Development of artificial surface layers for thin film cathode materials

Dissertation aproved by the
Department of Material and Geosciences
Technical University of Darmstadt

Requirements to obtain the academic degree of
"Doktor-Ingenieur" ("Dr.-Ing.")

MSc. Mercedes Alicia Carrillo Solano
from Barrancas, La Guajira, Colombia

Supervisor: Prof. Dr. Wolfram Jaegermann
Co-supervisor: Dr. Laurence Croquennec (Université de Bordeaux)

Date of submission: August 31, 2015
Date of examination: October 30, 2015

Darmstadt, 2016
D 17

Development of artificial surface layers for thin film cathode materials

Genehmigte Dissertation von Mercedes Alicia Carrillo Solano aus Barrancas, La Guajira, Colombia

1. Gutachten: Prof. Dr. Wolfram Jaegermann
2. Gutachten: Directrice de Recherche Dr. Laurence Croquennec

Tag der Einreichung: 31 Aug. 2015
Tag der Prüfung: 30 Okt. 2015

Darmstadt — D 17

Erklärung zur Abschlussarbeit gemäß § 22 Abs. 7 APB der TU Darmstadt

Hiermit versichere ich, die vorliegende Dissertation ohne Hilfe Dritter nur mit den angegebenen Quellen und Hilfsmitteln angefertigt zu haben. Alle Stellen, die Quellen entnommen wurden, sind als solche kenntlich gemacht. Diese Arbeit hat in gleicher oder ähnlicher Form noch keiner Prüfungsbehörde vorgelegen.

Datum:	Unterschrift
____________________	____________________

Thesis Statement pursuant to § 22 paragraph 7 of APB TU Darmstadt

I herewith formally declare that I have written the submitted thesis independently. I did not use any outside support except for the quoted literature and other sources mentioned in the paper. I clearly marked and separately listed all of the literature and all of the other sources which I employed when producing this academic work, either literally or in content. This thesis has not been handed in or published before in the same or similar form. In the submitted thesis the written copies and the electronic version are identical in content.

Date:	Signature
____________________	____________________

Con el amor más grande,
para Amador, María Mercedes, Carmen G. y José Luis A.

Miluji tento nový příběh s tebou Zee.

Acknowledgments

The presented work and PhD thesis was performed under the IDS FunMat framework, a joint collaboration between the *Surface Science group* at the *Technische Universität Darmstadt*, and the *Group 2. Energy: Materials and Batteries*, at the *Institut de Chimie de la Matière Condensée de Bordeaux (ICMCB-CNRS)*. I would like to express my immense gratitude de the IDS FunMat coordination, Prof. Jean Etourneau, Laurent Servant, Marianne Delmas and Audrey Sidobre.

To my advisor Prof. Wolfram Jaegermann, I would like to thank for his continuous support, patience, motivation, and immense knowledge provided to my work. His guidance helped throughout my research and writing of this thesis. To all the people at the Surface Science group at TU Darmstadt and the Material Science Department for their collaboration and support during the developments of this work.

To my advisors in ICMCB, Laurence Croguennec and Philippe Vinatier, I would also like to thank for their valuable collaboration and dedication to this project. To all my friends and colleagues at the ICMCB and Group 2, for all their help and guidance during my stays in Bordeaux.

A very special mention to Marc Dussauze for his guidance and support on the last stages of my PhD. A special thanks also to the *Groupe Spectroscopie Moléculaire at Institut des Sciences Moléculaires (ISM)* in Bordeaux, for allowing me perform experiments at their labs.

To my dearest friends from IDS FunMat, and all those beautiful souls I was able to meet during my stays both at Darmstadt and Bordeaux. I was lucky to have met all of you and I'm grateful to have had you close throughout this experience.

To Natascha and Deniz, all my love always.

A mi familia, quienes han sido mis pilares y debo tanto apoyo y respaldo en los momentos difíciles; por su cariño, amor y comprensión, siempre.

Contents

Symbols and Abbreviations

Symbol	**Description**
α	Angle between lattice planes
A	Area
C	Concentration
c_x	Atomic fraction
E	Potential
E_a	Activation energy
E_{kin}	Kinetic energy
f	Photon flux
F	Faraday constant
$G1$	Refinement parameter
I	Intensity
λ	Mean free path of the photoelectrons
M	Molar mass
n	Density of atoms
P	Pressure
Φ	Work function
Q	Capacity
Q_e	Specific capacity
R	Resistance
S	Sensitivity factor
σ	Ionic conductivity
σ_0	Specific ionic conductivity
T	Temperature
θ	Angle between the photon path and detected electrons
W	Warburg impedance element
y	Photoelectrons detection efficiency
z	Ion charge
Z'	Real part of impedance
Z''	Imaginary part of impedance

Abbreviation	**Description**
AC	Alternating current
ALD	Atomic layer deposition
CV	Cyclic voltammetry
CVD	Chemical vapor deposition
Daisy − Bat	Darmstadt integrated system for battery research
DC	Direct current
DEC	Diethyl carbonate
DMC	Dimethyl carbonate
DTGS	Deuterated triglycine sulfate
EC	Ethylene carbonate
EDX	Energy dispersive X-ray spectroscopy
EIS	Electrochemical impedance spectroscopy
GC	Galvanostatic cycling
ICMCB	Institut de Chimie de la Matière Condensée de Bordeaux
ICP	Inductively coupled plasma spectroscopy
IR	Infrared spectroscopy
LiBON	Lithium boron oxynitride
LiPON	Lithium phosphorus oxynitride
NMR	Nuclear magnetic resonance
Ob	Bridging oxygen
Onb	Non-bridging oxygen
PC	Propylene carbonate
PVD	Physical vapor deposition
rf	Radio frequency
TUD	Technische Universität Darmstadt
SEI	Solid electrolyte interface
SOC	State of charge
UHV	Ultra-high vacuum
UPS	Ultraviolet photoelectron spectroscopy
VB	Valence band
XAS	X-ray absorption spectroscopy
XPS	X-ray photoelectron spectroscopy

Chapter 1

Introduction

The societal challenges of further developing nations are closely related to controlled production, storage and use of energy. Even though the true mid- or long-term effects of excessive fossil fuel burning is not fully known, it is clear that eventually alternative ”clean” energy sources will be indispensable. Nevertheless the possible use of unconventional solutions rely on the availability of storage systems that meet the requirements for a fast paced energy-dependent world.

Among those, batteries used today satisfy the demands and requirements for small devices. Nevertheless the possibility to apply them in larger scales (energy storage, electro-mobility) can only be reached when energy densities increase 2 to 5 times their current value [1].

Battery systems are composed of a cathode and an anode in contact with an electrolyte. A conventional rechargeable lithium-ion battery is composed of a graphite anode as negative electrode, a non aqueous electrolyte typically related to $LiPF_6$ salt in organic solvent and a positive electrode based on intercalation materials [2,3]. The interfaces between these components have particular features and undergo complex electrochemical processes which occur during storage and battery operation [4].

The graphite anode and the electrolyte interface has attracted the most attention in research until now. Nevertheless in recent times the importance of the cathode-electrolyte interface has been acknowledged due to the fact that after lithium ion transfer on the positive electrode decomposition oxidation reactions may occur [5–8]. In general, capacity fading of positive active material can originate from three basic principles [9,10]:

- Structural changes during successive lithium extraction/insertion
- Chemical decomposition/dissolution reaction
- Surface modification

Studies on the decomposition mechanisms have been discussed for alkyl carbonates which promote surface reactions, like e.g. those based on electrolyte decomposition due to nucleophilic attack or reactions with the transition metal [5, 11–13].

The complexity of battery systems and cathode layers call for multidisciplinary efforts applying advanced techniques to elucidate surface reactivity and interface formation. Recently analytical methods have been used for this purpose, including X-ray photoelectron spectroscopy (XPS) [5, 7, 12, 14], infrared spectroscopy (IR) [8, 11] and X-ray absorption spectroscopy (XAS) [13].

The contribution of surface science made through the years has helped in the understanding of surface related elemental processes in electrochemistry and photo electrochemistry [15–18, 18]. An XPS study on electrochemically cycled $LiCoO_2$ thin films has shown the formation of phosphate, fluorophosphate and carbonate species with an electrolyte containing $LiPF_6$ in (EC/PC/DMC) solvent mixture [14].

More recently, an ultra-high vacuum (UHV)-based surface science oriented approach has been introduced, focused on the formation of, and charge transfer at, cathode-electrolyte interfaces of $LiCoO_2$ with liquid electrolyte components (DEC solvent and water) or a solid state electrolyte (LiPON) [19]. Additionally, the surface layer at the positive electrode was found to strongly increase cell impedance and effect the kinetics which has significant impact on the battery performance [20, 21].

Since it was first proposed, $LiCoO_2$ has managed to remain the standard cathode in commercial batteries due to its high stability, good rate capability and acceptable safety features. It is the most used cathode material in lithium-ion batteries powering most of the electronic devices used daily [22].

For the last two decades the research on positive electrodes has made great advances in terms of novel material preparation, structure and reaction control. Major improvements can still be achieved on materials used at present, for example recently, the energy density could be increased between 2 and 3 times, as mentioned by Thackeray [1].

1.1 Motivation

Current batteries are mainly composed of $LiCoO_2$ with carbon based anode and organic electrolytes with a $LiPF_6$ salt. Determining the composition of the cathode surface after electrolyte contact, specifically looking at the newly formed cathode-electrolyte interface, will give insight on different strategies that can be used to enhance properties and performance of commercial batteries. Analysis of the surface layer may also help to tailor new electrolyte systems by understanding their properties and effects on the active material.

One approach proposed to decrease reactions and enhance battery performance, by enabling high rate capability or by suppressing phase transitions, is the use of thin coatings of metal oxides and ion conducting materials, like ZrO_2, Al_2O_3, LiPON, LiF [3, 23–25]. Studies done on ZrO_2 coated $LiCoO_2$ or other cathodes have mainly focused on electrochemical cycling and structural properties, showing the benefits in reducing capacity loss and increases structural stability [26–30]. Nevertheless the decomposition of a coated cathode surface has not been fully addressed. LiPON on the other hand has been thoroughly studied given the additional application it has as solid state electrolyte for thin film batteries [31, 32]. For this reason the interface formation between LiPON and $LiCoO_2$ has drawn much more attention evidenced by the number of studies already done (see for example [24, 33, 34]). However, work on the evolution of coating layers on $LiCoO_2$ are again devoted to the electrochemical performance while the interface after cycling has not been addressed [35–37].

The study of the interface of a soaked model electrode in electrolyte solutions have also served as valuable information on how the cathode materials are reacting. Surprisingly few studies have focused on the surface characterization prior to the electrochemical study [38, 39] with samples exposed to air. At this point it is important to consider that interfaces are highly sensitive to ambient contaminations which can affect the analysis of the resulting surface. Another recent study done by Yamamoto et al. has shown an improved cyclic performance where the electronic structure of the electrode-electrolyte interface was analyzed with total-reflection florescence X-ray absorption spectroscopy (TRF-XAS) [40]. Their conclusions were focused on the stability of some cathodes after electrolyte immersion due to a lack of potential change in the space charge layer at the surface.

For the electrolyte composed of $LiPF_6$ in ethyl carbonate (EC) and diethylene carbonate (DEC) with a weight ratio of 1:1, little information is found in literature. Not withstanding, the reports that have been done with $LiPF_6$ in EC:DEC (1:1) electrolyte mixture focus on the surface chemistry for a non active material, which gives only a part of the view since the possible reactions with the active materials are not tackled [7, 14, 38, 39, 41]. In this way, a good approach is to look into the initial effects of the electrolyte when set in contact with $LiCoO_2$, which adequately serves as model electrode [38].

In the case of the solid electrolyte it is important to understand the bulk properties as well, since it will all contribute to the ion conduction mechanism necessary for the battery to function. For the specific case of LiPON acting as solid state electrolyte many efforts have been focused on the final properties and the enhancement of the ionic conductivity. This includes thorough studies on nitrogen incorporation [42–45]. Until now, research has focused on the definition of the key points affecting the ionic conductivity but not on the phenomena occurring in the structure that delivers this enhancement.

1.2 Objectives and organization of the dissertation

As yet no systematic studies focusing on the decomposition of coated electrodes exist, a surface science study based on X-ray photoelectron spectroscopy is proposed.

The main objective of this thesis was to study the electrode-electrolyte interface of bare and coated model electrodes after electrolyte contact and/or electrochemistry. For this, two types of coatings were used to create artificial surface layers on the active material with ion conducting solid or a metal oxide: LiPON and ZrO_2, respectively. A secondary objective was to obtain key information concerning the well known ion conducting solid structure and to further analyze the implications of nitrogen incorporation on the ion conducting ability. This study is aimed to understand the mechanism behind the ionic conductivity when nitrogen is incorporated to the glassy structure or when the films are annealed. Both parameters are studied in terms of short and medium range order in the final network conforming the electrolyte with infrared spectroscopy (IR).

The first chapters (2,3) are dedicated to a literature review and an overview of the experimental techniques used for sample preparation and characterization.

Continuing, Chapter 4 is dedicated to the deposition and characterization of model and alternative cathode thin films composed of $LiCoO_2$ and $Li(Ni_xMn_yCo_{1-x-y})O_2$. A thorough description of the deposition methods employed and final properties of the thin films are shown and discussed.

Chapter 5 presents a detailed study of the degradation observed at the surface of $LiCoO_2$, employed as a model electrode, after electrochemical cycling, focusing on the reactions occurring with the electrolyte solution. A complete study on the surface layer formed when the model electrode was set in contact with the electrolyte and after electrochemical cycling was performed.

Chapter 6 describes the effects of the artificial surface layer grown on thin $LiCoO_2$ layers and its effect on the electrochemical properties of the material. A surface science approach was used to determine the composition of the interface between the artificial surface layer and the electrolyte before and after battery cycling for both sets of coating, LiPON and ZrO_2.

Moving away from the technical aspects of the battery performance and going towards a more fundamental understanding of the properties which LiPON has as ion conductor, Chapter 7 focuses on an IR study on LiPON coating, given the great interest and additional application as solid state electrolyte. Results are analyzed in terms of chemical stability, conductivity and composition.

The presented work concludes with a summary of the results obtained.

This thesis serves to provide valuable information on both technical and fundamental aspects of tailored artificial surface layers for positive electrode materials which are well known but which still have room for improvements after further efforts are done to understand the complex process occurring at the interface. This is aimed to obtain information for more efficient and stable systems that could be applied in advanced and large scaled technologies.

Chapter 2

State of the Art

2.1 Electrochemical systems

Electrochemical cells are devices which reversibly convert chemical to electrical energy from their active materials through redox reactions. Galvanic cells have electrochemical redox reactions with both reduction and oxidation processes. Electrochemical cells are mainly composed of two electrodes, the electrolyte, and a separator.

During the battery discharge, where spontaneous chemical reactions occur, oxidation processes take place at the negative electrode (i.e. the electrode at lower potentials; serving as anode), and the reduction processes occur at the positive electrode (cathode). Contrarily, when the battery is charging the reverse chemical reactions occur having a reduction reaction at the negative electrode (now as the cathode) and an oxidation reaction taking place at the positive electrode (now the anode). The terms negative and positive electrodes are preferentially used which consider the direction of the current. The positive electrode releases electrons to circulate on the external circuit while the negative electrode receives electrons while the reduction reaction occurs. The electrolyte is an ion conductor which allows the movement of ions between the electrodes [46–48].

Batteries can be classified in several ways. The first is related to the size and function. They can be in micro-, miniature-, portable or automotive/ SLI (starting, lighting and ignition) configuration and uninterrupted power source (UPS). Micro-batteries are based on the thin film component technology, while miniature batteries work with liquid or solid based electrolytes and are used for microelectronic or miniature devices. These two have an average capacity of 200 µAh and 200 mAh respectively while portable and SLI have higher capacities (2 Ah and 50 Ah) [49].

Another classification relates to primary and secondary (rechargeable) character they poses. The difference recalls on the type of electrochemical system which determines if the reaction is reversible or not. Primary batteries are able to provide energy immediately in one discharge, while secondary batteries can be repeatedly recharged and charged again through an external power supply. An ideal reversible system will have unaffected structure and volume change of the active material with cycles.

Among the most important rechargeable batteries are the lead acid (Pb-acid), nickel-cadmium (Ni-Cd), nickel metal hydride (Ni-MH) and more recently sodium (Na), lithium (Li) and lithium ion (Li-ion) batteries [1]. Ever since the discovery of the first electrochemical cell by Alessandro Volta in 1800, further development of aqueous electrolyte based Ni-Cd and Ni-Fe systems were done for possible automotive applications. Secondary batteries therefore became a matter of interest in research and development laboratories. Over the years, the implementation of these batteries was unsuccessful and new alternatives were introduced. Focus has shifted from Ni-MH, Pb-acid and Ni-based to sodium and lithium technologies due to environmental drawback of toxic materials plus the poor capacities and low specific energy delivered [1]. Even though Ni-MH batteries may show higher power densities when compared to Li-ion (especially at low temperature), lithium-ion technology offers the best prospect for high energy and high power batteries, as indicated on Figure 2.1.

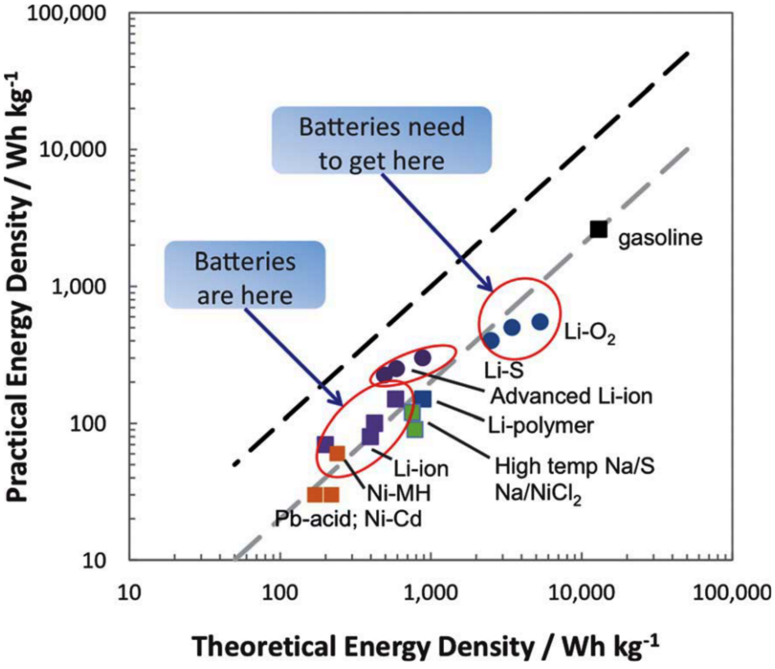

Figure 2.1: Theoretical specific energy of several rechargeable systems plotted against their pratical energy density. Taken from [1].

2.2 Lithium batteries

Lithium was considered for its light weight, non toxicity, low reduction potential (-3.045 V in aqueous solution at 25°C) and specific capacity of 3860 $mAhg^{-1}$. A first approach was made by employing a host oxide which could be capable of having lithium inserted, as cathode, and metallic lithium as anode. First intercalation materials used were layered dichalcogenide as TiS_2. These batteries presented a high voltage but at the same time had two main problems. One related to the dendrite growth at the negative electrode due to deposits of lithium which would break through the separator and arrive to the positive electrode with final short circuits. This dendrite growth can further provoke a raise in cell temperature and pressure and poses a risk of electrolyte-solvent ignition. The second drawback is related to the parallel reactions with the organic solvents present in the electrolyte, originating a loss in battery capacity [1, 50].

The biggest development done on lithium ion batteries was in 1991 with the introduction of a high voltage and high energy system where metallic lithium was replaced by carbonaceous compounds as negative electrode and a transition metal oxide, $LiCoO_2$ as positive electrode [1, 51].

Figure 2.2 presents a scheme of a lithium ion battery using these components. During the discharge process the lithium ions move from the positive electrode and are transported through the electrolyte to the negative electrode. Transition metal ions are reduced by the electrons coming from the electrical circuit during the lithium ion insertion. During discharge the reverse process is occurring giving electrons to the electrical circuit [2, 52].

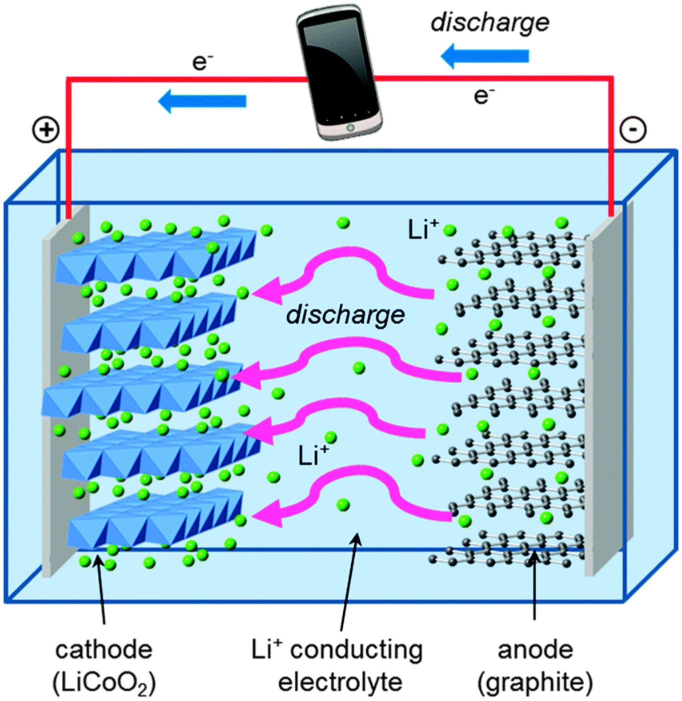

Figure 2.2: Schematic representation of a rechargeable lithium-ion battery. During charge the lithium ions move from the positive to the negative electrode through the liquid electrolyte and electrons are introduced from the external circuit. During discharge the process is reversed and electrons move in the reverse direction. Taken from [2].

The redox reactions taking place are the following:

$$\begin{array}{llcl} \text{Cathode:} & \mathrm{LiCoO_2} & \rightleftharpoons & \mathrm{Li_{1\text{-}x}CoO_2} + \mathrm{xLi^+} + \mathrm{xe^-} \\ \text{Anode:} & \mathrm{C_6} + \mathrm{xLi^+} + \mathrm{xe^-} & \rightleftharpoons & \mathrm{Li_xC_6} \\ \hline \text{Global Reaction} & \mathrm{LiCoO_2} + \mathrm{C_6} & \rightleftharpoons & \mathrm{Li_{1\text{-}x}CoO_2} + \mathrm{Li_xC_6} \end{array} \tag{2.1}$$

The advances observed in the electronic industry are increasing the demand of more sophisticated and efficient batteries that should be stable during extended charge-discharge cycles, have an elevated energy density, low weight and reduced volume, as well as low cost and low environmental impact [52].

Batteries have mainly the feature of generating energy without having a significant potential decrease. There are certain magnitudes that describe this feature. Capacity Q is the amount of charges that can be stored by a material and is expressed by Q=zF/M where z the ion charge (z_{Li}=1), and F the Faraday constant (96485 $\mathrm{Cmol^{-1}}$) and M is the molar mass. The capacity will depend on the amount and type of material, and is expressed in Ah. When related to the total mass or volume of the material, the specific capacity Q_e is expressed as $\mathrm{Ahkg^{-1}}$and $\mathrm{Ahl^{-1}}$respectively. The specific capacity that a battery can deliver will depend on the chemistry of the system. The stored energy can be maximized by having a large chemical potential difference (V) between the two electrodes or by minimizing the mass or volume of the reactants per exchanged electrons being small as possible [50]. Lithium ion batteries have in average a specific energy between 100 Whkg^{-1}and 150 Whkg^{-1} [53].

Considering the intrinsic properties of the materials used, the main advantages lithium ion batteries present, may be summarized as follows.

1. High energy density. The mass is around half and the volume is between 20-50% when compared to a Ni-Cd or Ni-MH of the same characteristics.
2. A high cell voltage, three times higher than those of Ni-Cd and Ni-MH, which is a good feature for implementation in miniature batteries.
3. Excellent cycling efficiency of 99.95% compared to the 70-80% of alkaline and acid batteries.
4. Absence of memory effect by partial charge or discharge process.
5. Does not contain highly contaminating heavy metals like Cd, Pb and/or Hg.

As mentioned before, the cell consists of several components: anode, electrolyte and positive electrode. The anode is the negative electrode where the oxidation reaction takes place and electrons are injected to the external circuit. The anode should be an efficient reducing agent and have high coulombic output (Ah/g), good conductivity and stability. Lithium metal was for some time considered as anode due to its high electronegativity and low weight. Nevertheless serious safety and cycle life problems were found due to dentridic growth of lithium metal deposits upon charge. Therefor, several options have been considered including silicon insertion and carbonaceous materials [54–56].

2.3 Positive electrodes in lithium ion batteries

Advantages and disadvantages of lithium-ion batteries are greatly related to the positive electrode employed. There is a variety of materials studied to be used as cathodes in lithium ion batteries. These include layered transition metal oxides, spinel mixed oxides, olivines, perovskites and most recently some organic polymers [57–60]. For layered oxides the lithium insertion is favored in open framework or layered type materials where the lithium is bound in the interstitial sites. Figure 2.3 shows a scheme of the crystal structure of lithium transition metal oxides with the general formula $LiMO_2$ where M is the transition metal (Co, Ni, Mn, Fe, etc.) which adopt the α-$NaFeO_2$ structure with R-3m symmetry. This structure can also be described as MO_6 octahedron $(MO_2{}^{-})_n$ layers sharing edges with metallic ions forming sheets in between [51].

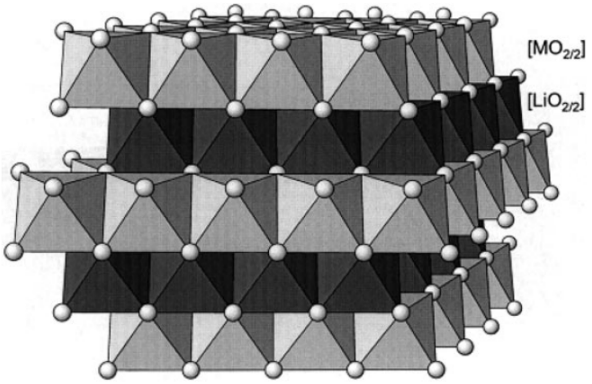

Figure 2.3: Crystal structure of $LiMO_2$ with α-$NaFeO_2$ type. Taken from [51].

Lithium cobalt oxide ($LiCoO_2$) was first proposed in 1980 and is at present the most used positive electrode material in commercial batteries [61]. $LiCoO_2$ has a high lithium diffusion and a good specific capacity of 140 mAh.g^{-1}. Additionally it presents high volumetric and gravimetric specific capacity [62, 63]. It can be found in two crystal forms. One is the spinel-like (disordered) low temperature (LT) phase and the other is the layered hexagonal structure, high temperature phase (HT). This abbreviated names were based on the solid state reaction temperature used in each case. Nevertheless, some more recent studies have shown a wet chemistry approach were the high temperature phase is also obtained [64]. The layered HT-$LiCoO_2$ can be prepared by different methods, physical vapor deposition (PVD) and chemical vapor deposition (CVD) [32, 62, 64–68], pulsed laser deposition (PLD) [69, 70] and sol-gel [71].

The performance of the material with this layered structure is affected by strong orientation effects since lithium movement will only occur in two dimensions. Therefore, the ion displacement will be unfavored when layers have a strong preferred orientation of the c-axis parallel to the substrate. The best rate capabilities appear when the HT-$LiCoO_2$ phase material is polycrystalline, or when it presents a favorable orientation in relation to the electrolyte [64].

The main limitations that $LiCoO_2$ has are due to low reversible capacity and performance degradation [32, 64, 72]. Lithium ions are removed and inserted at potentials close to 3.9 V and 4.2 V, respectively. Lattice distortion from hexagonal to monoclinic will occur when the Li ions in the CoO_2 framework goes through order/disorder transitions [73]. Even though all the lithium present can be electrochemically removed from the layered structure, when charged over 4.2 V, corresponding to half of the total amount of ion, poor cyclability is expected due to phase transitions in the material and spontaneous release of oxygen [73–75]. Over de-lithiation will also produce highly reactive Co^{4+} ion that may react violently with the electrolyte [51, 76].

Lithium nickel oxide $LiNiO_2$ is isostructural with $LiCoO_2$ and was considered as possible replacement due to its higher specific charge, higher stability, and the lower costs of production. Studies developed on the implementation of $LiNiO_2$ has delivered several drawbacks related to disordered structure and loss of lithium during preparation [51, 77]. Efforts were focused on replacing some nickel with Co or Al with the aim to reduce the disordered structure. Nevertheless the resulting materials present low energy density given the low operating voltage [78, 79].

Lithium manganese oxide $LiMn_2O_4$ serves as well as a promising material similar to $LiCoO_2$. It presents a stable cubic structure with a crystal lattice remaining unchanged and minor volumetric changes occurring when cycled between 3.5-4.5 V on the main electrochemical region. In this range the extracted lithium is between 0 and 1. However, at the second de-lithiation region, with lithium extracted between 1-2 (around 3 V), a Jahn-Teller distortion occurs favoring a structural change from cubic to tetragonal [64]. Together with the high mobility of the Mn^{2+} ions in this spinel structure thus will reduce significantly the cycle life. In this way several studies have dedicated efforts to stabilize the structure and enhance capacity and operating voltage [61, 80].

The substitution of Co by both Ni and Mn was found to deliver high reversible capacity, good thermal stability, excellent rate capability as well as reduced toxicity compared to commercial $LiCoO_2$ [81]. Incorporation of other transition metals is an alternative approach that can serve to overcome these limitations. A well studied material composition is $Li(Ni_xMn_yCo_{1-x-y})O_2$ ($Li(NiMnCo)O_2$) [58, 69, 82, 83]. In this structure the transition metals present different characteristics. Nickel 2+ and 3+ are found with Cobalt in 3+ and Manganese in 4+ oxidation states. This last cation was found to mainly stabilize the structure while Ni and Co enforce the electrochemical activity and rate capability respectively [58]. It presents high cyclability attributed to the low unit cell volume change [84].

2.3.1 Deposition of thin film cathode materials

Batteries in small dimensions are also of interest as the size of portable microelectronic devices decrease continuously, and thin films would be a good approach towards smaller battery units. Several techniques have been used for the deposition of thin film cathode materials on planar substrates, including vapor based techniques, physical vapor deposition (PVD) and chemical vapor deposition (CVD) [32, 62, 64–68]. Other methods have also been used, like pulsed laser deposition (PLD) [69, 70] and sol-gel [71].

Vapor based techniques serve for efficient production of high quality thin films. Physical and chemical methods deliver films with particular characteristics. PVD is a vacuum based technique which is extensively used for deposition of thin film materials also applied in industry [72]. It presents high deposition rate, long term stability, and a cost efficient method.

Planar structures lack to have a high power delivery and high energy density. Increasing the internal surface between battery components (cathode, electrolyte and anode) will provide a higher total battery current with similar internal current densities compared to a planar configuration [64, 72].

From all chemical deposition processes, CVD is an established technique which produces materials with structural control at atomic and nanometer scale as well as conformal coverage of 3D substrates. Nevertheless, the main limitations in CVD processes are the reduced availability of proper volatile precursors and the complexity to deposit multicomponent systems [85]. The precursors employed are usually expensive and tend to be sensitive to air and/or moisture. Additionally they present a complex vapor pressure behavior as function of the temperature and pressure. For a multicomponent system the composition control is difficult since the different evaporation rates of the precursors have a non linear behavior with temperature and pressure.

Additionally, the mechanism used to transfer the precursor solution to vapor phase becomes particularly important in order to obtain less impurities and defects on the final grown material. For this reason several delivery methods based on liquid injection have been developed recently [86].

One of the chemical deposition process that has been studied extensively for the preparation of nanoparticles and thin films is spray pyrolysis [87–92]. In this process the precursors, which are soluble in water or alcohol based solutions, are sprayed as fine droplets into an evaporation chamber. This could be described as a micro delivery system that preserves the initial concentration from the solution. Once the solvent is removed, the dried droplets react in a pyrolysis reaction. Depending on the temperature applied one can obtain either powders crystallizing in one phase, hollow spheres (at low temperatures), or compact thin films (at high temperatures). This method is simple, inexpensive and operates continuously with high product yield. Even though the particle morphology control remains as one of the main problems for the deposition of new materials [85, 93], related spray pyrolysis techniques have demonstrated the possibility to achieve desired thin films of positive electrodes and solid electrolyte thin films for lithium-ion battery applications [94, 95].

2.4 Electrolyte

The electrolyte is the means of ion transport and serves as connection between cathode and anode. In general, electrolytes should have good thermal stability, high ionic conductivity and low electronic conductivity. Moreover, they should be stable in the electrochemical window used depending on the type of battery and active materials present. Due to the wide range of batteries existing, electrolytes can be found in different forms; as liquids with aqueous or organic based solvent; like ionic liquids, solvent-free, and/or gelled polymer-based, or as solid-state [54, 64, 96, 97]. Table 2.1 presents the typical ranges of specific conductivities of electrolyte systems used in batteries [54].

Table 2.1: Conductivity ranges of several electrolytes at ambient temperature [54].

Electrolyte system	Specific conductivity, S cm^{-1}
Aqueous electrolytes	$1\text{-}5{\cdot}10^{-1}$
Molten salts	$\sim 10^{-1}$
Inorganic electrolytes	$2{\cdot}10^{-2}\text{-}10^{-1}$
Organic electrolytes	$10^{-3}\text{-}10^{-2}$
Polymer electrolytes	$10^{-7}\text{-}10^{-3}$
Inorganic solid electrolytes	$10^{-8}\text{-}10^{-5}$

2.4.1 Liquid electrolytes

Liquid electrolytes are solvent based solutions with a dissolved ion conducting salt. Given that lithium intercalation takes place at very negative potentials, water based solutions are not adequate. For this reason the most common solvent mixtures are those with organic solvents including alkyl-carbonates, esters and ethers. Figure 2.4 presents the structure of most commonly used solvents. This section concentrates mainly the electrolyte components relevant for this thesis. Detailed reviews on these and other electrolytes can be found for example in references [4, 97, 98].

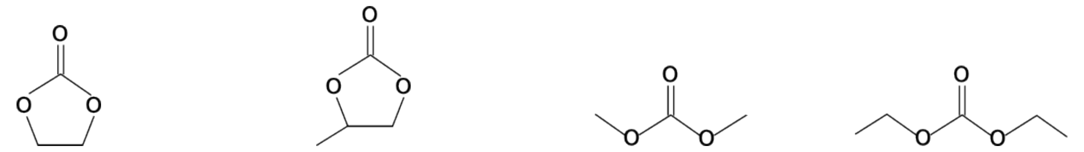

Ethylene carbonate Propylene carbonate Dimethyl carbonate Diethyl carbonate

Figure 2.4: Organic solvents most commonly used in lithium ion battery electrolyte mixtures [97].

The solvents in non aqueous electrolytes should allow a large concentration of efficiently dissolved salt. Elevated molar conductivity and dielectric constant are also important features. Voluminous salt anions will favor the negative charge distribution preventing ionic coupling which results in a better ionic conductivity and salt solubility. This way the Li ions in solution can be full surrounded by solvent molecules, reducing the influence of the anion. Low viscosity is also important since the ionic movement will be enhanced.

Some salts that have been considered are $LiPF_6$, $LiClO_4$, $LiAsF_6$, $LiBF_4$ [97, 99, 100] and LiTFSI [101]. Table 2.2 presents the properties of some of these salts. $LiPF_6$ is the most used salt given the low toxicity (compared to poisonous $LiAsF_6$) and the thermal stability (compared to explosive $LiClO_4$), as well as stability with anode materials.

Table 2.2: Lithium salts present in the electrolytes for lithiuim ion batteries [97].

Salt	Molar mass	Ionic conductivity mS cm^{-1} (1 M, 25°C) in EC/DMC	Structure
$LiBF_4$	93.9	4.9	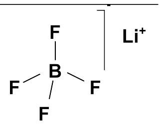
$LiPF_6$	151.9	10.7	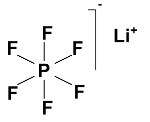
$LiAsF_6$	195.9	11.1	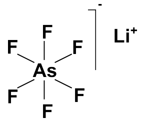
$LiClO_4$	106.4	8.4	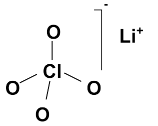

A major concern about the application of $LiPF_6$ is the high reactivity with water traces and further formation of corrosive HF. Moreover, at higher voltages it may suffer from decomposition towards LiF and PF_5 which can further hydrolyze and form HF and PF_3O. These two products are highly reactive towards both anode and cathode materials, thus a large amount of these contaminations may easily affect battery performance.

2.4.2 Solid electrolytes

The possibility that Li ion batteries can deliver high energy density arise from the high cell voltages obtained. As seen before, the use of aqueous electrolytes is not possible in this voltage range and organic based electrolytes have serious safety concerns. Solid state batteries were thought to overcome these and other problems related to possible leakage, side reactions, gas formation, phase transitions at low temperature (improving low-temperature performance) and difficulty to achieve smaller dimensions. A more recent view has focused on the application of batteries to power vehicles and as renewable energy storage systems. These potentially large scaled batteries would need great amount of electrolyte solution making safety considerations even more important. Solid state electrolyte implementation is therefore expected to reduce risks of current commercialized polymer/gel batteries while giving reliability, storage stability and very long cycle life [102].

As the electrolyte is the medium used to transport the lithium ions during battery operation, ionic conductivity is one of the most important properties that should be considered for electrolyte engineering. The discovery of fast ion conducting solids triggered the development of solid state batteries. Materials with high ionic conductivity must have a low energy barrier to overcome during transport and should contain vacancies in which the ions can move to, i.e the activation energy (Ea) should be small. For the specific application as battery electrolyte these materials should also have a low electronic conductivity. Additionally they should be chemically stable, not hygroscopic, easy to prepare and low cost. Solid electrolytes which are developed at present have ionic conductivities between 10^{-1}(for Ag^+ solid electrolytes [102]) and 10^{-5} $S.cm^{-1}$which come close to values observed for liquid electrolytes [54, 97, 103].

A wide variety of solids with high ionic conductivity are known at present. These can be found as mono- or polycrystalline, ceramic, amorphous and polymeric mixtures. Solid electrolytes have a structure which is rigid with a subnetwork of mobile ions. Compared to liquid electrolytes they have an overall advantage related to the exclusive ion migration, while in liquid electrolytes different species can also migrate and participate in side reaction, including ions and impurities [102]. Lithium ion conductors may be classified in four groups [104, 105]

1. Perovskite type oxides: e.g. $(Li,La)TiO_3$
2. NASICON-structured lithium electrolytes: e.g. $LiM_2^{IV}(PO_4)_3$(M^{IV} = Ti, Zr, Ge)
3. Garnet-type structures containing transition metal oxides: e.g. $Li_5La_3M_2O_{12}$ (M = transition metal);
4. Glassy and glass–ceramic electrolytes: lithium nitrides, sulfides (also found as crystalline materials [106]), borates and phosphates.

A recent summary of the progress of solid electrolytes has been made and can be seen on Figure 2.5. These materials generally present a lithium transport number near to the unity, therefore materials with an ionic conductivity in the order of 10^{-3} S cm^{-1}will suffice to obtain power densities comparable to those of commercial batteries which contain liquid electrolytes. At present it is possible to find oxides and sulfides that achieve these values of conductivity. The implementation in all solid state batteries of these materials are nevertheless somewhat complicated due to limiting factors like low decomposition voltage (Li_3N, hygroscopic character (Li-β-alumina), high reactivity with Li metal ($Li_{1.3}Ti_{1.7}Al_{0.3}(PO_4)_3$, and unfavorable preparation conditions ($(Li,La)TiO_3$(Perovskite-type)). On the other hand, Li_9AlSiO_8 and $Li_{2.88}PO_{3.86}N_{0.014}$ (LiPON) have moderate conductivity but are stable against lithium. The main challenges the development of all solid state batteries and implementation of solid electrolytes are related to the relatively low power density, high ionic resistance at room temperature and high manufacturing costs. The problem of having low ionic conductivities in the solid electrolytes can be addressed by reducing the ohmic losses by applying very thin films. LiPON is therefore employed as electrolyte for thin film technology found today [31, 103–105, 107].

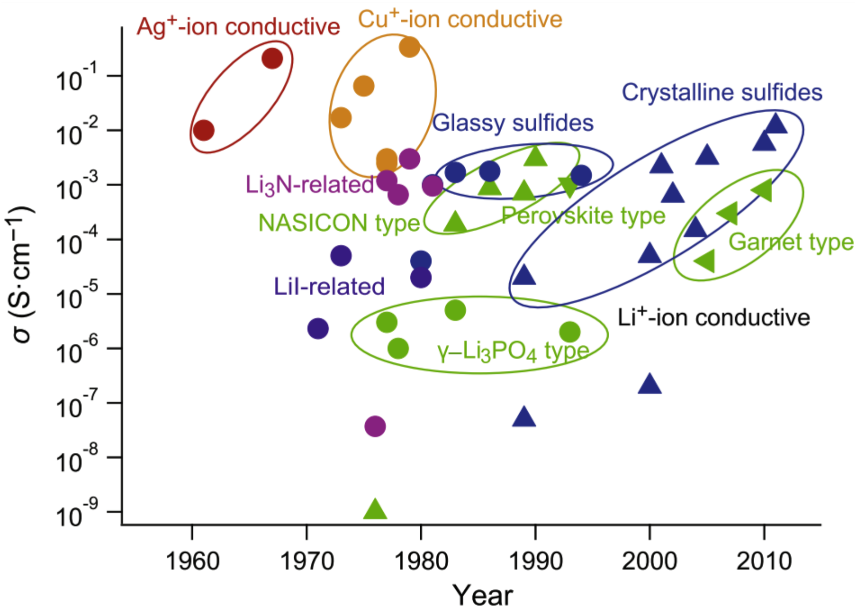

Figure 2.5: Progress in solid electrolyte for the past 50 years. Taken from [102].

2.4.3 LiPON: Lithium phosphate oxynitride

A large number of the electrolytes used in microbatteries are glass ion conductors. Some examples of bulk ion conducting oxide glasses include silicates, borates and phosphates.

Phosphate glasses are formed by PO_4 tetrahedrons linked through bridging oxygen ions forming chain or network structures. Modifying units are introduced to enhance material properties for determined applications [108]. Phosphate glasses modified with different metal oxides have been long studied due to their particular properties. Just to mention some examples, zinc phosphate has high chemical durability, iron phosphate is used as nuclear waste host, alkali aluminophosphate compositions have low glass transition temperatures and high expansion coefficient, while bio-compatible phosphate glasses and glass ceramics are used in medical applications [109–113]. Focus has been set for alkali elements like Li or Na for their low melting temperature and high thermal expansion coefficient as well as the fast ion conductivity that make them good candidates for solid state electrolytes [114–116].

Li_3PO_4 orthophosphate glass is an insulator with a large band gap (5.75 eV) [117]. On one side PO_4 tetrahedrons are joined with covalent bonding and on the other lithium and oxygen atoms are linked with ionic bonds, which is a structural arrangement responsible for improving the chemical durability towards water.

The ionic conductivity of a glass is closely linked to the mobility of charge carriers. These materials present conductivities between 10^{-3} and 10^{-6} S cm^{-1}, less than the observed for liquid electrolytes. The best ionic conductivities found for bulk glasses are from thin film sulfides. However, sulfide materials are highly hygroscopic and thus difficult to implement on an industrial scale. This is not the case for oxide glasses. However, given the low ionic conductivity that oxide glasses present, several methods have been proposed to improve ion mobility. Studies on Li-borate glasses reported an increase of ionic conductivity by structural modification of the interface with thickness control of materials [118–120]. A second approach was related with doping of borate glasses with salts. A third method was the incorporation of nitrogen into the glassy structure which is known to additionally improve mechanical and chemical properties. Loehman concluded that the addition of nitrogen to an oxide glass enhances chemical durability, and increases its glass transition temperature (Tg), hardness, fracture toughness and elastic modulus [121]. The incorporation of nitrogen to the different oxides will result in oxynitride type glasses like SiAlON [122], NaPON [123], LiNaPON [124], LiBON [125, 126] and LiPON [31, 127].

LiPON is the most used material as a solid electrolyte in microbatteries since it was first deposited by Bates et al. as thin film in 1992 [31, 127]. The deposition of the thin film was done by reactive sputtering starting from a crystalline Li_3PO_4 target and nitrogen - argon gas mixture to produce the plasma [127]. The potential stability window of LiPON calculated by the Bates and his group was 5,8 V which indicates the materials' stability when in contact with lithium [128]. For the case of RF magnetron sputtering, which is a common method used for the deposition of LiPON thin films for electrochemical applications, many authors have found the influence of RF power [45, 129–132], N_2 gas flow [42, 131], N_2 pressure [45, 130, 133] and substrate-target distance [45, 134], on the final composition, Li ion conductivity, film morphology and deposition rate. The values of composition significantly depend on the deposition parameters.

Introducing nitrogen into the glassy network in substitution of the oxygen will give nitrogen two types of configuration, which is double and triple coordination with phosphorus. These species which create the three dimensional glass network have been detected and studied with different techniques (NMR, XPS). Bunker et al. established a theory for nitrogen incorporation in the phosphate structure where 2 units of Nt are formed on the extent of 3 bridging oxygen (Ob) while 2 units of Nd are made when only 1 bridging oxygen bond is broken [135].

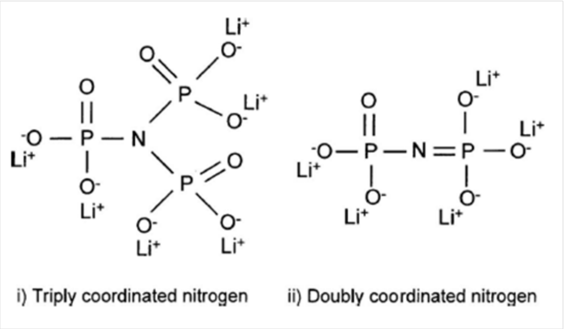

Figure 2.6: Possible structures which can be found for Nd and Nt coordinated nitrogen in LiPON [130,132].

Dussauze et al. found for LiBON how the main advantage of nitrogen incorporation is the improved chemical and mechanical stability with additional increase in cross linking in the network, which in the same way reduces the electrostatic energy since P-N bonds are more covalent than P-O bonds [136].

Understanding the nitrogenation mechanism is important and in this way studies have been dedicated to bulky glasses. Nevertheless, attempts to understand thin film material has been done less.

Until now several studies on composition and structure on bulky metaphosphate glasses [109,125,137] have been done but not so many have focused on thin film materials [138]. It has been found that these alkali metaphosphate glasses present particular properties different from bulk materials.

These are advanced techniques that enable the preparation of glassy structures with a larger glass region than bulk glasses prepared with traditional melt quenching processes. Understanding the effect the preparation conditions have on the thin films in terms of chemical composition and properties has captured the attention of many research groups.

Nevertheless, when these parameters are tuned to obtain the best ionic conductivity the films can be applied in electrochemical systems like as solid electrolyte for micro batteries or in our case as protective layer for the positive electrode.

2.5 Formation of surface layers on positive electrodes

The Solid Electrolyte Interface (SEI) layer is a known layer formed at the anode surface due to reduced species of the electrolyte [139], where the overall properties affect the battery performance. This layer is meant to prevent further decomposition of the electrolyte during battery operation. The main characteristics the SEI should have are:

1. Good adherence to the electrode material.
2. Insolubility in the electrolyte (including high temperatures).
3. Good electronic insulation
4. Good lithium ion conduction
5. Avoid solvent co-interaction by removing solvation shell from lithium ions.

Modification of the electrode surface may help in the improvement of cyclability of lithium ion batteries.

The SEI layer is composed of degradation products from electrolytes, for example, an organic/inorganic nature with salt degradation species, lithium carbonates and alkyl carbonates. XPS studies done by Dedryvère [8] on different cathode materials like $LiMnO_4$ and $LiNiO_2$ showed the presence of Li_xPF_4, $Li_xPO_yF_z$. Aurbach et al. studied $LiMO_2$ and observed Li_2CO_3 with $ROCO_2Li$ and polycarbonate species. They have attributed the formation of this layer to the nucleophilic reaction of $LiMO_x$ with the alkyl carbonates in the electrolyte, known to be strong electrophiles [140].

This surface layer is not necessarily detrimental since the organic surface films should protect the cathode from reactions with acidic species in the solution (which can promote transition metal dissolution [141]). This dissolution has also been seen by Markovsky et al. [142], when they studied the surface of the lithium anode after cycling, and showed presence of cobalt.

Some other problems arise from the reactions that can occur at the electrode/electrolyte interface. Vetter et al. [9] has detailed these reactions, where the most relevant are:

- Self discharge due to spontaneous lithium insertion and electrolyte oxidation.
- Nucleophilic reactions between the cathode and the solvent like for example in the case of lithium transition metal oxides containing Ni or Co.
- Structural changes and dissolution of the transition metal observed as a poisoning of the cathode and loss of oxygen.
- At highly de-lithiated states $x>0.5$ there is a strong oxidation of the electrolyte and oxygen loss which gives a high charge transfer resistance.

Similar to the negative carbon material, the degradation of positive active materials depends on state of charge and cycling conditions [9]. The insertion/extraction of lithium ions leads to changes in the molar volume of the materials, which may induce mechanical stress and strain to the oxide particles and, hence, to the electrode. Also, phase transitions can occur, which lead to distortion of the crystal lattice and further mechanical stress.

2.6 Surface modification of cathode materials

Several methods, which are used to improve the battery performance, include bulk dopant of cathode material, additives in the electrolyte solution and surface coating.

Many of the coating procedures are based on sol-gel technique where large amounts of solvents and a post-annealing treatments are needed [143–146]. In the last years several groups have reported on the electrochemical improvement of lithium ion batteries with surface modification of cathode materials by deposition of thin oxide layers applying ALD and PVD. Research has focused on Al_2O_3, TiO_2, B_2O_3, SiO_2 and ZrO_2 [26, 29, 143–148]. Other surface coating approaches with lithium conductors, like LiPON, have also been studied [24]. The thin film approach has the advantage that the surfaces obtained have a simpler geometry compared to particle systems [147]. In this way coating the material with a controlled and homogeneous film with known thickness also represents a positive point.

Promising results in terms of long term stability were found for ZrO_2 layer coating on $LiCoO_2$ cathode after 70 cycles, which showed only 7% of capacity decreases, while the uncoated cathode had 42% loss [26]. The overall effect the protecting layer has on the electrode was attributed to the stabilization of the crystal structure of the cathode during the first charge process. Additionally, it has been considered that the oxide layer served to decrease the deterioration of the cathode due to the physical barrier between active material and electrolyte avoiding possible metal dissolution [26].

Thackeray et al. proposed that the effect of the metal oxide is the creation of a solid electrolyte interface with lithium which protects the film against the attack of HF present in the electrolyte after decomposition [27]. Takamastsu and coworkers have found that very small layers of ZrO_2 are enough to improve the cyclability and potential durability by acting also as a layer decreasing the area of contact between cathode and electrolyte. They have also observed how thicker layers increase the resistance and and performance decreases [28].

Cho et al. have shown a range of materials as protective layers for $LiCoO_2$, and ZrO_2 proved to be the one with best results [143]. They speculate that Zr atoms occupy Co sites and which helps suppress the lattice constant changes. Other authors disagree, like Chen and Dahn [149] based on XRD studies. They found no lattice parameter variation with cycling while the capacity retention was independent of the fracture toughness mentioned by Cho et al. Instead, Chen and Dahn found that the coating causes a slight rate capability degradation.

In the same way, synchrotron-based in situ X-ray diffraction techniques used by Chung et al. on ZrO_2-coated $LiCoO_2$, showed how coated electrodes have less deterioration with cycling at higher voltages (4.8 V). Chung et al. argued how the improved characteristics of the coated material compared to the uncoated $LiCoO_2$ is due to reduced polarization effect generated by the precipitation of the electrolyte decomposition products on the electrode surface. The concluded that such coating provides some protection for the cathode surface of $LiCoO_2$ and reduces electrolyte decomposition.

Chapter 3

Methods

This chapter focuses on the two technical aspects involved in the development of the thesis. A first section will be dedicated to the techniques employed for the synthesis of the thin films, i.e. physical and chemical deposition routes. The preparation of the $LiCoO_2$, ZrO_2 and LiPON thin films were done by magnetron sputtering, while $Li(NiMnCo)O_2$ films were prepared by aerosol assisted chemical vapor deposition.

The second section is dedicated to the characterization of these materials performed with the help of several methods, including X-ray photoelectron spectroscopy, scanning electron microscopy, energy dispersive X-ray spectroscopy, X-ray diffraction, inductively coupled plasma spectroscopy and infrared spectroscopy. Additionally, the electrochemical performance of the above mentioned materials was studied using a battery ensemble. For this, cyclic voltammetry, galvanostatic cycling and electrochemical impedance spectroscopy were measured.

This PhD thesis was a collaboration between the *Surface Science group* at the *Technische Universität Darmstadt*, and the *Group 2. Energy: Materials and Batteries*, at the *Institut de Chimie de la Matière Condensée de Bordeaux (ICMCB-CNRS)*. The experimental work presented here was selectively done in either laboratory, which will be named related to the data when necessary.

3.1 Thin film deposition

The development of techniques to deposit thin films has become essential due to the advanced technological requirements. At present, many of these techniques are based on the deposition of thin films on a substrate from a vapor phase generated by a physical or a chemical process.

3.1.1 PVD

In physical vapor deposition (PVD) the vapor is produced by physical processes which can occur in vacuum or at higher pressures. The main categories of PVD are vacuum deposition (evaporation), sputter deposition, laser ablation, epitaxy growth and ion deposition [150].

One of the most common techniques used to produce thin films is sputtering. In this process a target material is bombarded with energetic ions. The ionized gas is generated by an applied DC voltage between target and substrate forming a hot gas-like phase conformed by ions and electrons, called plasma. The charged atoms are accelerated to the target colliding with the atoms in the material and ejecting them to the gas environment. The ejected atoms will then travel towards the substrate and condense into a film. The electrons released during the gas ionization are accelerated to the anode substrate where new collisions with gas atoms occur, creating more free ions and electrons and thus giving a continuous production of these species. For the deposition of conductive materials, a DC power supply is used. However, for insulating or semi conducting targets, the use of a RF power supply is considered by applying an alternating current with frequencies higher than 50 kHz [150].

By adding a strong magnetic field near the target area in the system, the sputtering process is enhanced. These systems are called magnetron sputtering. The plasma generated is confined to an area where the magnetic field is stronger, causing faster deposition rates, greater gas ion replenishment and less substrate damage from stray particles. Figure 3.1 shows the target configuration when a magnetic field is applied to the vaporization process.

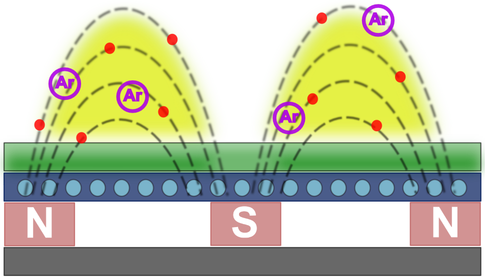

Figure 3.1: Schematic representation of the target configuration for a magnetron sputtering process.

Sputtering can be used to deposit elemental materials or compounds. The material vaporized will have the same composition as the bulk of the target. Nevertheless, elements in a compound target tend to have different volatilities, therefore there is a loss in stoichiometry in the final film compared to the starting target. The compensation of these losses can be done by including a reactive gas such as oxygen or nitrogen. This sputtering configuration is called reactive sputtering, and directly refers to deposited thin films of compounds formed from the reaction between the target and the environment gas present (N_2 or O_2) [150].

Thin films have generally particular properties which differ from the material in bulk form, and depend on the deposition parameters used. There are five main points that influence the properties of thin films [150]:

1. Substrate surface: morphology, chemistry, mechanical properties, surface defects, stability, and preferential nucleation sites.
2. Deposition process and system geometry: temperature deposition rate, gas contaminations.
3. Film growth on substrate surface: condensation, nucleation of adatoms, interface formation, surface mobility of adatoms, growth morphology of film, among others.
4. Intermediate processing.
5. Post deposition processing and reactions.

By having constant geometry, gas pressure, gas composition and target voltage, and current (power), a constant and reproducible plasma, and consequently thin films, can be produced.

By establishing a set of parameters, reproducible $LiCoO_2$, LiPON and ZrO_2 films were produced here using RF magnetron sputtering.

Samples were deposited either on titanium foil (Alfa Aesar 99.95%), silicon substrate stacks of $Si/SiO_2/TiO_2$ or $Si/SiO_2/TiO_2/Pt$ (GMEK), depending on the characterization technique. The targets employed were all 2 inches diameter, $Li_{1.0}Co_{1.0}O_2$ (FHR, 99.9%), Li_3PO_4 crystalline target (J.K. Lesker, 99.95%), and metallic Zr (J.K. Lesker, purity Grade 702). For the $LiCoO_2$ deposition a standard gas mixture of Ar/O_2 was used, for LiPON either pure N_2 or a gas mixture of Ar/N_2 was used, while for ZrO_2 an Ar/O_2 mixture. The total gas flow, which was generally used, was 10 sccm and a pressure of $8 \cdot 10^{-3}$ mbar, for all cases.

These experiments were performed in the Surface Science Group in Darmstadt, at the Daisy–Bat (Darmstadt integrated system for Battery research). The Daisy–Bat is an integrated cluster tool for in situ deposition and surface characterization of materials for battery applications. The films were deposited either at the ”Anode” or ”Electrolyte” sputtering chambers, as seen on Figure 3.2, and were either transported to the analysis chamber for XPS measurements or taken to the glove box, without breaking vacuum or exposing the sample to air. A transfer box can be attached to the load lock where quick transport of the sample can be made under vacuum or argon for further battery assembly.

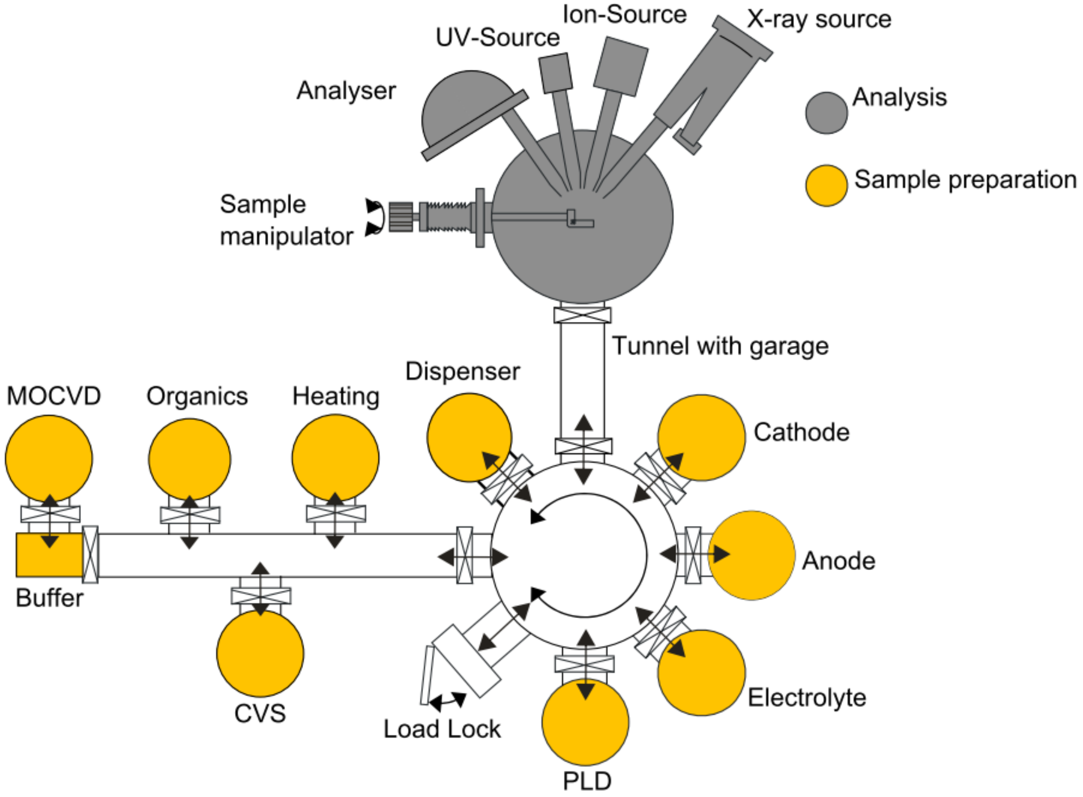

Figure 3.2: Daisy–Bat: DArmstadt's Integrated SYstem for BATtery research.

The deposition of $LiCoO_2$, ZrO_2 and LiPON was done in TU Darmstadt. Additional LiPON layers were deposited at the ICMCB-Bordeaux in a similar sputtering chamber. Thin films were deposited on aluminum and glass substrates for the determination of chemical composition (ICP) and electrochemical properties (EIS).

3.1.2 CVD

In chemical vapor deposition (CVD) the vaporization of atoms or molecules is done by high temperature reaction or decomposition of chemical precursors. The reaction between the species in gaseous phase will take place either on or near the substrate surface. The advantages that CVD has over other deposition techniques are the high growth rate, the deposition of materials which are hard to evaporate, the good reproducibility, and the growth of epitaxial films. With this technique it is possible to have a conformal coverage over all the substrate [150].

CVD can be classified by the final application of the material, the process and reactor used, by the precursor employed, and the chemical reaction taken place. Most of the

CVD processes use endothermic reactions so activation energy is needed. It can be provided by electrical heating, radio frequency induced heating, laser assistance and plasma enhancement among others. Some examples of materials that can be prepared by CVD are conductors, semiconductors, insulators/dielectrics, optoelectronic and optical layers, and coatings [151].

The experimental parameters determine the deposition rate and the characteristics and properties of the film. These variables include temperature, pressure, concentration of precursors, gas flow, reaction geometry, and operating principles. CVD processes are complex given the amount of steps occurring and the parameters that can be varied. Nevertheless the process is in equilibrium so it is possible to study the kinetics and thermodynamics involved. The two main factors involved in CVD processes are mass transport and surface kinetics. Figure 3.3 shows the different steps in a CVD process that can be classified as mass transport or surface reaction and are listed below [151].

1. Transport of the reactant molecules inside the reaction chamber.
2. Intermediate species formed.
3. Diffusion from the gas boundary to the surface.
4. Adsorption of species on the substrate.
5. Reaction/s at the substrate.
6. Desorption of product gases.
7. Transport of the product gases outside the chamber.

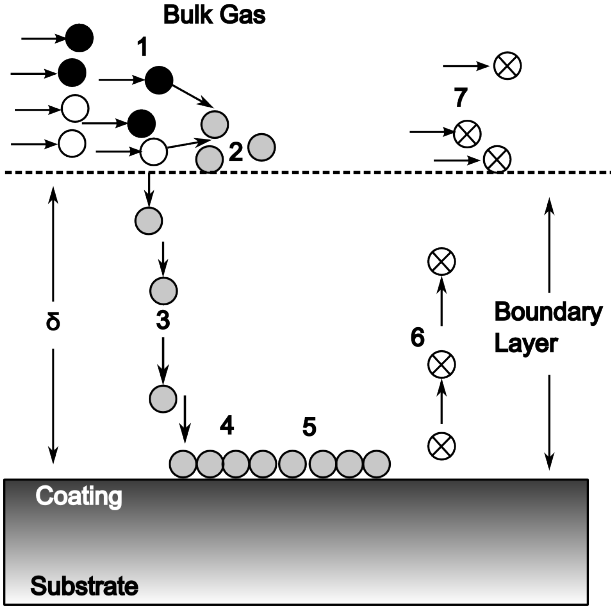

Figure 3.3: Diagram of the mechanistic steps that occur during a CVD process. Adapted from [151].

3.1.3 Aerosol Assisted CVD

A novel technique, which benefits from the basic principles of a CVD process fed by a micro delivery system based on nebulization of a starting solution, is introduced. The experimental setup is schematically depicted in Figure 3.4. This setup and implementation for thin film deposition of transition metal oxides was developed by Dr. Ing. Azad Darbandi (Nanomaterialien, Technische Universität Darmstadt).

The process includes an ultrasonic generator to produce the aerosol, which is later carried continuously to a hot evaporation zone. As the solvent is removed, the remaining vaporized precursor is transported to a subsequent reaction zone where the decomposition of precursor and deposition of the multicomponent thin film occurs.

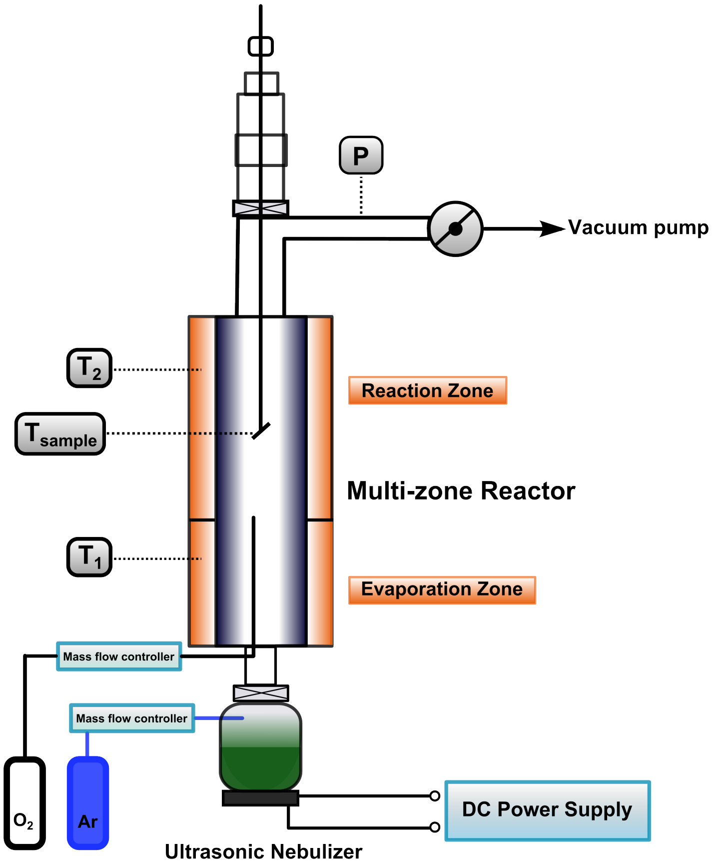

Figure 3.4: Nebulized chemical vapor deposition setup used for the thin film production

The precursor solutions were transformed into aerosol using an ultrasonic nebulizer (1.7 MHz). The aerosol was then delivered by a flow of gas to the reaction chamber build up by two furnaces which can be heated at different temperatures in spatially separated heating zones for evaporation and reaction (T_1 and T_2 in Figure 3.4). Both argon and oxygen gases were mixed at the reaction chamber. The temperatures of the furnaces were kept at 750°C (T_1) and 800°C (T_2) while the sample temperature was set to 850°C.

The $Li(NiMnCo)O_2$ (LNMCO) films were prepared on both platinum and silicon wafer substrates. Stoichiometric amounts of lithium acetylacetonate (Sigma Aldrich 97% purity), cobalt (III) acetylacetonate (Sigma Aldrich 98% purity), manganese (III) acetylacetonate (Sigma Aldrich, 99% purity) and nickel acetate tetrahydrate (Alfa Aesar 98% purity), were dissolved in methanol, testing different total ion concentrations, i.e 0.01, 0.025, 0.04, 0.05, and 0.07 mol/L. The final molar concentration of solutions was achieved from relative amounts of 1:1:1 of Co, Ni, Mn-precursors and a 20% excess of the lithium precursor.

In addition to investigating different concentrations, a variety of total gas pressures (P in Figure 3.4) were examined; 300, 500, 700 and 900 mbar. The average deposition rates observed were between 7 and 83 nm/min on experiments for varying the solution's concentration and between 12 and 46 nm/min when changing the pressure.

3.2 Material Characterization

As mentioned before, the production of thin film materials is a crucial part in the development of modern functional devices. Given that the final mechanical, chemical, electrical, magnetic and optical film properties are determined by the micro-structural qualities of the films, exhaustive material characterization has become an essential part in device development. In general, characterization of thin films focuses on surface analysis. For example, photoelectron spectroscopy is a technique which provides information on the energy level alignment at interfaces. The electronic and ionic energy levels and their relative position in a complex layer system, such as a battery stack, determine crucial parameters like ionic transport. The interaction between the different interfaces formed also have great impact on device behavior. Nevertheless, and due to the application of the materials studied here in batteries, stability, behavioral, and other functional bulk properties and characterization were also considered.

3.2.1 X-ray photoelectron spectroscopy

X-ray photoelectron spectroscopy is a technique based on the photoelectric effect, where a sample is illuminated with photons of a defined energy ($h\nu$). If the applied photon energy is higher than the ionization energy of the sample, electrons are emitted and can be detected by a photoelectric spectrometer. The energy provided by the absorption of a photon is employed to eject an electron, with a certain kinetic energy (E_{kin}), from a core level or valence level [152]. Considering the principle of energy conservation, the photon excitation energy $h\nu$ and the total initial energy of the system will be related to the final energy of the system and E_{kin}, as seen in Equation 3.1. E^1 and E^2 are the fundamental energies of the system at the initial state (neutral, N electrons) and at the final state (ionized, N-1 electrons), respectively. The energy difference between these states will give the ionization potential or binding energy E_B.

$$h\nu + E^1(N) = E^2(N-1) + E_{kin} \tag{3.1}$$

$$E_B = E^2(N-1) - E^1(N) = h\nu - E_{kin} \tag{3.2}$$

The ionization potentials corresponding to the core levels and the valence band are in the range of ≈ 30 to 1000 eV and 0 to 30 eV, respectively. XPS of core level states gives specific characteristics of each element probed, which is related to the charge of the atomic site and suffers variations with changing chemical bonds.

The ejected photoelectrons may lose part of the kinetic energy during the photoionization process, which can result in interactions and further excitations of a second electron towards an empty orbital, or to a complete emission of the electron. These two processes are called shake-up and shake-off, respectively. Additionally, when the liberated energy from the ejection process is high enough, Auger electrons are emitted, as seen in Figure 3.5 [152].

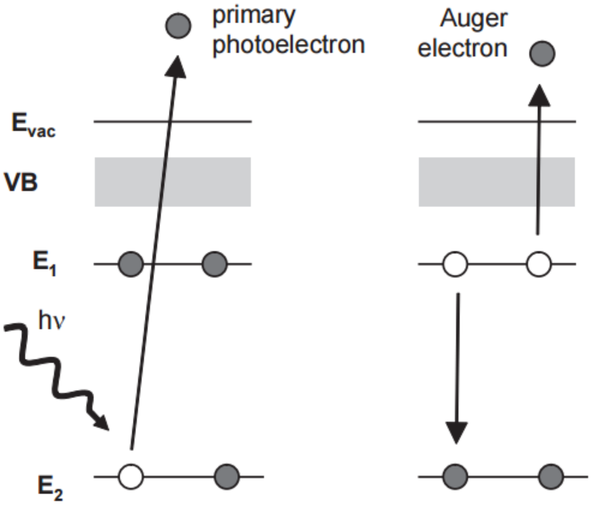

Figure 3.5: Energy level diagram for posible photoelectron processes occuring during XPS measurements. Adapted from [152].

The experimental determination of E_B of a metallic probe, in electric contact with the spectrometer, can be established by the thermodynamic equilibrium of the Fermi levels (E_F). The work function of the spectrometer, Φ_{SP}, is the difference between the Fermi level and the vacuum level. In this way, for conducting samples the binding energy can be determined by the relation expressed in Equation 3.3.

$$E_B = h\nu - E_{kin} - \Phi_{SP} \tag{3.3}$$

Nevertheless, this simple expression can not be applied for insulating samples, given the inhomogeneous residual charges left at the surface after the photoemission process. In these cases, a calibration procedure is necessary to determine the difference between the measured and real E_B.

The surface sensitivity is given by the mean free path (λ) of the photoelectron which varies with excitation energy and the samples probed. $h\nu$ photon energy from the K_α radiation of Al (1486.6 eV) or Mg (1253.6 eV) are generally found in XPS spectrometers. It is estimated that around 95% of the photoelectrons contributing to the spectra corresponds to 3λ, then the possible escape depth for a given element will be characteristic. Therefore, Al K_α has a maximum mean free path corresponding to less than 10 nm. Nevertheless, the surface sensitivity can be changed by variating the photon energy, E_{kin}, by using a synchrotron source for example. Another way of changing the surface sensitivity is by changing the electron emission angle. Nevertheless, the highest surface sensitivity that can be achieved is for E_{kin}=50 eV with a resulting mean free path of about 5Å, as seen in Figure 3.6 [152].

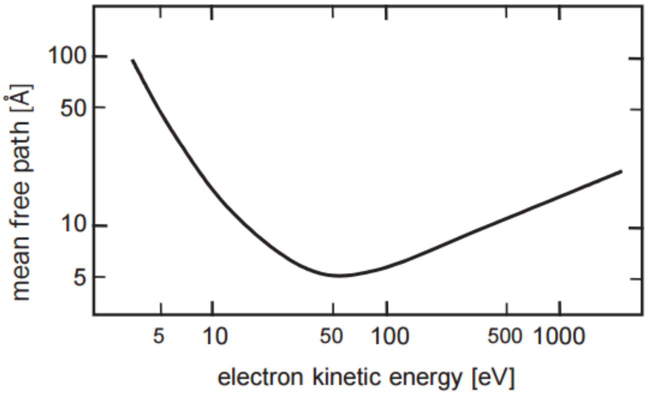

Figure 3.6: Inelastic mean free path of electrons in a solid related to the kinetic energy. The minimum found relates to the highest surface sensitivity, which can be obtained from 50 eV kinetic energy. Adapted from [152].

XPS is a useful technique which may help to determine the composition and electronic structure of surfaces. Effects of doping, chemical reactions on interfaces (solid/gas, solid/liquid and solid/solid), growth modes of thin films, chemical state of adsorbate, barrier heights at contacts, charge transport mechanisms, and diffusion processes at interfaces can be identified [152].

The used process to determine the chemical composition of layers with XPS was done by evaluation of the absolute intensities corrected with the sensitivity factors of the spectrometer [41, 153]. Even though results are highly reproducible, there are some factors that affect the correct determination from the peak intensity I, which depends on the density of atoms n, the photon flux per second f, the angular efficiency factor (angle between the photon path and detected electrons) θ, the mean free path of the photoelectrons in the sample λ, the photoelectrons detection efficiency y, the area probed A and the detection efficiency T. This relation is shown on Equation 3.4.

$$I = nf\sigma\theta y\lambda AT \tag{3.4}$$

The quantification of the intensity depends on the sensitivity factor (S) for each individual photoelectron line. Equation 3.5 relates the given intensity of the emission and the density of atoms n, for fixed spectrometer conditions.

$$I = \frac{n}{S} \tag{3.5}$$

$$\frac{n_1}{n_2} = \frac{I_1/S_1}{I_2/S_2} \tag{3.6}$$

By establishing the ratio between two elements, the set of values for the spectrometer constants will be established. In this way, the atomic fraction for any constituent in a sample c_x, will therefore be the ratio between the different elements (Equation 3.7)

$$c_x = \frac{I_x/S}{\sum I_x/S} \tag{3.7}$$

All XPS measurements performed in this thesis were done at the Daisy-Bat lab with a Physical Electronic VersaProbe XPS/UPS hemispherical analyzer unit with monochromated Al K_α radiation (hv = 1486.6 eV). The measurements were done with a pass energy of 23.50 eV.

3.2.2 Infrared spectroscopy

Infrared spectroscopy is a method which can be used for the direct qualitative analysis and detection of bond type, structures and functional groups, present in a material. This technique is based on the irradiation of a sample with a beam causing the electrical field to interact with fluctuations in the dipole moment of the molecule. Only when the frequency of the radiation matches the vibrational frequencies of the molecule the radiation will be absorbed causing a change in the amplitude of the molecular vibration. Given that the IR radiation frequency is between 0.78-1000 μm, it does not induce electronic transitions. Therefore, it can only cause differences in the vibrational and rotational modes of the molecules. The different regions in the IR spectrum are based on the wavenumber.

- Near IR: Region between 12500 - 4000 cm^{-1}.
- Mid IR: Most used region, located between 4000 - 650 cm^{-1}. It can also be further divided in two regions, 4000 - 1000 cm^{-1} where functional groups may be identified and below 1400 cm^{-1} where specific absorption bands of a material are probed, this is the so called fingerprint region.
- Far IR: In the region between 650 - 200 cm^{-1} the analysis of the weakest bonds may be done. This region is used for the study of organometallic or inorganic compounds.

Molecules have specific vibrational modes, which depend on their components and functional groups, and are classified as stretching or bending modes. Examples of these modes are shown in Figure 3.7. Stretching modes are related to symmetric and asymmetric vibrations which give changes in the inter-atomic distances along the bond axis. On the other hand, bending modes refer to movements like rocking, scissoring, wagging and twisting. IR spectra record the variation of transmitted or absorbed light as function of the wavenumber.

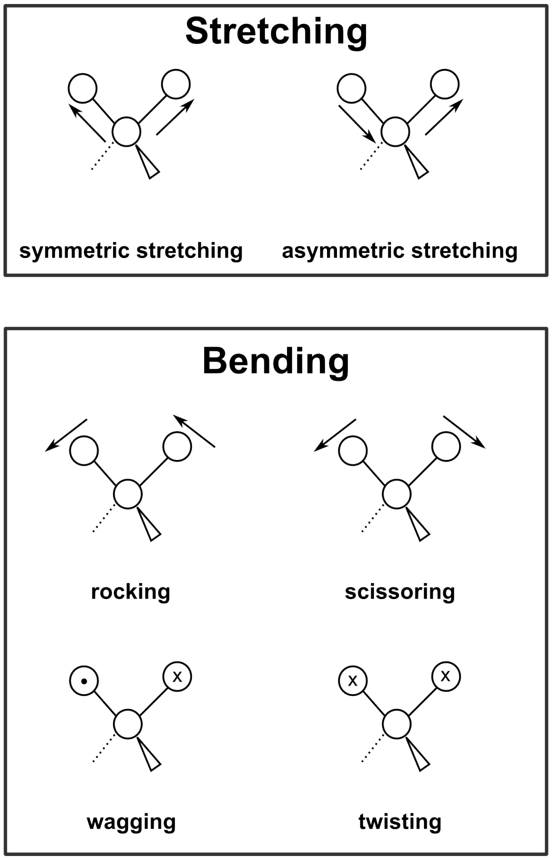

Figure 3.7: Stretching and bending vibrational modes.

IR spectroscopy was employed for the analysis of lithium phosphates and lithium phosphorus oxynitride film structure. Figure 3.8 presents the vibrational modes present in a tetrahedral molecule with general formula MA_4 with A1, E, and T2 represent the molecular symmetry groups, like the ones found for phosphates tetrahedrons. The T2 modes are IR active and triply degenerate [154, 155].

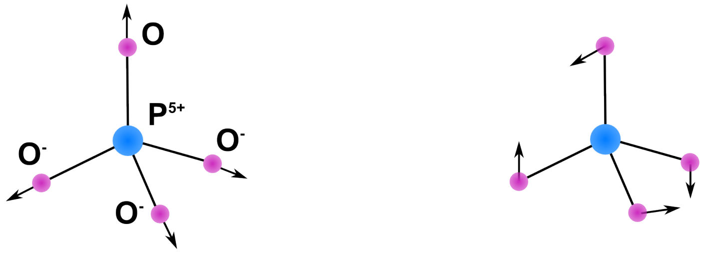

(a) ν_1(A1) **(b) ν_2(E)**

(c) ν_3(T2) **(d) ν_4(T2)**

Figure 3.8: Vibrational modes of a $PO_4{}^{3-}$ tetrahedron. Adapted from [155].

Modes ν_1 and ν_3 represent symmetric and asymmetric stretching, while ν_2 and ν_4 are related to the bending modes in a $PO_4{}^{3-}$ tetrahedron. The analysis of the peak position compared to standard reported values allows a proper identification of the molecular structure present in the sample. More information on the case of IR will be given in Chapter 7.

The IR transmission spectra were recorded on a Bruker Vertex 70 v spectrometer, working under vacuum and equipped with DTGS detectors and two beam splitters (KBr or mylar multilayer). A total of 200 scans were averaged with a resolution of 4 cm $^{-1}$. A glove bag was attached to the IR spectrometer which was used for the handling and exchange of samples.

3.2.3 Scanning electron microscopy and energy dispersive X-ray spectroscopy

SEM is used to image a surface by interaction of an electron beam directed towards the sample. The electron microscope focuses the entire image getting a detailed view of the thin film. When the primary electron beam impacts the sample, the electron beam will penetrate a determined depth, which will depend on the beam's energy and inversely depend on the atomic number of the probed material. The different interactions between primary electron beam and the sample will generate several scattering effects, which can be elastic or inelastic, corresponding to backscattered and secondary electrons, respectively. As the electrons only interact within a short range inside the surface, additional information can be obtained from these interactions, thus secondary electrons and back scattered electrons are detected. Considering the secondary electrons, which result from a inelastic scattering, the intensity of the collected signal gives information of the topography and morphology of the layer. On the other hand the back scattered electrons, resulting from elastic scattering, give information on the chemical composition. Highly energetic backscattered electrons may cause ionization of the atoms before leaving the surface, producing additional secondary electrons. The relaxation of these ions lead to the emission of X-rays or Auger electrons characteristic of each element present. The particular X-ray photon or Auger electrons emitted help characterize the chemical composition of the sample by applying SEM withan energy dispersive (EDS) mode. The characteristic X-ray emission lines of the cations of interest, present in the materials analyzed in this work, manganese, cobalt and nickel, are shown in Table 3.1.

Table 3.1: Photon energies, in keV, of principal K-, L-, and M-shell emission lines for Mn, Co and Ni [156, 157].

Element	$K\alpha_1$	$K\alpha_2$	$K\beta_1$	$L\alpha_1$	$L\alpha_2$	$L\beta_1$
Mn	5.89875	5.88765	6.490.5	0.6374	0.6374	0.6488
Co	6.93032	6.91530	7.64943	0.7762	0.7762	0.7914
Ni	7.47815	7.46089	8.26466	0.8515	0.8515	0.8688

At TU Darmstadt SEM and EDX measurements were performed with a Philips XL30 FEG High-resolution scanning electron microscope (HR-SEM) with EDX (energy dispersive X-ray spectroscopy), EDAX Genesis and Electron Backscatter Diffraction (EBSD). At the ICMCB-Bordeaux a JEOL 6700F (High resolution, Cryo-SEM analysis X) microscope was used. Measurements were performed by Sonia Buffière, Ingénieur d'étude at PLACAMAT, Université de Bordeaux.

3.2.4 X-ray diffraction

X-ray diffraction is the most common technique to study the crystalline structure of a material, and it can determine several parameters like lattice parameters, cell volume and degree of texturing. This technique also serves in the detection of impurity phases and evidences the presence of eventual structural disorder.

After the sample is irradiated, the diffracted X-ray beam occurs at a certain angle θ from a set of lattice planes separated by a distance d, as described by Bragg's law, as shown in Equation 3.8.

$$n\lambda = 2d\sin\theta \tag{3.8}$$

A well crystallized structure will have periodically arranged units which will scatter only at certain directions related to the different lattice planes present. Incident X-rays will interact with the these atomic planes creating interference with the incident beam when leaving the structure. In this way all the periodic distributions of electron density may be determined. On the other hand, amorphous materials will have overlappig X-ray scattering from many directions. This will give a broad band over a wide range of the 2θ values. The presence of these broader peaks are therefore a good indicator of the presence of amorphous phases or a not fully crystallized material. Spectral results are analyzed with the PDF database which gives information of the crystal structure present in the film planes of symmetry.

In the TU-Darmstadt, XRD patterns of the $Li(NiMnCo)O_2$ films were recorded on a Bruker D8 diffractometer with angular range between 15 and 80° 2θ with a step size of 0.03° and a scan rate of 2 s per step.

Analysis of the diffraction data of a set of samples was performed using the Rietveld method with the program TOPAS 4.2 (Bruker AXS, Karlsruhe, Germany) [158]. To determine the degree of texturing, the model of March and Dollase [159] was used to correct the reflections' intensities for (0 0 1) texturing with the factor O_k (Equation 3.9), where α describes the angle between the lattice plane under consideration with the (0 0 1) plane and G_1 is a refined parameter. Therefore, $G_1 = 1$ gives no influence of texturing, whereas $G_1 \ll 1$ indicates strong texturing perpendicular to the (0 0 1) plane.

$$O_k = [G_1^2 \cdot \cos^2\alpha + (\frac{1}{G_1} \cdot \sin^2\alpha)]^{-1.5} \tag{3.9}$$

The XRD of $LiCoO_2$, ZrO_2 and LiPON were measured with a Seifert PTS 3003 diffractometer using a Cu anode and an X-ray mirror on the primary side. On the secondary side a long Soller slit and a graphite Monochromator was used to separate the Cu K_α line, operated at 40 mA and 40 kV. These measurements were performed by Dr. Joachim Brötz (Kompetenzzentrum Materialcharakterisierung, Technische Universität Darmstadt)

In the ICMCB-Bordeaux a Bruker D8 Advance diffractometer was used with a Göbel mirror as primary optics and a theta-two theta diffractometer when measuring grazing incidence X-ray diffraction. This last variation of diffraction analysis is used to obtain microstructural information in directions parallel to the substrate, different from conventional Bragg diffraction where the direction analyzed is perpendicular to the interface. This technique has been developed for very thin films that can not be probed with conventional diffraction methods [160].

3.2.5 Inductively coupled plasma spectroscopy

Inductively coupled plasma spectroscopy (ICP) is a technique employed for chemical analysis and composition of materials. This method uses argon plasma as source of ionization and excitation. The ICP source is in the form of a white, intense and bright flame. The plasma temperature oscillates between 6000 and 7000 K, which allows the dissociation of molecular species to excited atoms and free ions. The emission of UV-Vis photons are expected when these ions return to their fundamental state. The quantification of the photons received by the photomultiplier when compared to the calibration from a reference solution. Apart from halogens, oxygen and nitrogen, this technique allows the identification of a large amount of elements in solution with high sensitivity.

ICP was applied for LiPON layers prepared in ICMCB-Bordeaux for the determination of Li and P ratio. The wavelength of the emission lines for Li and P are 460.289 nm and 214.914 nm, respectively. Thin films were deposited on aluminum foil which were later dissolved in boiling Aqua Regia (HCl:HNO_3 1:2) solution. Triplicates of these measurements were done for a good statistical base. ICP was performed by Laetitia Etienne, assistant Ingénieur at ICMCB-Bordeaux, using a Varian 720ES spectrometer.

3.2.6 Electroanalytical techniques

The electrochemical characterization of a material focuses on the changes caused by an external perturbation leading to the passage of electrical current and the generation of electrical voltage due to chemical reactions [48].

The electrochemical performance of the material was measured using a Swagelok type cell assembled in an argon filled glove box with Li metal as the anode and lithium hexafluorophosphate solution, $LiPF_6$ 1 M in ethyl carbonate-diethyl carbonate 1:1 (UBE Industries ltd.) as the electrolyte. Thin films were generally deposited on titanium substrates, which act as current collector in the battery.

3.2.6.1 Cyclic Voltammetry

Cyclic voltammetry (CV) applies a linearly changing voltage (ramp) to the electrode as a function of time while registering the changes in the induced current. When the potential reaches the value at which the electrochemical reaction takes place, the current measured increases proportionally to the amount of lithium exchanged This current peak identifies the potential at which the reaction occurs. For the majority of the cases addressed in this thesis, cyclic voltammetry was performed between 3–4.2 V using a scan rate of 0.05 mV/s, unless stated differently.

3.2.6.2 Galvanostatic cycling

During galvanostatic cycling (GC) a constant current is applied to the electrode during charge and discharge, where the potential change is recorded as a function of time. For the tests performed on the materials developed in this thesis a current of ± 1 μA between 3 and 4.2 V, was generelly applied, unless stated differently.

3.2.6.3 Electrochemical impedance spectroscopy

Both cyclic voltammetry and galvanostatic cycling are techniques that build on the electrical response in relation to the change in impedance at the electrode/electrolyte interface.

The ionic conductivity of thin films was determined by performing EIS measurements. Impedance can be described as the ability of a circuit to resist a flowing electrical current. EIS is measured by applying an AC potential to an electrochemical cell, where the current response is measured. This approximation can be done by associating the impedance response to an equivalent circuit, which is a model used to interpret simple impedance data. Most of the circuits are made of common electrical elements like resistors, capacitors, and inductors.

The AC potential applied generates changes in the real and imaginary parts of the impedance, which are computed as a function of the frequency. The overall shape of the response in the complex plane is characteristic for very specific mechanism present. For example, a straight line with slope = $\pi/4$ is related to the diffusion process which creates an resistance called Warburg impedance (W). A semicircle corresponds to a simple electron transfer which includes capacitance in parallel with a resistance. The combination of diffusion and kinetic processes will lead to a model with a capacitance and a charge transfer impedance (W). The equivalent circuits considered for electrode-electrolyte-electrode and battery configurations studied here are shown in Figure 3.9 (a) and (b), respectively. The corresponding Nyquist plot for each case show the variation of the frequency with the real and imaginary part, Z' and Z".

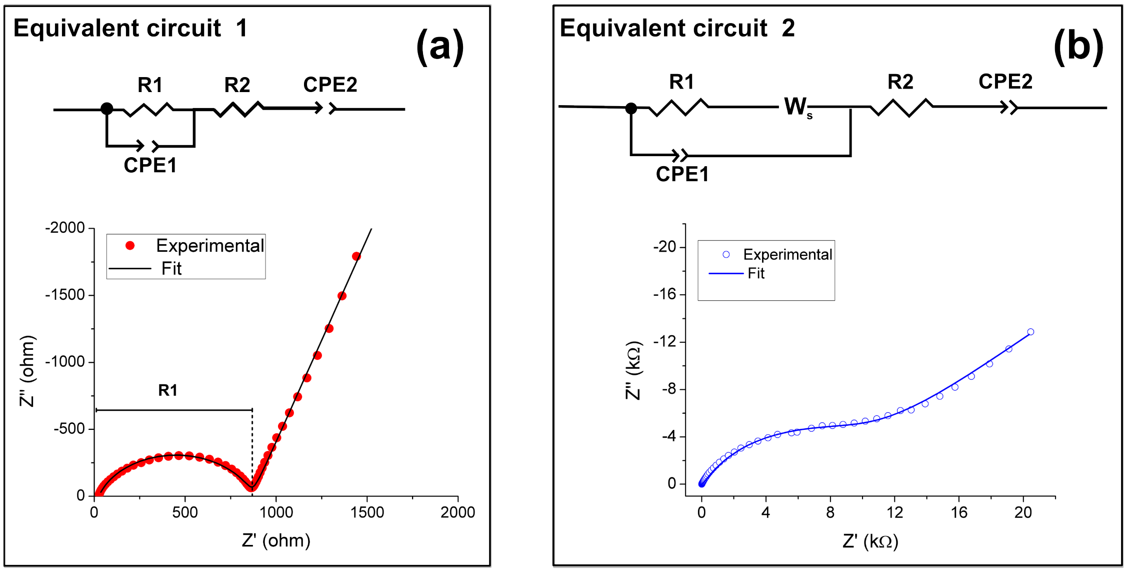

Figure 3.9: Impedeance spectra of a thin film electrolyte and the corresponding fit with the equivalent circuit for (a) electrode-electrolyte-electrode and (b) battery configurations.

The ionic conductivity of thin films (σ) in the electrode-electrolyte-electrode configuration was calculated using the resistance R obtained from the Nyquist plot. The R1 is used in Equation 3.10 where d is the layer thickness and A the area of the done.

$$\sigma = \frac{1}{R} \times \frac{d}{A} \tag{3.10}$$

For the determination of the ionic conductivity of LiPON in ICMCB-Bordeaux, sputtered films were deposited on glass substrates with copper (Cu) current collectors, 200 nm thick. These blocking electrodes were also deposited by sputtering using a metallic Cu target and an argon plasma. Figure 3.10(a) shows the configuration of the impedance cell on a glass substrate showing the sandwich structures (area 4 mm^2) where the measurements are taken.

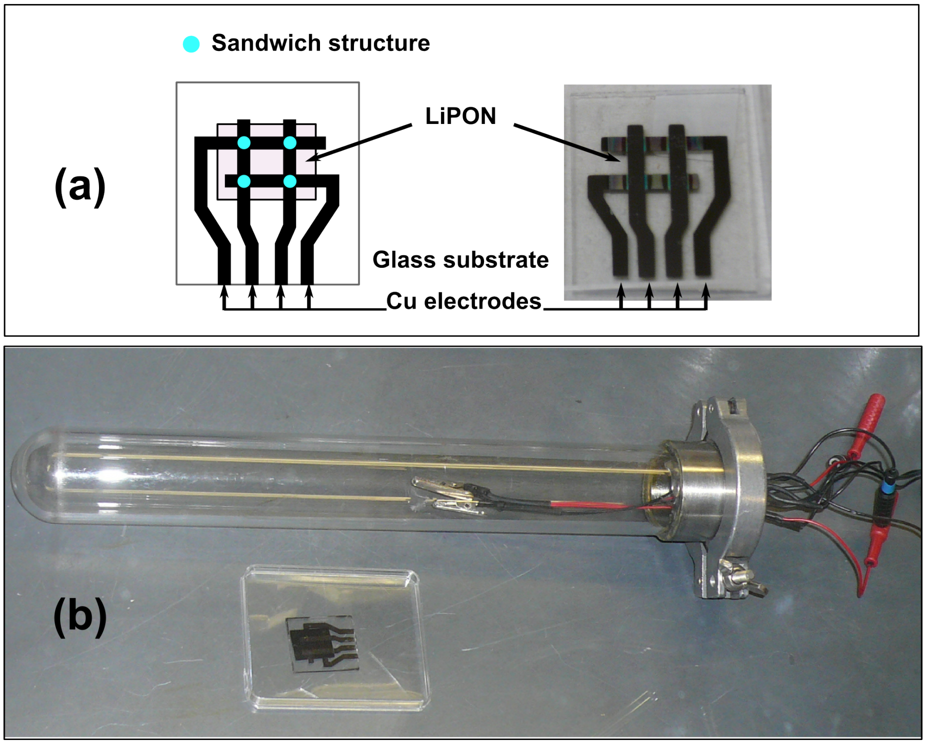

Figure 3.10: Impedance measurement device and cell and configuration of a sandwich structure with electrode/LiPON/electrode [42].

The measurement device available at ICMCB-Bordeaux (Figure 3.10(b)) has the advantage of having the cell inside a closed argon environment during measurements, which is useful for air sensitive samples. The glass device can be connected to a furnace and register the change in conductivity as function of temperature to determine the activation energy (E_a) or energy necessary to have the mechanism of conduction. By using the Arrhenius expression (Equation 3.11), the E_a can be calculated from the relation between ionic conductivity σ and temperature T.

$$\sigma = \sigma_0 exp(-\frac{E_a}{kT}) \tag{3.11}$$

At TU Darmstadt, the cell impedance of batteries were measured directly before and after the respective electrochemical test. For LiPON films, the layers were deposited using $Si/SiO_2/TiO_2/Pt$ (GMEK) substrates with a gold blocking layer on top. The impedance measurements were generally done with a 10 mV AC excitation signal between $5 \cdot 10^5$–0.1 Hz.

Chapter 4

Thin film cathode materials

This chapter presents the deposition of thin film cathode materials. The routes employed to deposit such materials were physical vapor deposition (PVD) and chemical vapor deposition (CVD). PVD was used for the deposition of $LiCoO_2$ which serves as standard material for comparison, while a novel deposition method was used as a route to obtain thin films of $Li(Ni_xMn_yCo_{1-x-y})O_2$ ($Li(NiMnCo)O_2$). A comparison of sputtered $LiCoO_2$ and $Li(NiMnCo)O_2$ is made in terms of structure and electrochemical performance.

$Li(NiMnCo)O_2$ cathodes have been studied thoroughly in the past decade for Li-battery applications [161–164]. Since the first published work on the synthesis of $Li(Ni_{1/3}Mn_{1/3}Co_{1/3})O_2$ by Ohzuku and Makimura [165] much effort has been focused on the deposition of thin films positive electrode materials as replacement of $LiCoO_2$. Nevertheless studies on the deposition of these materials with CVD are scarce [64]. The key point for high quality thin films with chemical vapor processes is the optimization of deposition parameters, e.g sample temperature, concentration of precursor solution, carrier gas and flow rate [88, 92, 95].

This chapter focuses on the synthesis of cathode materials which are comparable to the standard positive electrode in terms of surface homogeneity and chemical activity.

4.1 $LiCoO_2$ thin films

The deposition of $LiCoO_2$ thin films was done by rf magnetron sputtering. As the chamber employed was newly built, the starting point was to perform a screening and determination of the best deposition parameters based on chemical composition. These results were used subsequently to obtain thin films with the best electrochemical activity possible.

4.1.1 Deposition of rf magnetron sputtered thin films

Details of the PVD setup used in this part is described in Section 3.1.1. The initial experiments included the variation of deposition temperature, rf sputtering power and the gas ratio (Ar:O_2). All experiments were made under a total gas pressure of $8{\cdot}10^{-3}$ mbar. Table 4.1 summarizes the experimental parameters used in this section. Chemical composition and electrochemical activity were determined by XPS measurements and cyclic voltammetry, respectively. All samples were deposited on titanium foil for 2 h.

Table 4.1: Summary of deposition parameters employed for the $LiCoO_2$ thin film deposition screening.

Sputtering parameters	**Other**
Temperature (°C)	
450	
500	*with Ar:O_2 1:1,*
550	*50 W power.*
600	
rf Power (W)	
35	
40	*at 550° C,*
50	*Ar:O_2 1:1.*
60	
Gas Ratio (Ar:O_2)	
1:1	
2:1	*at 550° C,*
3:1	*50 W power.*

4.1.2 Results

4.1.2.1 Determination of sputtering parameters

XPS was employed to determine the elemental composition based on the core level peak areas from Li 1s, Co 2p, and O 1s spectra. Figure 4.1 shows the normalized values of the elemental atomic percentage of each layer in each set of experiments performed (Section 3.2.1). Figure 4.1 shows the resulting layer composition of each set of experiments.

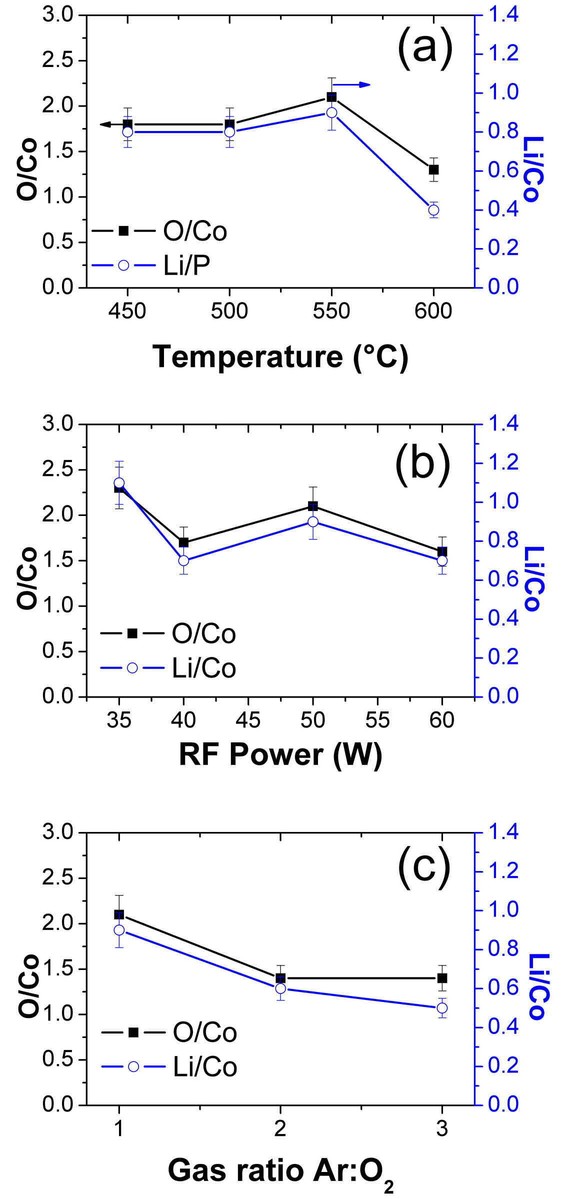

Figure 4.1: O/Co and Li/Co ratios of $LiCoO_2$ thin films deposited with different parameters (a) Temperature: 450, 500, 550 and 600°C; (b) rf power: 35, 40, 50 and 60 W; and (c) Gas ratio Ar:O_2: 1, 2 and 3.

4.1.2.2 Deposition temperature

Results on Figure 4.1.(a) evidence a change in composition when the temperature is increased over 550°C. Depositions at lower temperatures seem to not affect the relation between components, while at 600°C there is an apparent loss of material evidenced by the low amounts of lithium and oxygen in reference to cobalt.

Figures 4.2 show the CV curves of layers prepared at different temperature with 50 W rf power and Ar:O_2 1:1.

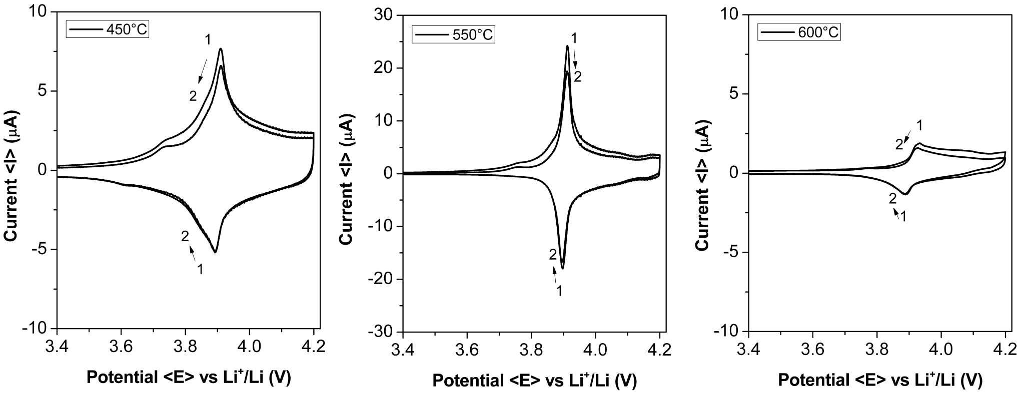

Figure 4.2: Cyclic voltammograms for sputtered $LiCoO_2$ thin films at different temperatures (a)450°C, (b)550°C and (c)600°C.

Prior studies on sputtered $LiCoO_2$ describe how high temperature (HT) phase $LiCoO_2$ can be deposited at room temperature and then annealed between 400-650°C and present the R-3m symmetry [166]. As an example, Figure 4.3 provides the XRD pattern for the $LiCoO_2$ film prepared at 550°C. The pattern has reflections from (0 0 3) found at 18.8°, (1 0 1) and (0 1 2), observed between 37°-39° and the main peaks from the titanium substrate. XRD shows a polycrystalline structure shows a preferred (0 0 3) orientation in line with reported layers sputtered on Ti foil [167–169]. Bohne et al. have found that metallic substrates, due to possible oxidation and O-termination of the surface, favor the formation of (0 0 3) texture [168].

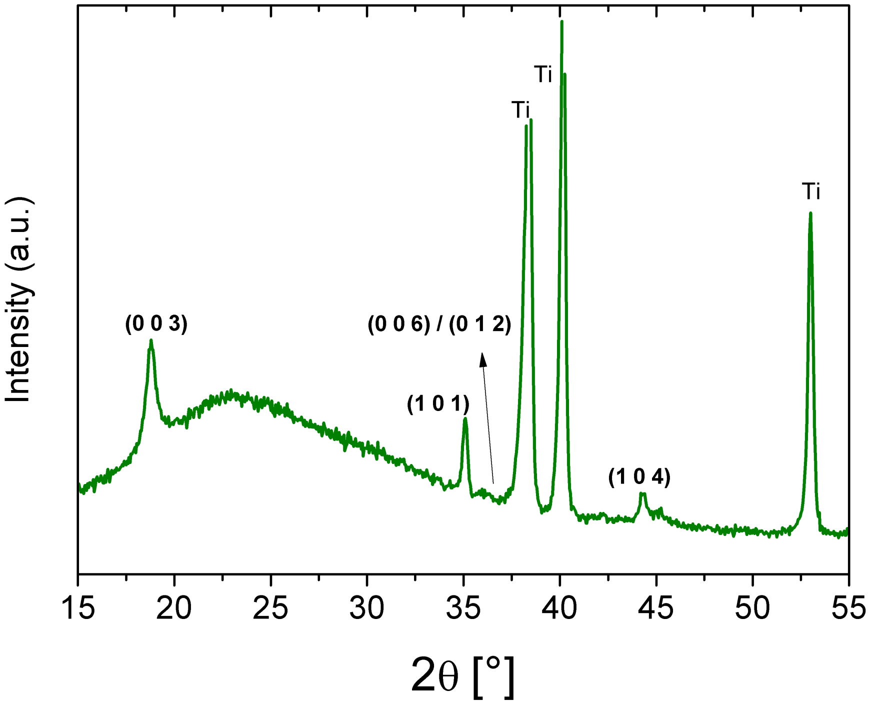

Figure 4.3: XRD pattern of sputtered $LiCoO_2$ thin film on titanium foil prepared at 550°C, 50 W and O_2:Ar 1:1.

Prior results from the group concluded that 550°C seems to be the optimal temperature for $LiCoO_2$ deposition [24, 166], the reason why it was chosen for the subsequent experiments as the working temperature which delivers hexagonal crystal structure with no additional phases. XPS spectra recorded for the surface layer, seen on Figure 4.4, shows features for stoichiometric $LiCoO_2$ in accordance to sputtered layers deposited at similar parameters [24, 166].

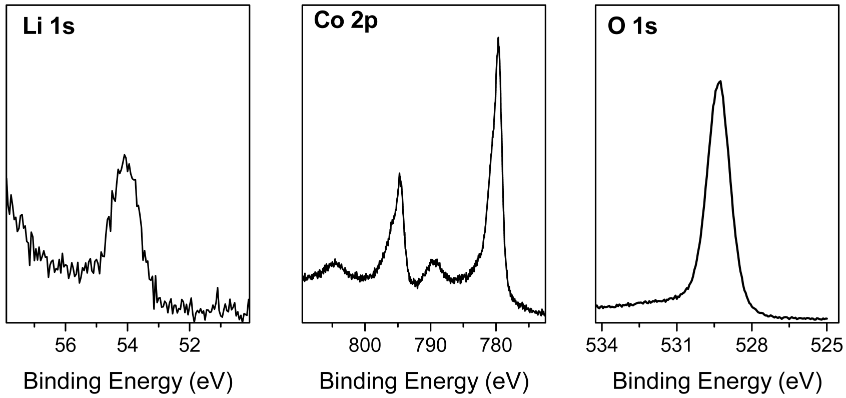

Figure 4.4: XPS spectra of core Li 1s, Co 2p and O 1s from $LiCoO_2$ thin film deposited at 550°C, 50 W and O_2:Ar 1:1.

4.1.2.3 rf sputtering power

Figure 4.1.(b) shows the variations of film composition with changing rf power in the sputtering process. The ideal value seems to be depositions at 50 W given that both lithium and oxygen are in correct proportion in relation to cobalt. Lower powers seem to favor over stoichiometric films, indicating the formation of impurity phases.

The CV of the first two cycles of thin films deposited at 550°C and 1:1 O_2:Ar ratio, with different rf powers are shown on Figure 4.5. Samples prepared at 35 W and 40 W were cycled from 3-4.4 V while the layer prepared at 50 W was cycled from 3-4.2 V. The CV curve of sample prepared at 50 W shows the typical features of a well crystallized HT-$LiCoO_2$ with sharp oxidation and reduction peaks. For the two first cycles the peaks appear at 3.92 V and reduction at 3.90 V. Samples at 35 W and 40 W, on the other hand, have shifted cathodic peaks to higher voltages while anodic moves to lower. The lower peak current intensity after the first cycle could indicate a performance decay due to the formation of SEI layer [164].

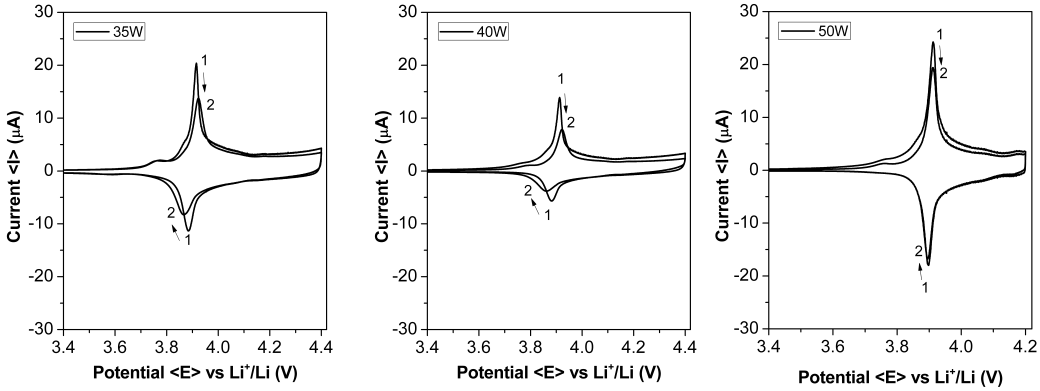

Figure 4.5: Cyclic voltammograms for sputtered $LiCoO_2$ thin films with different rf power (a)35 W, (b)40 W and (c)50 W.

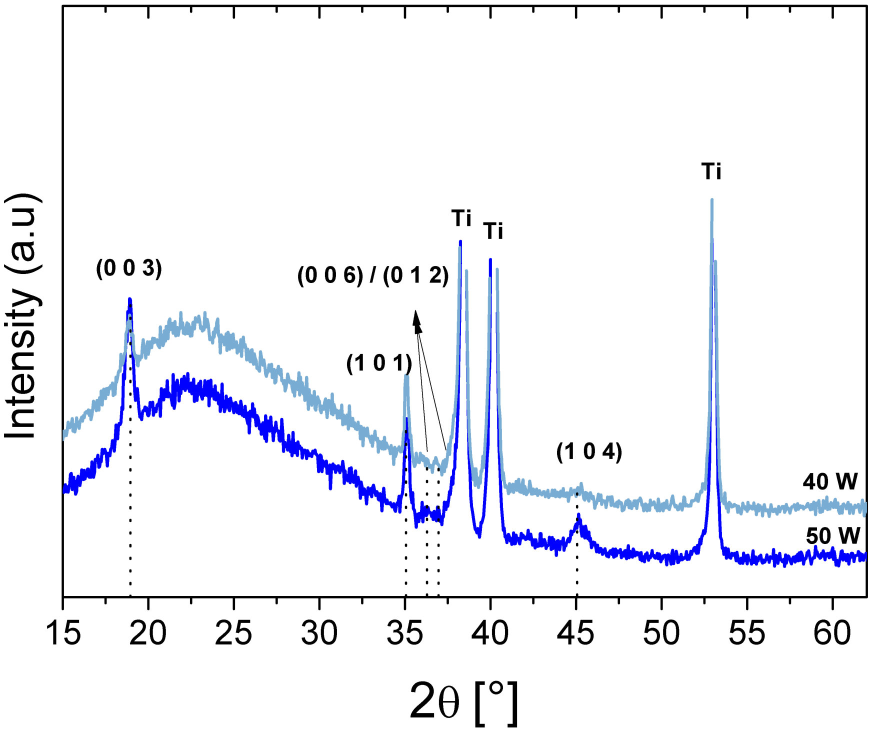

Figure 4.6: XRD patterns for sputtered $LiCoO_2$ thin films deposited with different rf power:40 and 50 W.

Figure 4.6 presents the XRD of samples deposited at 40 and 50 W. Both patterns present similar features, nevertheless the layer done at higher rf power has a clearly increased intensity of the (0 0 3) reflection and a possible appearance of the (0 0 6) reflection. These findings are in accordance with prior results of $LiCoO_2$ sputtered films on platinum which showed how higher rf power delivers layers with preferential (0 0 l) texture, while lower powers gives mixed (1 0 1) and (1 0 4) texture [168].

4.1.2.4 Ar:O_2 gas ratio

The composition of films prepared at 550°C and 50 W with different oxygen ratios in the gas mixture are shown on Figure.4.1.(c). The decreasing amount of oxygen in the total gas flow clearly affects the stoichiometry of the film. Results show a loss of both elements when working at low oxygen ratio, thus being not enough for the desired composition. Interestingly both samples with lower oxygen in the gas ratio showed similar results (2:1 and 3:1 for Ar:O_2).

Figure 4.7 presents the cyclic voltammetry curves measured from 3-4.2 V for samples prepared at different Ar:O_2 flows. Films are electrochemically active and present similar behaviors as with a 1:1 ratio. No shift in the cathodic or anodic peak is observed and the decrease after the first cycle seems to be in the same proportion. Nevertheless decreasing the amount of oxygen (samples 2:1 and 3:1) maintain the peaks' sharp features evidencing good crystallinity as seen for sample 1:1. As a particular point, when the amount of oxygen is lowest, an additional peak is observed at around 4.07 V after the first cycle. Several authors have attributed this peak to an order-disorder transition near composition $Li_{0.5}CoO_2$. [166, 170, 171].

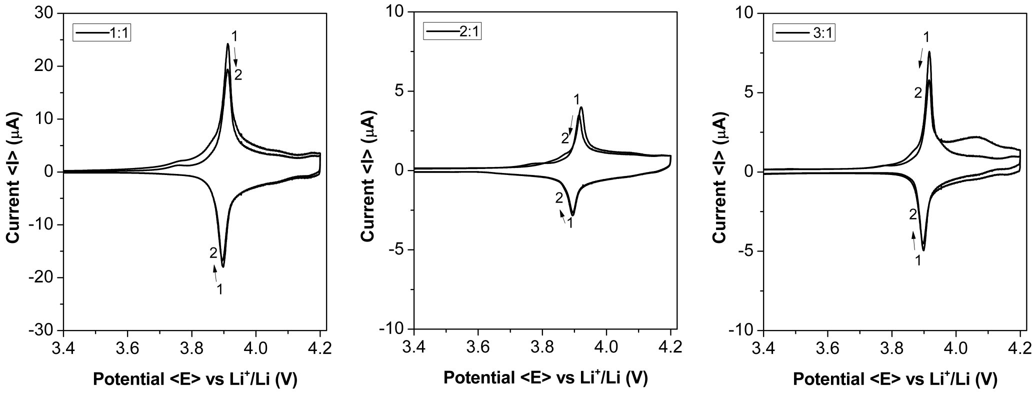

Figure 4.7: Cyclic voltammograms for sputtered $LiCoO_2$ thin films with different gas ratios Ar:O_2 (a)1, (b)2 and (c)3.

The different sputtering parameters clearly affect the chemical composition and electrochemical behavior of the material. Based on the results shown until now, the best deposition parameters in terms of composition and electrochemical CV activity are 50 W, 550°C and 1:1 Ar:O_2. These parameters will serve as standard for further experiments with $LiCoO_2$ addressing as for possible coating with artificial surface layers.

4.2 Li(NiMnCo)O_2 thin films

The ultrasonic nebulized CVD process was used for the deposition of thin films of Li(NiMnCo)O_2 on silicon and platinum substrates. The deposition was studied as a function of the working pressure and precursor solution concentration as mentioned in Section 3.1.3. Phase composition, structure and morphology of thin films was investigated in dependence of the different deposition parameters.

Given the higher difficulty CVD has to obtain homogeneous layers and also considering this novel process. A more detailed study on the deposition of Li(NiMnCo)O_2 was done and will be presented in this section.

4.2.1 Film Analysis and Characterization

X-ray diffraction (XRD) was employed to determine the composition and structure and texture of the deposited films. XRD measurements were performed on a series of samples prepared from different precursor solution concentrations and working pressures.

SEM imaging was used to determine the density, homogeneity, and particle morphology, while EDX was used to determine the composition of the films. Thin films were deposited on (1 0 0) oriented silicon (Si) for providing a smooth surface and the possibility to provide a sharp cross section cut. SEM imaging of the cross sections was used to measure film thickness and could be used to estimate the deposition rates for different process parameters. Nevertheless films tend to be porous towards higher concentrations and working pressures.

4.2.2 Results and Discussion

At first, films were deposited on silicon substrates to study the effect of precursor solution, concentration, and deposition pressure on the structural properties of the films.

4.2.2.1 Variation of precursor solution concentration

Figure 4.8 shows the XRD patterns of Li(NiMnCo)O_2 layers deposited at 900 mbar and 850° C for a series of precursor solution concentrations: 0.01, 0.025, 0.04, 0.07 $moll^{-1}$.

The data shows that for all the conditions crystalline Li(NiMnCo)O_2 phase was deposited with different degree of texturing depending on the deposition conditions. Additionally, the formation of Li_2SiO_3 and Li_2MnSiO_4 phases were observed. The presence of these phases and their effect on the films will be discussed later.

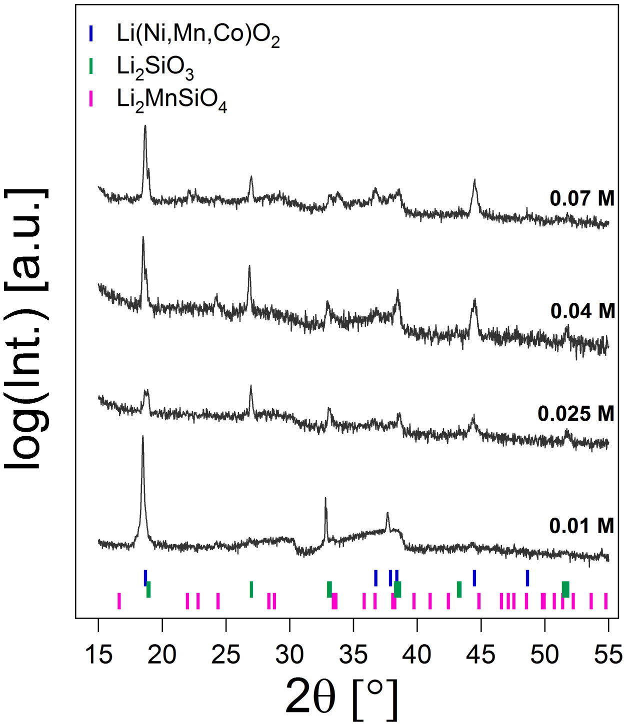

Figure 4.8: XRD patterns of Li(NiMnCo)O_2 layers prepared at 900 mbar and 850°C from different precursor solution concentrations: 0.07, 0.04, 0.025 and 0.01 $moll^{-1}$. Vertical lines denote Li(Ni,Mn,Co)O_2, Li_2SiO_3 and Li_2MnSiO_4 phases.

As prepared thin films crystallize in the trigonal $LiCoO_2$ type structure with space group R-3m. The lattice parameters and cell volume data, shown in Table 4.2, exhibit no significant change for different precursor solutions. The values are in good agreement with reports in literature for hexagonal α-$NaFeO_2$ layered structures with $LiNi_xMn_yCo_{1-x-y}O_2$ ($0.2 \leqslant x,y \leqslant 0.4$) stoichiometry and corresponding reflections for (0 0 3), (1 0 1), (0 0 6) (1 0 2) and (1 0 4) [81, 172–174].

Rietveld analysis was used to determine the degree of preferred orientation of the films. The values of March-Dollase parameter for all the layers are also shown in Table 4.2. A smaller March-Dollase parameter G_1 will indicate the preferred orientation perpendicular to the (0 0 1) lattice plane. A rough classification of texture related to the G_1 parameter can be given as follows: 1-0.9, no texture is present; from 0.8-0.6, some texture is present; and less than 0.5, very strong texture is present.

Table 4.2: Results of the Rietveld analysis of the diffraction patterns of the Li(NiMnCo)O_2 layers prepared at different precursor solution concentration. (*Not determinable due to very strong texturing)

Concentration (mol/L)	**a (Å)**	**c (Å)**	**V (Å^3)**	**March-Doll. (001) G_1**
0.010	*	14.248	*	0.3
0.025	2.875	14.236	101.90	~ 1
0.040	2.856	14.265	100.77	0.95
0.070	2.865	14.274	101.45	0.95

Figure 4.8 shows how the relative intensity of the (0 0 l) increases for low concentrations of the precursor solutions. The main presence of these peaks, (0 0 3) and (0 0 6) at 2θ = 18.7° and 37.9° respectively, is an indicative for strong texturing. Rietveld analysis confirms the (0 0 l) texturing for low precursor concentration, i.e. they present a low G_1, compared to the rest of the series, where no texture is observed.

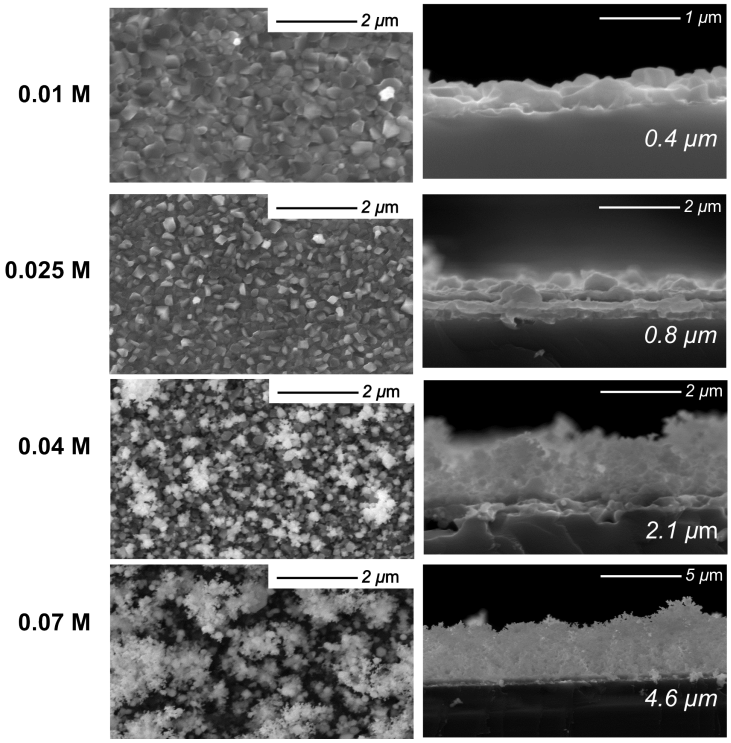

Figure 4.9: SEM images of Li(NiMnCo)O_2 layers prepared at 900 mbar and 850°C from different precursor solution concentrations: 0.07, 0.04, 0.025 and 0.01 moll^{-1}. Images on the right present film thickness for each case.

SEM images (Figure 4.9) show layers at lower concentration having a more compact structure with large grains while the rest are less dense composed of particles with bulky tree-like shape. This morphology is found frequently for thin film cathode materials prepared with similar deposition routes. For example, Chen and co-workers obtained a similar fractal-like porous morphology with Electrostatic Spray Pyrolysis [95], while Loho et al. [175] prepared textured films of $LiCoO_2$ deposited by a laser-assisted CVD route on silicon, being in agreement with the findings reported here.

4.2.2.2 Variation of total process pressure

Figure 4.10 shows the X-ray diffraction (XRD) patterns of Li(NiMnCo)O_2 layers deposited at different pressures during the process with a starting solution of 0.05 moll^{-1}. The formation of the Li(NiMnCo)O_2 phase with additional impurities, labeled on the patterns, was confirmed with XRD. Diffraction patterns show different degree of texturing for films prepared with variation of total pressure in the chamber. (0 0 l) indexed reflections have a significantly higher relative intensity at lower pressures.

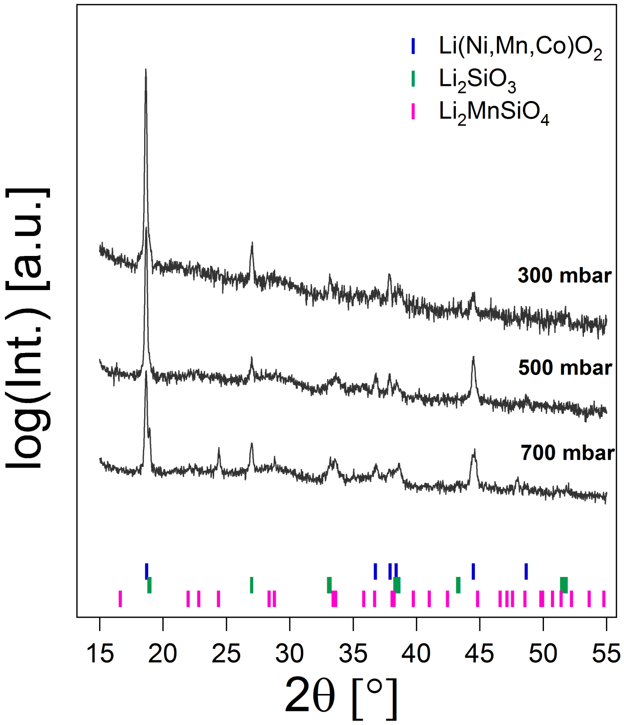

Figure 4.10: XRD patterns of Li(NiMnCo)O_2 layers prepared at different pressures: 300, 500 and 700 mbar, at 850°C from a solution 0.05 moll^{-1}. Vertical lines denote Li(Ni,Mn,Co)O_2, Li_2SiO_3 and Li_2MnSiO_4 phases.

Table 4.3 shows Rietveld analysis results for the lattice parameters and G_1 texturing parameter. The calculated data shows that the lattice parameters and cell volume do not change significantly and again agree well with literature reports for Li(NiMnCo)O_2 [81, 172–174]. It is observed that these films have some texture in comparison to films prepared at 900 mbar. Thus this is indicative that a lower process pressure promotes texturing and results in denser films. Moreover, the films deposited at lower pressures are apparently purer.

Table 4.3: Results of the Rietveld analysis of the diffraction patterns of the Li(NiMnCo)O_2 layers prepared at different pressures.

Pressure (mbar)	**a (Å)**	**c (Å)**	**V (Å^3)**	**March-Doll. (001) G$_1$**
700	2.863	14.283	101.42	0.71
500	2.864	14.248	101.18	0.60
300	2.866	14.284	101.61	0.44

Figure 4.11 shows the morphology of the films deposited at different working pressures. At high pressures particulate morphology is observed while films deposited at low pressures are dense with larger grains. The trend observed for increasing pressure resembles the behavior seen when the precursor concentration is increased. These films deposited at lower total pressures in the chamber present large grains with a more compact structure, while the rest of the samples are composed of particles with bulky tree-like shape and are less dense.

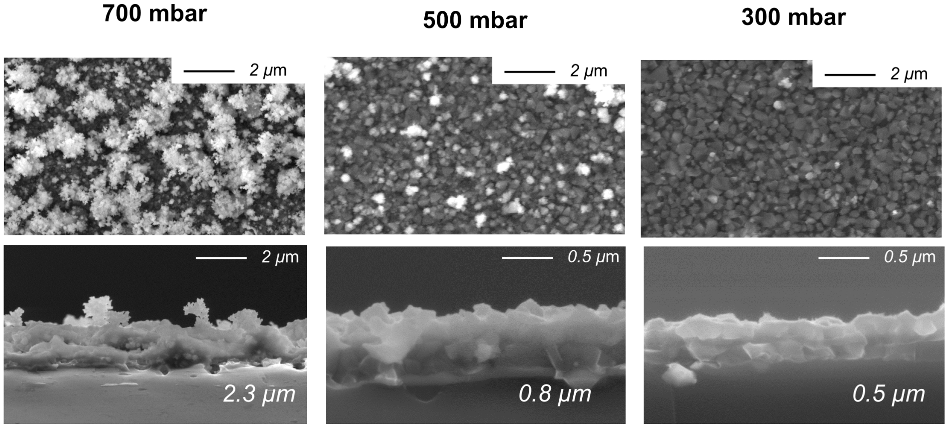

Figure 4.11: SEM images of Li(NiMnCo)O_2 layers prepared with different pressures: 300, 500 and 700 mbar, at 850°C from a solution 0.05 moll^{-1}. Images on the bottom present film thickness for each case.

The morphology observed at lower process pressures and concentration of precursor solution is in agreement with layer growth on a substrate under conditions of low supersaturation, i.e. low nucleation rate, and/or high surface diffusion [176] which is in line with the occurrence of texture. Oppositely, at high pressure (or precursor concentration) the films present low texture and low density, which consist of 100 nm particle size range. It is then possible to assume that for increasing pressures, particles are more likely to be formed in the gas phase and are subsequently deposited onto the substrate.

The morphologies of films deposited at intermediate pressures or concentrations reflect the presence of both growth modes, i.e. growth by particle deposition and layer growth on the substrate, displaying a more fine-particulate deposit with a higher fraction of particles at the process temperature [85, 93].

Additional impurity phases were observed for both series of experiments. Li_2SiO_3 was identified and its presence can be explained by the high reactivity of excess lithium with silicon at the oxidizing atmosphere and high temperature (850°C) present in the process. Li_2SiO_3 is observed to greater extent for films that are thinner or less dense, indicating that this impurity is formed at the surface of the silicon layer and not present in the bulk. On the other hand in some cases an additional phase is observed which could possibly be related to a lithium containing manganese silicate Li_2MnSiO_4 [177].

The composition of the films have been measured with EDX corresponding to the amount of each metal relative to the total amount of transition metals present in the film. The analysis of the composition shows some variation in dependence on deposition condition with most films being in their decomposition ratio close to the 1/3 : 1/3 : 1/3 ratio, as expected for the ratio of the transition metal concentration in the precursor solution (± 5%). Only at very low solution concentrations and very low film thickness stronger deviations have been observed, which may also be attributed to a systematic error of applying EDX on very thin films [178]. This deviation is likely due to either complex deposition parameters and involved processes, extent of stoichiometry transfer to the type of deposition mode, or even the application of the analytical method. Nevertheless, a good stoichiometry is expected given the stability of the metal cations in $LiNi_{1/3}Mn_{1/3}Co_{1/3}O_2$ [179] under the deposition conditions employed.

So far, $Li(NiMnCo)O_2$ thin films prepared on a Si substrate via aerosol assisted chemical vapor deposition were studied as a model system which easily allows the monitoring of morphology and crystallinity as a function of process pressure and solution concentration. For practical use, a material like platinum (Pt), serving as current collector in battery devices, is of more relevance for further comparison with $LiCoO_2$ thin films prepared in the prior section.

The electrochemical activity of $Li(NiMnCo)O_2$ thin film on Pt was studied for a sample deposited at 850°C, 900 mbar with a solution concentration of 0.05 $moll^{-1}$, and yielded the desired microcrystalline morphology, as observed in a different study.

Figure 4.12 shows the Rietveld plot of $Li(NiMnCo)O_2$ thin film deposited on platinum foil. The film presents phase pure $Li(NiMnCo)O_2$ with composition $Li_{1.2}(Ni_{0.33}Mn_{0.34}Co_{0.33})O_{2.8}$ determined by XPS from a sample that was in contact with air which can be the reason for the oxygen over-stoichiometry. Rietveld refinement for this layer gave a texturing parameter $G_1 = 0.77$, lattice parameters a = 2.8655 Å, c = 14.232 Å and cell volume V = 101.20Å^3, which agree well with reports of $Li(NiMnCo)O_2$ [81, 172–174]. In contrast to the deposition on Si, the use of platinum facilitates the preparation of purer films due to a decreased reactivity with Li_2O/Li_2CO_3 under the conditions used.

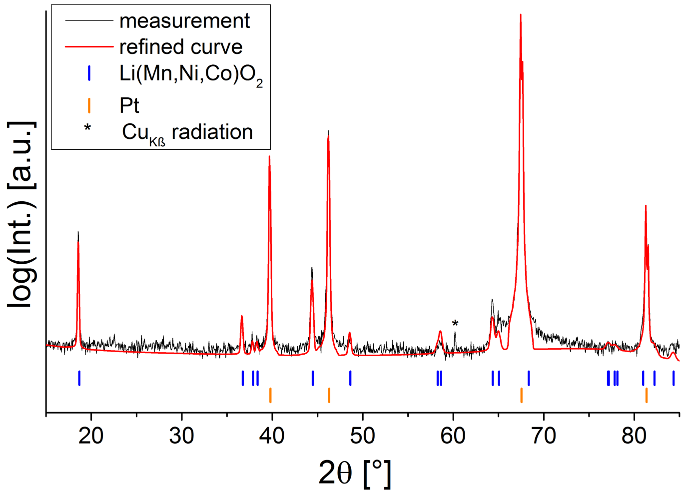

Figure 4.12: Rietvield plot of deposited $Li(NiMnCo)O_2$ layer on Pt substrate at 850°C, 900 mbar with a solution concentration of 0.05 $moll^{-1}$.

Figure 4.13 presents the SEM images of layers prepared on Pt and Si using the same deposition parameters. These films were prepared only for morphology comparison. The film deposited on platinum shows significantly different morphology compared to films deposited on silicon. A possible reason is the high reactivity of the film with the silicon substrate at the process temperature, resulting in the formation of Li_2SiO_3 which would change the nucleation and growth behavior and thus affect the overall final composition of the films.

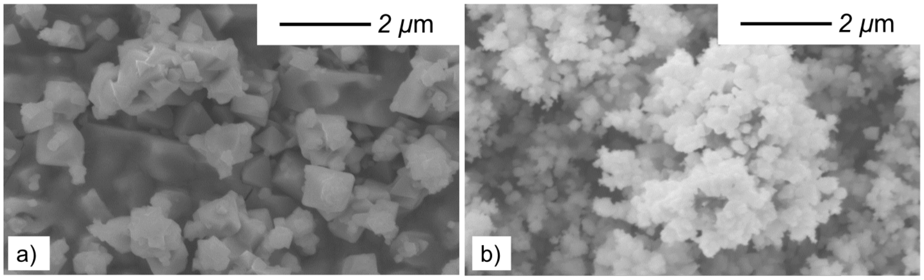

Figure 4.13: Comparison of films grown on different substrates prepared with 0.05 $moll^{-1}$ precursor solution concentration at 900 mbar, a) Pt and b) Si.

4.2.2.3 Electrochemical performance

Figure 4.14 shows the cyclic voltammetry of the synthesized material on Pt foil at 850°C, 900 mbar with a solution concentration of 0.05 moll^{-1}exhibiting good intercalation/de-intercalation behavior. The oxidation and reduction peaks on the first cycle appear at 3.85 and 3.75 V respectively. The first anodic peak presents a slight shift towards lower voltages and intensities while for the cathodic peak no change is observed. Upon film cycling the performance and capacity decreases indicated by the lowering of the peak amplitude. This behavior is similar to Li(NiMnCo)O_2 films prepared by PVD [81] and PLD [69, 180]. The slight decrease between anodic and cathodic peaks observed after the second cycle indicates a good structural stability during the lithium intercalation and de-intercalation processes [181]. This has been referred to by Jacob et al. [69] as a stabilization of the cathode surface after the first cycles with decreased polarization, reduced side reactions and better reversibility of the electrode.

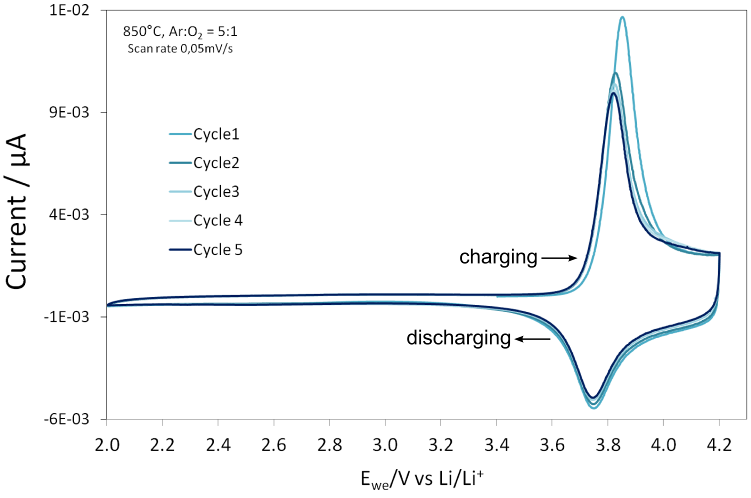

Figure 4.14: Cyclic voltammetry of Li(NiMnCo)O_2 thin film prepared on Pt at 850°C, 900 mbar with a starting solution of 0.05 moll^{-1} concentration.

The initial electrochemical analysis indicate that the Li(NiMnCo)O_2 cathode films prepared by the nebulized assisted CVD process provides promising properties as to be used in Li-ion batteries.

4.3 Conclusions

Sputtering parameters for the $LiCoO_2$ deposition had a marked effect on the chemical composition and electrochemical behavior of the material. Results exemplified that the best deposition parameters based on composition and electrochemical activity were 50 W, 550°C and 1:1 Ar:O_2.

A series of thin films of varying stoichiometry $LiNi_xMn_yCo_{1-x-y}O_2$ were deposited using a novel aerosol assisted CVD process applying an ultrasonic nebulized procedure. The effect of the working pressure and precursor solution concentration on the crystal structure texture and morphology of the films deposited on silicon wafers has been studied.

Low pressures and concentrations lead to dense films while high working pressures and precursor solution concentrations lead to more particulate and less dense films. For proper conditions, the deposition of $LiNi_{1/3}Mn_{1/3}Co_{1/3}O_2$ thin films on platinum, delivered polycrystalline films and has proven to be well suited for battery applications with good cyclability and stability.

Chapter 5

Degradation study on a $LiCoO_2$ model electrode

Electrode/electrolyte interface studies have been carried out for some time. Given that knowledge about the interface creates the basis for the modeling of surface chemistry occurring at the electrodes. Nevertheless these processes are complex to characterize and understand. The final components left on the surface from electrolyte decomposition are highly sensitive to ambient environment which makes it technically challenging for these studies to be carried out. XPS is a powerful tool that can reveal information about the surface chemistry on electrode materials. This chapter looks into the change $LiCoO_2$ thin film experiences starting from the study of the materials' surface when it is in contact with the electrolyte and after cycling in terms of chemical and structural properties.

In this part the active material was deposited in the sputtering chamber and further transfered for electrochemical measurements, always under inert environment. At this point questions concerning the nature of the resulting surface layer after battery cycling arise. Considering that the sample does not see air the only changes occurring at the surface will involve the electrolyte and the electrochemical cycling.

5.1 Thin film deposition and battery cycling

$LiCoO_2$ thin films were deposited on titanium foil (Ti) for 2 h with the RF sputtering process, 50 W, 550°C and 1:1 O_2:Ar. The active thin film material was washed with DEC solvent or immersed in the electrolyte solution for 1 h, $LiPF_6$ in a 1:1 weight ratio of ethyl carbonate (EC) and diethyl carbonate (DEC), and later washed with DEC. These samples were transported in a chamber which can be connected to a glove box and to the XPS analysis chamber to avoid having the sample in contact with air.

A further XPS analysis was carried out with a cycled $LiCoO_2$ layer. Once the battery was assembled, i.e. the cathode was set in contact with the electrolyte, separator and anode in the Swagelok cell, it was left to stabilize for 1 h before the measurement started. After cycling, the battery was opened in the glove box, where it was washed with DEC solvent. The sample was later transfered to the XPS analysis chamber in an argon filled transport chamber. The surface layer was later determined after each electrolyte/solvent exposure or cycling process.

The films deposited for battery testing were sputtered on Ti foil and were additionally analyzed with XRD and SEM before and after electrochemical activity. To obtain in depth morphological characteristics of the sputtered electrodes SEM images were also taken on films deposited on Si wafer. Electrochemical activity in a Swagelok cell configuration with $LiCoO_2$ film on Ti as cathode, Li metal as anode and the $LiPF_6$ (1:1 EC:DEC) electrolyte, was measured by a cyclic voltammetry (CV) and Galvanostatic cycling with potential limitation (GC). CV was performed for six cycles between 3-4.2 V at a scan rate of 0.05 mV/s. GC was measured applying 1 μA between 3 V and 4.2 V. Electrochemical impedance measurements were performed on the assembled battery before and after the charge/discharge experiments. EIS measurements were done with a 10 mV AC excitation signal between $5{\cdot}10^6$-0.1 Hz.

5.2 Results

5.2.1 Electrochemical characterization

Figure 5.1 presents cyclic voltammetry results for $LiCoO_2$ 200 nm thin film. The electrochemical behavior has been discussed in detail previously in Chapter 4. Both oxidation and reduction processes occurring during cycling are observed, with peaks appearing at around 3.9 V and 3.8 V respectively, in accordance with values reported in literature for thin film $LiCoO_2$. The layers present good cycling behavior and the material seems not to suffer major changes in the structure. There is low hysteresis in the reduction and oxidation peaks. Nevertheless, while the oxidation peak has only minor decrease in current, the change in reduction peak is more evident.

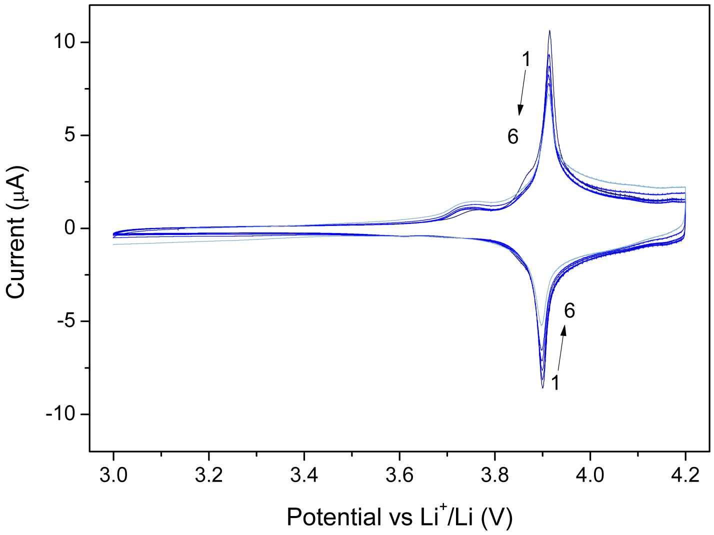

Figure 5.1: Cyclic voltamogram of sputtered $LiCoO_2$ thin film on titanium foil from 3-4.2 V.

Figure 5.2 shows the charge and discharge capacity profiles of a $LiCoO_2$ thin film after 22 cycles. A steep decrease is observed for the charge capacity after the first cycle. Succeeding charge/discharge reveals a moderate reduction for both peaks and later stabilization after the 10th cycle.

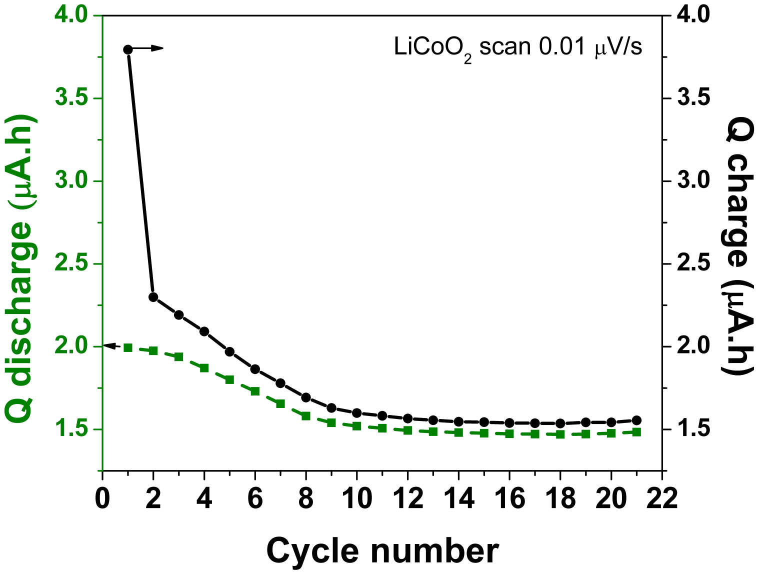

Figure 5.2: Galvanostatic cycling with potential limitation of sputtered $LiCoO_2$ films for over 22 cycles.

The Nyquist plot of the impedance measurements is shown in Figure 5.3. The analysis of the complex impedance spectra before and after cyclic voltammetry was done and the fits are also shown in the figure.

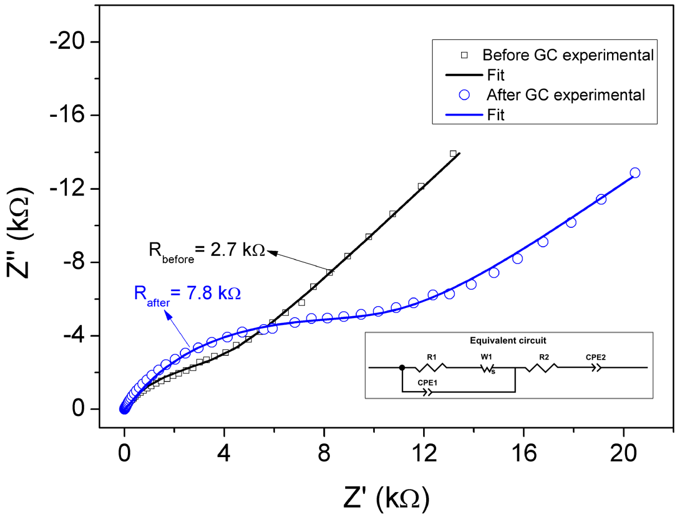

Figure 5.3: Evolution of the impedance spectra of a Li/$LiPF_6$ (EC:DEC)/sputtered $LiCoO_2$ thin film before and after 6 cycles of cyclic voltammetry measured in a Swagelok configuration.

The fits were done using a simple equivalent circuit, from which the resistances R obtained for before and after battery cycling are 2.7 and 7.8 kΩ, respectively. These results indicate how the initial resistance observed significantly increases after electrochemical cycling.

5.2.2 Structural properties after cycling

Figure 5.4 presents the SEM images for top and cross section views of bare $LiCoO_2$ layers prepared on silicon wafer. The presence of a dense film composed of uniform micro-crystallites relates to typical $LiCoO_2$ results found of similarly prepared and reported samples [166, 168].

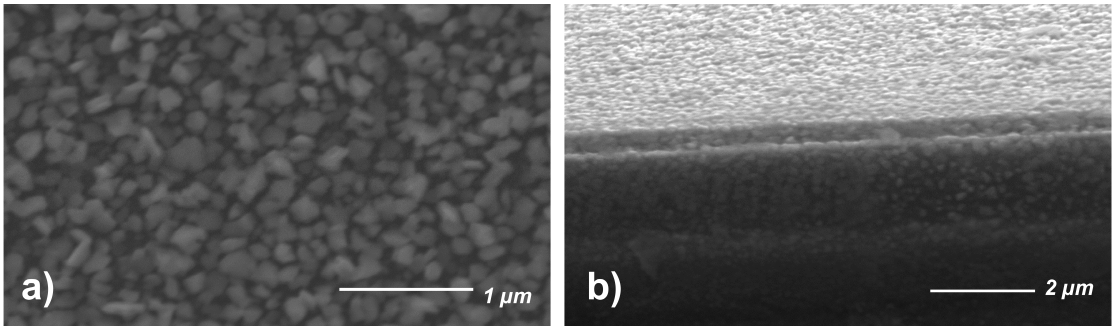

Figure 5.4: SEM images, (a) top and (b) cross section view of $LiCoO_2$ thin film sputtered on silicon wafer.

SEM images presented in Figure 5.5.(a) shows a film deposited on titanium foil, which is the substrate used for electrochemical testing. In this case the macroscopic features observed resemble these of the substrate and are different from the layers deposited on silicon. Voids and cracks related to the titanium foil are observed. The average primary particle size is between 10-20 nm. The SEM image seen in Figure 5.5.(b) corresponds to the cycled $LiCoO_2$ showing how the average particle size does not vary. From these pictures no evidence of changes related to stress, loss of material or cracks due to cycling is observed.

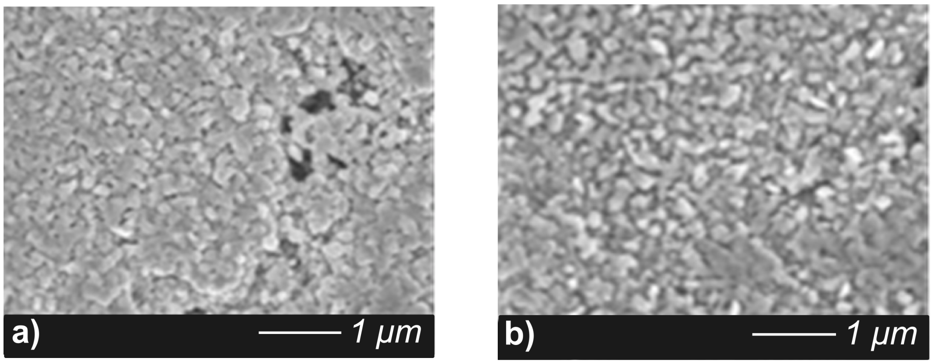

Figure 5.5: SEM images of (a) as deposited and (b) cycled $LiCoO_2$ thin film sputtered on titanium foil.

The XRD pattern measured after electrochemistry and in fully discharged state was performed to have an overview of the re-intercalated material compared to the initial layered oxide. XRD patterns of $LiCoO_2$ films before and after cycling are shown in Figure 5.6. For both cases layers present reflections from (0 0 3) around 18.8° (1 0 1) and (0 1 2) planes observed between 37°-39°.

The intensity of the (0 0 3), (0 0 6) and (0 1 2) peaks increase while (1 0 1) and (1 0 4) decrease upon battery charge/discharge cycling. Moreover, after electrochemistry, the diffraction pattern shows broadening of the $LiCoO_2$ peaks and the appearance of peaks at 19.1°, 31.3°, 36.9° and 44.9° corresponding to Co_3O_4 [182].

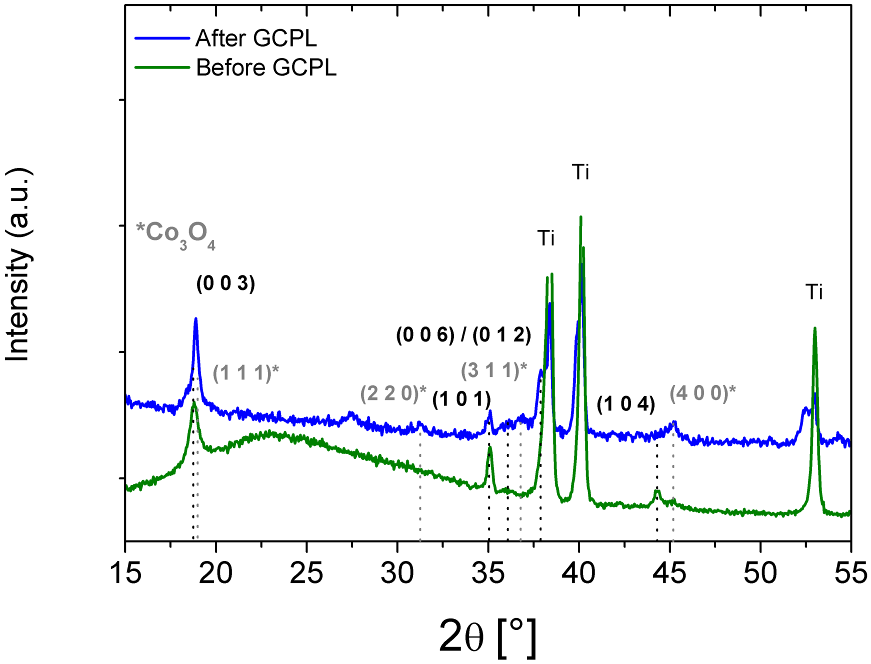

Figure 5.6: XRD pattern of $LiCoO_2$ before and after galvanostatic cycling.

Xia et al [75] showed how the roughness of the substrate influenced the final morphology of the deposited $LiCoO_2$ thin film. They compared samples presenting coarse and rough morphology and associated these features to a lack of crystallinity. The CV measurements done with these films presented broad features with anodic and cathodic peaks separation. Iriyama et al also confirmed this and observed bigger separation of the CV peaks when compared to mainly (0 0 3) oriented grains [183].

The main point is that the electrochemical properties of the layers are seen to be strongly affected by the micro structure and the surface morphology of the films. This is because the lithium ions diffusion occurs through the grains and grain boundaries of the material.

Now, when a layer is randomly oriented it will present more channels, and because of this, more surface area. In this way, when a film presents a preferred orientation the ion transport will be through the grain boundaries.

Bates et al have explained how the ion transport is less favored for a (0 0 3) preferred orientation compared to the parallel (1 0 0) or (1 0 4) texture. They also found a loss of capacity following the first cycle due to the loss in Li sites available which is due to a strain induced cell resistance increase. Kim et al have later mentioned how the fact of having a (0 0 3) preferred orientation will give structural stability during charge-discharge processes and that due to this, only a very small internal resistance should be expected, contrary to a randomly oriented films [84].

The Investigations done on the changes of the crystal structure with in situ XRD experiments have shown how the well crystallized HT-phase remains after cycling until 4.2 V, which is not the case observed here [183–185].

The polycrystalline morphology seen with SEM and the apparent changes observed in the XRD measurements performed in the present investigation, indicate that initial mixed texture of sputtered $LiCoO_2$ allows a good voltammetry cycling for first cycles due to the favored lithium diffusion. However with extended charge/discharge cycles the benefits from the mixed texture are exceeded by the effect of the lowering of crystallinity due to repeated intercalation and loss of active material (formation of Co_3O_4) resulting in a capacity loss, as observed in the GC Figure 5.2 [62, 183–185].

5.2.3 Surface chemistry analysis for $LiCoO_2$ thin films

The XPS experiments developed to characterize the surface chemistry of the cathode material after galvanostatic cycling are shown here. After electrochemical testing, batteries were carefully disassembled in an argon filled glove box, where the cathode was recovered and further washed with DEC. The samples were transported to the XPS chamber in a transfer box to avoid contamination from the environment on the surface.

As deposited $LiCoO_2$
Figure 5.7 presents the Li 1s, Co 2p and O 1s core peaks for sputtered $LiCoO_2$ thin films prior to electrochemical cycling. The Co 2p spectra shows main emissions at 779.6 eV ($2p_{3/2}$) and 794.6 eV with a corresponding satellite separation of 9.8 eV ($2p_{1/2}$). The oxygen O 1s has a strong peak at 529.3 eV, while the Li 1s region has a main emission at 54.1 eV. These spectra show the well defined photoelectron emission lines corresponding to stoichiometric $LiCoO_2$ compared to literature reports [7, 14, 164, 186].

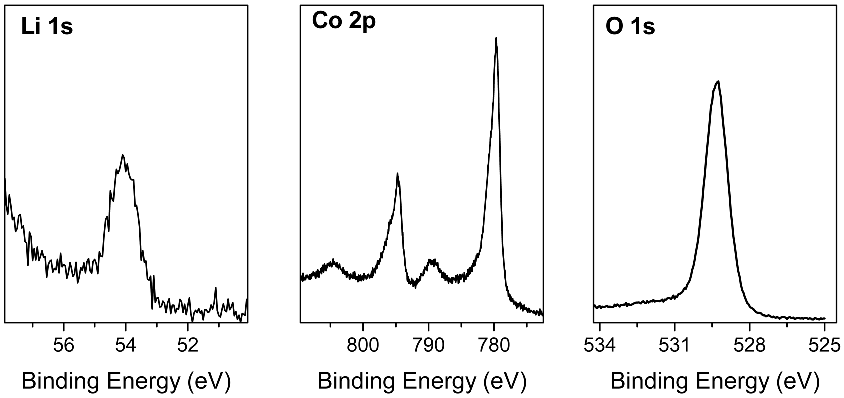

Figure 5.7: Li 1s, Co 2p and O 1s XPS spectra of a sputtered $LiCoO_2$ thin film as deposited

5.2.3.1 Effect of the electrolyte set on the cathode surface

It is a known fact that the surface layer formed on the cathode material has a marked effect on the battery performance [11, 20, 141].

Deposited $LiCoO_2$ thin films were either washed in solvent (DEC) or soaked in the electrolyte mixture ($LiPF_6$ 1 M, EC:DEC 1:1) (with further washing with DEC as done for the previous sample). The results of the XPS measurements are shown in Figure 5.8.

The photoemission of Li 1s, Co 2p and O 1s spectra from both samples, soaked-washed and washed, are similar. The emissions from lattice Li, O and Co seem to remain unaffected for the washed sample. The Li 1s region in this case shows the peak at 54.3 eV from $LiCoO_2$ with a small shoulder at 56.2 eV related to a small and unavoidable fluorine contamination in the glove box.

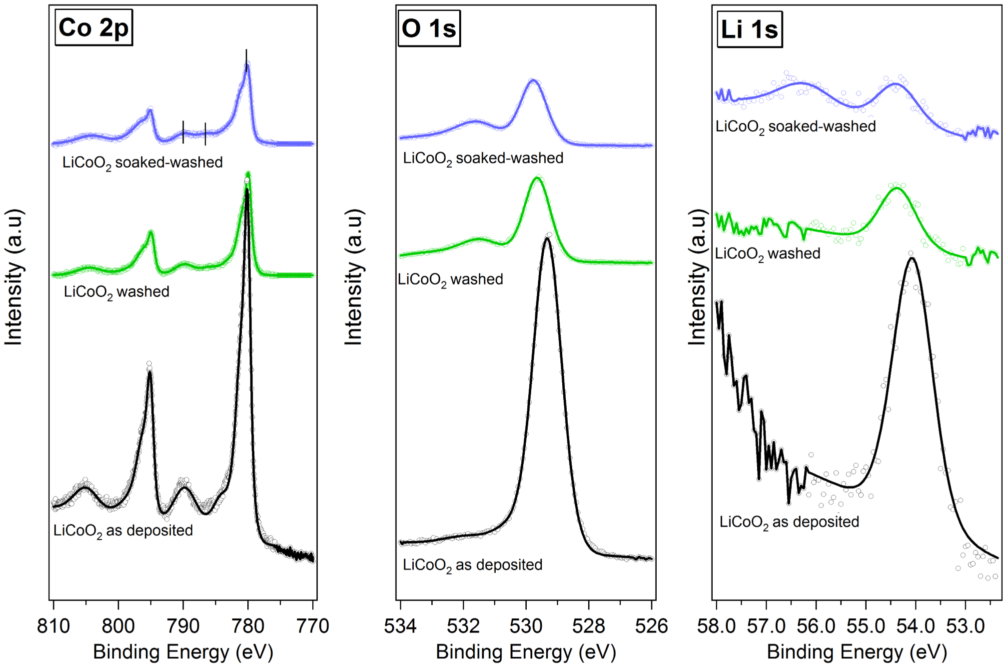

Figure 5.8: XPS spectra for the Li 1s, Co 2p and O1s core levels of $LiCoO_2$ thin film sputtered on titanium foil after $LiPF_6$ (EC:DEC) electrolyte soaking and/or washing with DEC.

The Co 2p spectra for these two samples present the same features as the as deposited layer, with emissions at 779 eV and 795 eV with satellite separation of 9.9 eV. But for the soaked sample a small increase in satellite emission ($\Delta E_B = 6$ eV) is observed, which can be associated to the formation of Co^{2+}.

On the other hand, the oxygen peak shows some variation. Compared to the initial material the main component coming from the lattice oxygen, detected at 529.6 eV, has now a shoulder at higher binding energies, 531.4 eV, which can be assigned to carbonates CO_3^{2-} and new oxygenated species at the surface. Nevertheless, a more important presence of oxygenated species at the surface of soaked-washed samples is seen compared to the washed. The main differences between these two samples comes from the inorganic species from the salt and the Co peak showing a difference in the shoulder shape.

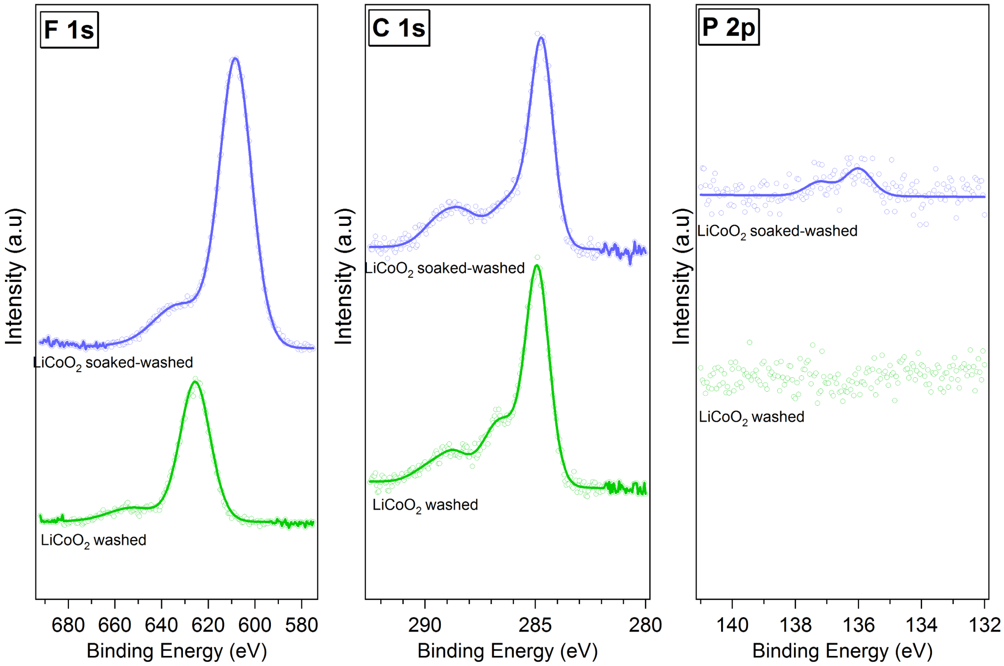

Figure 5.9: XPS spectra for the F 1s, C 1s and P 2p core levels of $LiCoO_2$ thin film sputtered on titanium foil after $LiPF_6$(EC:DEC) electrolyte soaking and/or washing with DEC.

The C 1s, P 2p and F 1s XPS spectra are presented in Figure 5.9. The C 1s line exhibits peaks at 285.0 eV, 286.5 eV and 288.9 eV from aliphatic, CO and COO compounds.

The presence of the small fluorine contamination on the surface of the sample may be caused by the formation of LiF derivatives. Nevertheless, the soaked-washed surface exhibits an important presence of several fluorinated components. The F 1s peaks observed at 685.3 and 688.0 eV can be assigned to LiF and other Li_xPF_y components respectively. This is correlated with the P 2p spectrum of the soaked-washed samples and not seen in the washed sample. Altogether this is a proof that there are species arising from the degradation of the $LiPF_6$ salt on the soaked-washed sample that are not present on the only washed sample.

The spectra of the sample that was soaked in the electrolyte shows key differences in the $LiCoO_2$ layer when compared to the washed sample. On one side the Li peak presents an extended profile related to the appearance of LiF, while the lithium from the $LiCoO_2$

lattice decreases. The O 1s shows a broader component at higher binding energies when compared to the washed sample. The peak features evidence an important presence of oxygenated compounds.

5.2.3.2 Surface analysis of cycled electrodes

In Figure 5.10 the XPS data of a cycled $LiCoO_2$ sample are shown. According to the XPS analysis, the surface recovered layer is composed of Li, Co, O, C, F and P elements. Figure 5.10 presents Co 2p, O 1s, Li 1s, C 1s, F 1s and P 2p spectra of the recovered $LiCoO_2$ layer from the battery which appear very different from the ones observed for the pristine electrode (Figure 5.7). A summary of the peak assignment is done in Table 5.1, based on experimental data obtained in this work and findings reported in literature [8, 140, 141].

After cycling, the Li 1s spectrum presents two new components. The supplementary components with higher binding energies compared to the lattice lithium from the electrode is related to the presence of fluorinated lithium compounds, LiF and $LiPF_6$, at 56.0 and 56.6 eV respectively.

The Co 2p is quite weak and is only observed in a low extent on the surface given the high signal to noise ratio. The shape of the emission shows a slight change in the shapes of satellite peaks in reference to the main peak when compared to the starting material. Nevertheless the rough estimate still indicates that cobalt is mostly present with oxidation state 3+. A modified intensity in the satellite features indicate in addition an increased contribution of Co^{2+}.

The O 1s signal presents two peaks at 529.4 eV and 532.7 eV corresponding to the lattice oxygen and other carbon-oxygen containing species ${CO_3}^{2-}$ at higher, and COO and CO at lower binding energies.

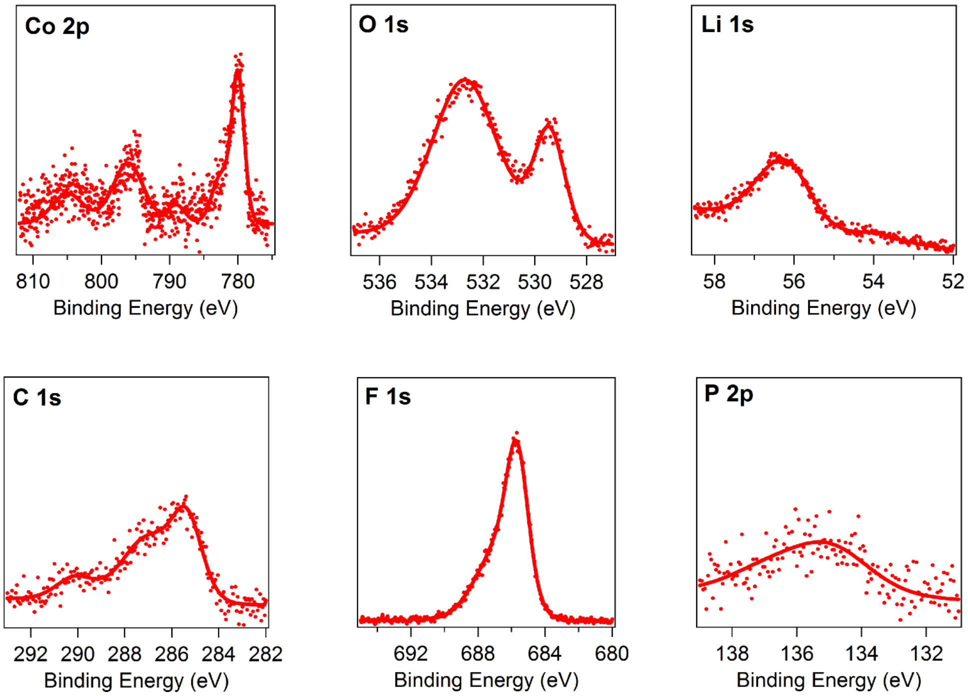

Figure 5.10: Li 1s, Co 2p and O 1s spectra of the recovered $LiCoO_2$ surface after electrochemistry

The C 1s peak shows the existence of multiple components. The spectra is composed by a component at 285.2 eV attributed to the presence of aliphatic carbon chains. Components at 287.0 eV and 288.7 eV are attributed to polymeric units containing C-O bonds. The last component at 290 eV reveals the presences of carbonate species.

The P 2p signal is quite low, however, it has an extended profile around 135 eV which may indicate the presence of intermediate fluorophosphate species from the degradation of the electrolyte's salt. On the other hand the strong F 1s peak shows the presence of two components at 685.6 and 686.8 eV. These peaks are assigned to LiF and $LiPF_6$/ fluorophosphate intermediates, in correspondence to literature reports and to the Li 1s spectrum found before galvanostatic cycling.

Some reports show how cycling was found to help the surface chemistry to develop [14,20,97]. Reactions observed include oxidation of solvent (EC) or ring opening polymerization which is catalyzed by a nucleophilic mechanism that occurs spontaneously involving electron transfer without the need of cell charging. These spontaneous processes were studied by Wang et al. with gas chromatography and mass spectroscopy, and showed how even without electrolyte salt, $LiCoO_2$ has strong reactions with mixture of EC/DMC [190]. Additionally, salts which are part of the electrolyte are also found to participate in the surface layer formation [97].

The presence of species containing C, F and P elements on the surface shows how the

Table 5.1: Chemical composition of $LiCoO_2$ cathode after battery cycling. [4, 5, 7, 9, 97, 140, 141, 187–189]

Peak	BE (eV)	Assignment
Co 2p	779.7	$LiCoO_2$
	786.8	sat II+
	789.8	sat III+
F 1s	685.5	LiF
	686	$LiPF_6$
	687.7-688.4	Fluorinated alkanes
O 1s	529.3-530	$LiCoO_2$
	531-532,7	Oxygenated compounds
	533-534	Polycarbonate
C 1s	285	Aliphatic
	286-288	CO/ COO
	289-290	CO_4^{3-}
P 2p	133.5-133.9	LiPON /PO_4^{3-}
	134.9	PO_4F_y
	136.7	$LiPF_6$
Li 1s	53.8	$LiCoO_2$
	56.0	LiF
	56.7	$LiPF_6$, $Li_xP_yOF_z$

decomposed and intermediate species from the electrolyte are present on the cathode surface and remained after the films were washed with DEC electrolyte. Therefore, it is possible to establish that the signal from the initial cathode material is quite low and evidences the formation of a cover layer mainly based on inorganic compounds from the salt and some organic coming from the solvent.

The formation of LiF has been associated to two main reasons. One is the instability of the $LiPF_6$ salt which decomposes and forms LiF and PF_5, while the second is the hydrolysis of $LiPF_6$ generating HF (Reaction 5.1-5.3) and further reaction with the transition metal oxide. Reactions 5.2 and 5.3 show the proposed mechanisms of LiF formation by salt decomposition and reaction with cathode.

$$\mathrm{H_2O + LiPF_6 \longrightarrow HF + LiF + POF_3 + 2\,HF} \tag{5.1}$$

$$\mathrm{LiPF_6 \longrightarrow LiF + PF_5} \tag{5.2}$$

$$\mathrm{LiCoO_2 + 2\,xHF \longrightarrow 2\,xLiF + Li_{1-2x}CoO_{2-x}} \tag{5.3}$$

As Andersson et al suggested, for similar transition metal oxides, Reaction 5.3 will produce

LiF as part as the surface layer adjacent to the active cathode material, while Reaction 5.2 will produce LiF randomly [187,188]. These findings, and their correlation with an increase in cell impedance (Figure 5.3), can be attributed as well for the case presented here, since LiF layer on the cathode material is highly resistive to lithium ion migration [11,141].

Some groups attribute the reactions occurring coming from an electrophilic attack from the Lewis acid PF_5 which reacts with carbonates and leads to polymerization [97,187]. Andersson et al have also proposed possible reactions occurring at the surface as an electrophilic attack from the lewis acid mainly due to the instability of $LiPF_6$ salt and that will further react with cyclic carbonate (EC) and favors polymerization [187]. Liu et al. have reported the presence of $ROCO_2Li$, ROLi and Co_3O_4 as products on the spontaneous reaction of nano-sized $LiCoO_2$ and DMC. They conclude how, for the case of DMC, the reduction of solvents enhance the production of the surface layer [189].

The Co 2p spectrum on soaked-washed sample has overall the same features as the washed sample and initial $LiCoO_2$ sample. It presents a broader emission around 789 eV with two satellite peaks with difference of 6 eV and 10 eV. The appearance of the satellite at 786 eV and the broadening of the main emissions indicate the presence of Co^{2+} in the surface [7,164]. Reports state that oxygen deficient lattices induces the formation of Co^{2+}, which has a smaller difference in binding energy than Co^{3+} [164]. Yamamoto et al carried out X-ray Absorption Spectroscopy experiments on immersed $LiCoO_2$ in $LiClO_4$ (1:1, EC:DEC) electrolyte [40]. They found that the surface undergoes reduction and further non-reversible changes in the electronic structure upon electrolyte immersion. This surface instability is due to the increased concentration of transition metal anti-site coupled to the formation of a reaction layer. The creation of these defects was found to depend on the concentration and chemical potential of both Li and Co, which involve the actual amount of Li and Co participating in the reaction that forms $LiCoO_2$ [191]. Hoang and Johannes have found how the defect formation energies are sensitive to the Co:Li ratio and in this way explain the presence of Co^{2+} ions. For the case of the experiments shown here, the presence of fluorinated salts enhances the reactions with the active material, and specially with the oxygen present in the lattice, as reflected by the decreased amount of these species on the surface [191].

When comparing to both soaked-washed, washed and cycled samples, there are in general similarities in terms of organic and inorganic components forming the surface layer. It is evident that once the active material is set in contact with the electrolyte several simultaneous processes occur.

The first process involves oxygen from the lattice giving an oxygen deficient interface layer that will then promote the reduction of Co atoms and a creation of space charge layer. This was proposed recently by Yamamoto et al where a study with total-reflection florescence X-ray absorption spectroscopy (TRF-XAS) analyzed the electronic structure of the electrode-electrolyte interface [40].

The second process involves the reaction and deposition of lithium containing species that may consume Li from the active material. The fact that after cycling the remaining surface layer contains mainly inorganic species coming from the electrolyte that are actually deposited on the active materials indicates that cycling favors the second process even more. The creation of a surface layer with increased impedance coming from the two processes affect the overall performance of the material and decrease capacity.

The overall processes present after contact of the electrode material with the electrolyte and/or after cycling were observed with the set of XPS experiments. When the samples are soaked there are more organic species seen than after CV evidenced by the estimation of carbon containing species related to each sample, around 14% for soaked and 9% after CV. This is a clue of the influence of electrochemical reactions and transport phenomena which enhance the movement of decomposition species. When the films are soaked the reactions take place on the surface and the material is covered. The possible presence of small amounts of water in the electrolyte solution will contribute to formation of highly resistive species and oxygenated chains that are seen on the soaked and washed layer in higher proportion. In this way it is possible to say that the formation of the surface layer is enhanced by the electrolyte water contamination and the absence of current allows these species to react and deposit on the active material.

5.3 Conclusions

SEM and XRD results showed how the $LiCoO_2$ sputtered layers have initial mixed texture and additional good voltammetry cycling for first cycles due to the favored lithium diffusion. Extended charge/discharge produces lowering of crystallinity due to intercalation processes and loss of active material (formation of Co_3O_4) resulting in a capacity loss.

Washing and soaking the electrode material in the electrolyte and solvent shows that surface reactions start from the first contact. The formation of a surface layer from these processes occur with organic components from the solvent and inorganic form the salt.

$LiPF_6$ has a very important effect since it can decompose and form HF which reacts with carbonates and forms highly resistive LiF salt on the surface, which induces the increase in interface resistance observed with EIS measurements.

The remaining surface layer is mainly carbonated species and some inorganic components. The carbon compounds found correspond to reactions from the EC solvent while the $LiPF_6$ salt forms LiF and other Li_xPF_y compounds, to a lower extent.

The surface chemistry of the layer formed on $LiCoO_2$ after cycling is based mainly on decomposed species from the electrolyte deposited arising from carbonated and fluorinated species.

Soaking the sample for a short time results in the deposition of a surface layer on the active material composed of organic compounds related to the solvent. Contrary, electrochemical cycling favors the formation of inorganic species from the salt on the cathode surface. On one hand the electrolyte salt starts decomposing and may induce further reactions generating intermediate species, that with any possible water trace, that can enhance polymerization of solvent and formation of other products.

Chapter 6

Artificial surface layers for the $LiCoO_2$ cathode

As was reviewed in Chapter 2 and observed in Chapter 5, the formation of a surface layer on bare $LiCoO_2$ is occurring from the first contact of the material with the electrolyte. The composition of these films were determined for the sake of elucidating what components are present on the electrode-electrolyte interface after electrochemistry, and how this can be associated to the battery performance.

Coating of the cathode material in known for improving electrochemical behavior [27, 30, 148]. Research has proven how coatings suppress phase transition, improve structural stability, and decrease disorder of cations in crystal sites by preventing cathodes to be in direct contact with the electrolyte. Additionally, modifying the electrode was found to help suppress the relative release of oxygen that leads to instability [144, 192]. Among the studies performed on coating procedures for cathode materials several questions remain unsolved. The stability of metal oxides in non aqueous electrolytes, specially with corrosive acids like HF in $LiPF_6$ based electrolyte have, can be reduced and a further formation of surface fluorides can be expected [193]. Additionally, the preparation of uniform and robust coatings may be difficult and carry with extra process costs [193]. ZrO_2 and LiPON have successfully shown significant improvements when applied to thin film active materials [24, 27, 148]. These studies have focused on the electrochemical behavior of coated cathode material. Nevertheless new/different processes are expected to take place at the electrode-electrolyte interface when an artificial surface layer is generated by coating. Thus, this chapter focuses on the XPS analysis of the artificial surface layers created on $LiCoO_2$ by a thin sputtered ZrO_2 or LiPON layer. The results are set in relation to the electrochemical behavior of each case studied with additional morphology and structure investigations with SEM and XRD.

6.1 Experimental

LiPON and ZrO_2 thin films were prepared using rf magnetron sputtering. The chosen deposition parameters where determined after a series of screening electrochemical experiments with different coating thicknesses. Table 6.1 summarizes the deposition parameters used for ZrO_2 and LiPON films. Thin layers of ZrO_2 or LiPON were either deposited onto silicon substrate for standard material characterization, or on a 200 nm layer of standard $LiCoO_2$, which was prepared on titanium foil at 50 W, 550°C and 1:1 O_2:Ar. Both coating materials were deposited by reactive sputtering with a mix of gases (O_2:Ar) for ZrO_2 from a metallic Zr target, and pure N_2 with a crystalline Li_3PO_4 target for LiPON.

Table 6.1: Deposition parameters for the rf Sputtering of LiPON and ZrO_2 thin films. (*Temperature was not controlled in these depositions)

Material	**LiPON**	**ZrO_2**
rf Sputtering Power (W)	40	40
Pressure (mbar)	$8{\cdot}10^{-3}$	$8{\cdot}10^{-3}$
Gases	N_2	O_2:Ar
Gas Flow (sscm)	10	9.5:0.5
Temperature (°C)	*	300
Target-sample distance (cm)	5.5	4

By combining XPS quantification and profilometry measurements, the thickness of the ZrO_2 and LiPON thin film coating was approximately calculated to be 2 nm and 26 nm, respectively, with an uncertainty of 10% [153].

A series of in-situ deposition and electrochemical experiments, cyclic voltammetry (CV) and galvanostatic cycling with potential limitation (GC), were done on the coated $LiCoO_2$ layers. Swagelok cells were prepared using Li metal as anode, $LiPF_6$ in EC:DEC (1:1) as electrolyte, and the coated $LiCoO_2$ as cathodes. CV experiments were performed between 3-4.2 V at a scan rate of 0.05 mV/s and the GC experiments were done applying 0.01 µA between 3-4.2 V for both charge and discharge processes for at least 20 cycles. Subsequently, XPS measurements were performed on recovered cathode thin films, which were washed with DEC solvent and transported under inert atmosphere from glove box to the analysis chamber.

6.2 Results

6.2.1 Coating characterization

SEM and XRD were additionally employed to analyze coating layers. As a first step, thick layers (150 nm ZrO_2 and 200 nm LiPON) were deposited on silicon substrate for morphology, composition and crystallinity determination.

The SEM images of thick sputtered layers of ZrO_2 and LiPON are shown on Figures 6.1 (a) and (b) respectively. Both materials deposited on silicon substrates present formation of small grains in the layer. The grain size present in ZrO_2 appear to be smaller than the ones in the LiPON layer. Nevertheless the quality of the SEM images does not allow further evaluation.

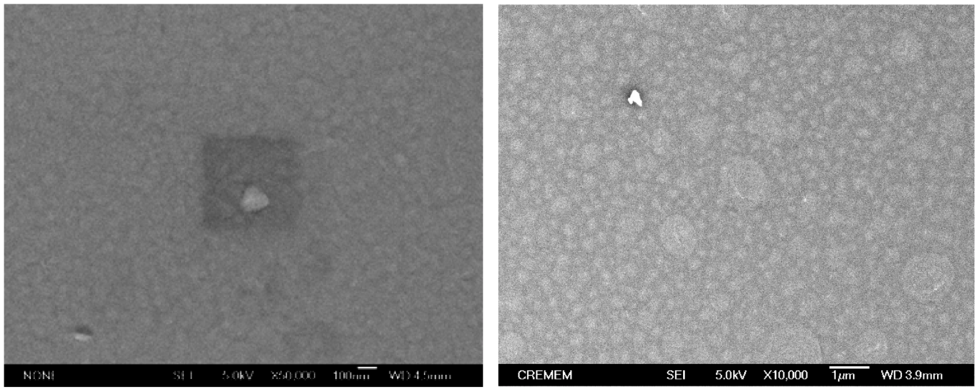

(a) (b)

Figure 6.1: SEM images of (a)ZrO_2 thin film (150 nm) and (b) LiPON (200 nm) sputtered thin films on silicon substrate.

Figures 6.2 shows the XPS spectra of Li 1s, P 2p, O 1s and N 1s core levels of sputtered thick LiPON on silicon substrate. The surface composition of the layer was $Li_{1.3}PO_{2.4}N_{0.8}$ quantified by XPS. The Li 1s appears at 57.8 eV and P 2p at 135.6 eV. N 1s and O 1s present broad peaks between 397-400 eV and 531.4-532.4 eV respectively. Details on these features are addressed in Chapter 7. The composition obtained presents less Li and more N than other sputtered LiPON thin films reported [34, 194].

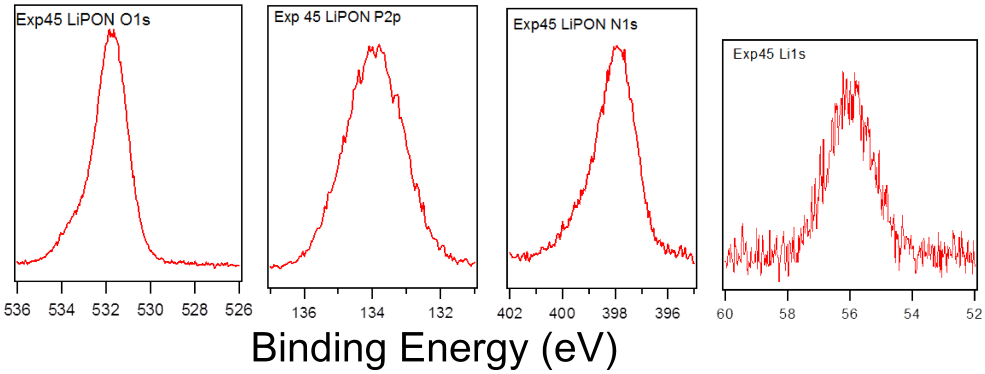

Figure 6.2: XPS of a LiPON (200nm) layer.

The XPS spectra of Zr $3d_{5/2-3/2}$ and O 1s for a thick ZrO_2 layer, deposited on silicon wafer, was also measured. Results are shown in Figure 6.3 evidencing typical features for a metal dioxide layer, with O 1s at 529 eV and Zr 3d doublet at 181.6 eV and 183.9 eV. The surface composition determined by XPS is $ZrO_{2.3}$.

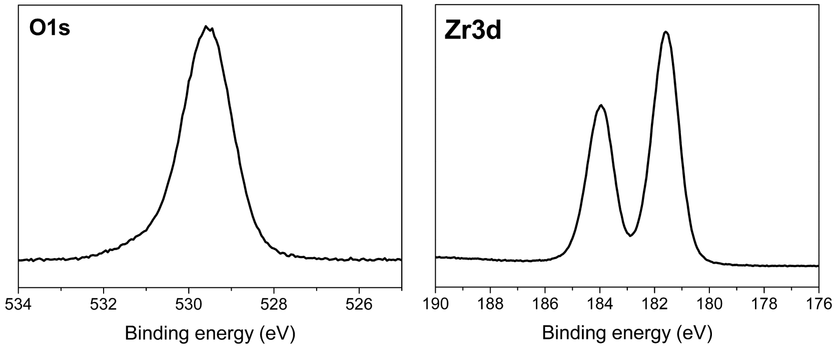

Figure 6.3: XPS of a thick ZrO_2 (150 nm) layer.

6.3 Coated $LiCoO_2$

SEM images of ZrO_2- and LiPON coated $LiCoO_2$ are shown in Figure 6.4 (a) and (b). The main effect of the thin coating on the active material is the smoothening of the sharp edges of the $LiCoO_2$ crystallites. This effect appears more pronounced in the case of ZrO_2 coating, nevertheless it appears to be an inhomogeneous coverage, possibly related to the very thin nature of layer (2 nm). LiPON on the other hand seems more homogeneously distributed over the active material as was observed for similar layers reported in literature [195].

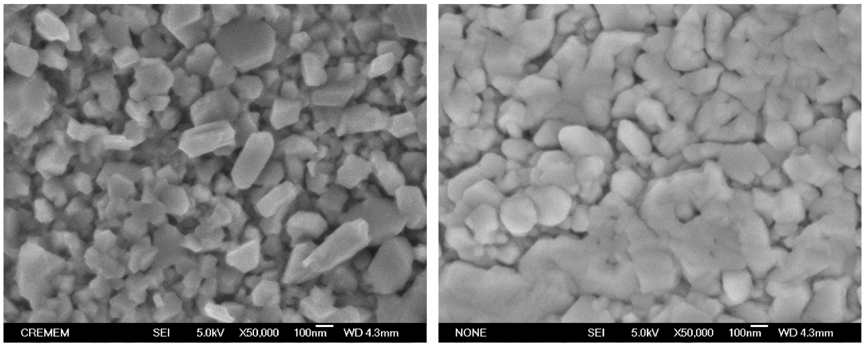

(a) (b)

Figure 6.4: SEM images of (a)ZrO_2- and (b) LiPON- covered $LiCoO_2$ thin films deposited on titanium foil.

6.3.1 Electrochemistry of coated $LiCoO_2$

Figures 6.5 (b) and (c) show the cyclic voltammetry curves for cycles 1 and 5 of LiPON-coated and ZrO_2-coated samples respectively, compared to the uncoated layer, Figure 6.5 (a). Coated LiPON layer presents broader cathodic and anodic peaks compared the uncoated layers different from what Song et al observed for the first two cycles [24] in LiPON-coated (3 nm) and uncoated $LiCoO_2$ films [24,196]. They have employed a thinner LiPON coating which shows a faster transfer kinetics than the one used here (26 nm), which could be reason for the higher current peak observed by them. On the other hand, the ZrO_2 coated layer shows similar decreased current and broadening as the ones prepared by Takamatsu et al for over 180 s deposition [28]. From the CV curves it is possible to conclude that, at least for short cycling, ZrO_2 coated cathode is slightly more stable.

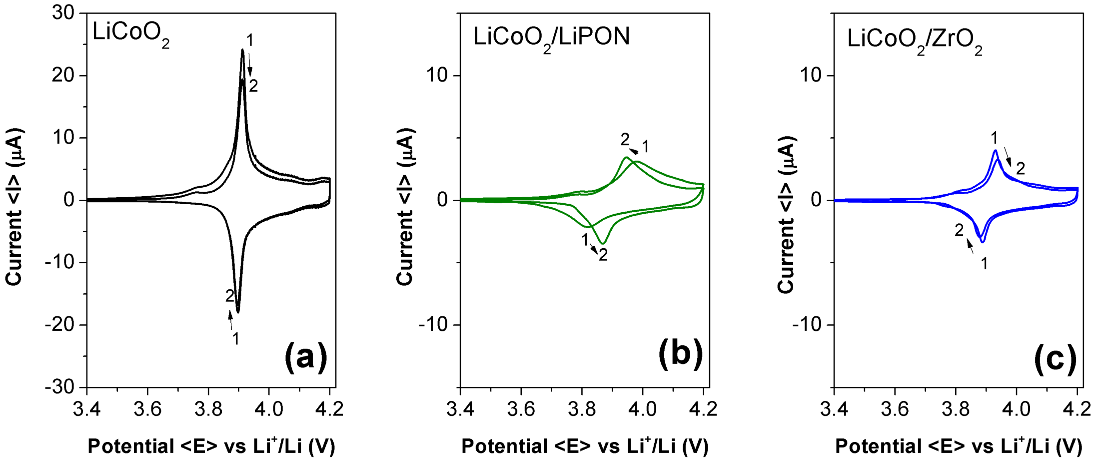

Figure 6.5: Cyclic voltammetry of cycles 1 and 5 of (a) bare $LiCoO_2$ compared to (b)LiPON-coated and (c)ZrO_2-coated layers.

Figure 6.6 compares the effect of each coating on the discharge capacity. Results show how LiPON has initially a higher discharge capacity than ZrO_2 coated sample. However, over the first 20 cycles both systems seem to stabilize towards the same discharge capacity value.

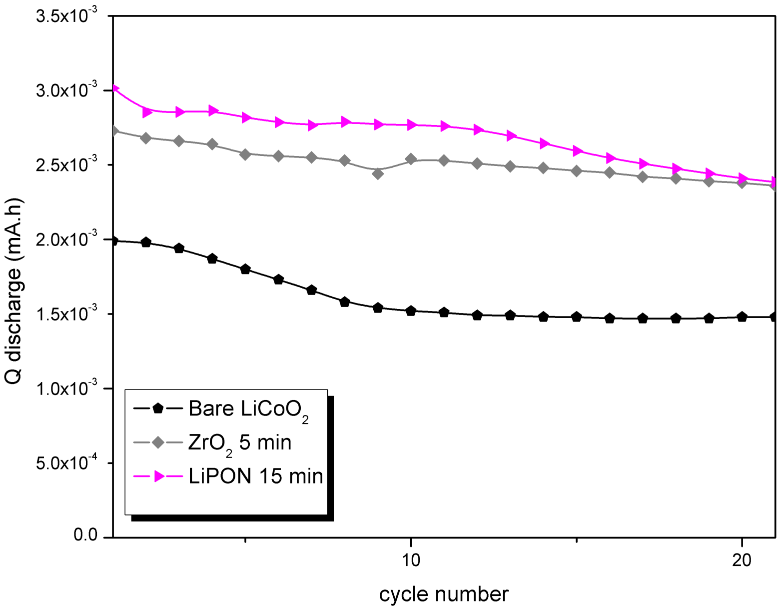

Figure 6.6: Galvanostatic cycling results for sputtered uncoated $LiCoO_2$, ZrO_2-coated 5 min (2 nm) and LiPON-coated 15 min (26 nm) deposition.

Figure 6.7 presents XRD patterns of bare and ZrO_2- and LiPON- coated $LiCoO_2$. The patterns of coated layers show no significant difference when compared to the bare $LiCoO_2$. It is possible to say that the thin layers on the cathode have no effect on the crystal structure nor formation of any detectable additional phase.

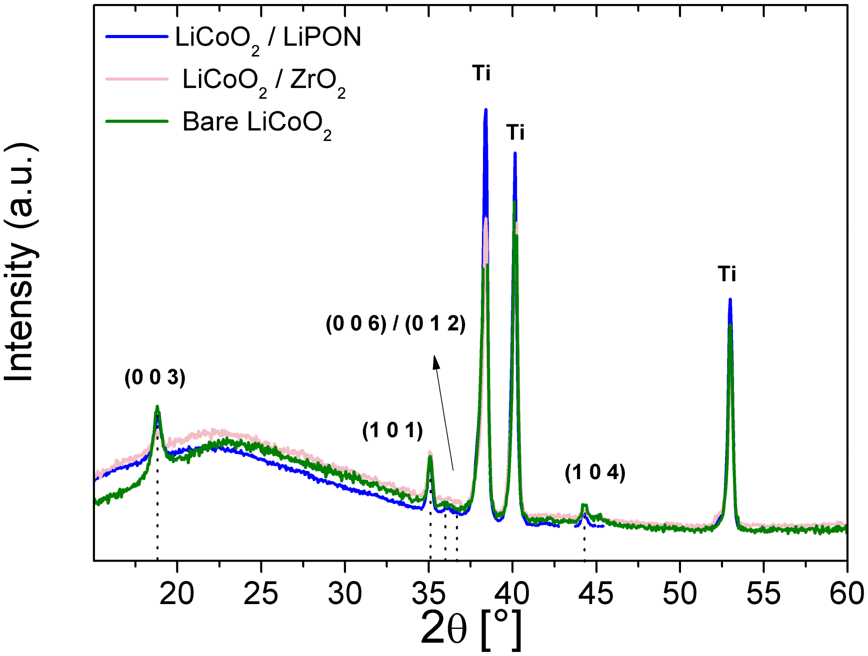

Figure 6.7: XRD of sputtered ZrO_2 coated $LiCoO_2$ layers before and after coating. *Interrupted signal observed during spectra acquisition.

6.4 XPS surface layer study of ZrO_2- and LiPON-modified cathodes.

6.4.1 Initial surface layers

As in literature the term used for Solid Electrolyte Interphase is referred to the negative electrode, in the following sections the new interface created by thin film coating deposition will be called *artificial surface layer* to avoid any confusion for the reader.

As a first step, XPS measurements were done on the coated layers to obtain reference points for binding energies and initial components present on the artificial surface layers. Figures 6.8 presents the XPS spectra obtained for the ZrO_2- and LiPON- coated $LiCoO_2$ thin films for corresponding Li 1s, Co 2p, O 1s, P 2p, N 1s and Zr 3d core levels. The stacked spectra are meant to have a comparison between coated and uncoated $LiCoO_2$.

The artificial surface layer observed for the LiPON coated layer has components with similar characteristics as the thick LiPON discussed before (Figure 6.2). The artificial layers are composed of Li 1s, O 1s, P 2p and N 1s showing particular features of a LiPON thin film with overall composition $Li_{1.3}PO_{1.9}N_{0.3}$. The newly formed surface layer presents only LiPON and no presence of $LiCoO_2$ components. Nevertheless an apparent oxygen deficiency is observed.

As the sputtered LiPON layer is thicker (approx. 26 nm) than the ZrO_2 layer (approx. 2 nm), the signals of the cathode material are not observed, which is not the case for the thin ZrO_2 coating.

The artificial surface layer from ZrO_2 coated $LiCoO_2$ is composed of Li, Co, O, and Zr. The direct relation between the Co 2p, Li 1s and O 1s indicate that effectively the layer is made of a mixture of $LiCoO_2$ and ZrO_2. Li 1s seen for the ZrO_2 coated layer can be attributed to presence of lattice lithium in the pristine material. The O 1s shows as well the main featured for $LiCoO_2$ and ZrO_2, peaks at 529 eV and a small shoulder for surface oxygen. Co 2p signal is quite low, nevertheless it is possible to see the broadening of the main emission and the appearance of a small shoulder at $\Delta E_B = 6$ eV, satellite related to Co^{2+}. On the other hand, O 1s has no main differences since both oxygen from the oxides have similar binding energy and seem to overlap to form a broader peak. It is important to note that also in this case there is oxygen deficiency on the newly formed artificial surface layer.

Summing up, the characterization of the initial surface layers showed that the thin layer of ZrO_2 give a reaction layer between the active cathode and the metal oxide. On the other hand, and given that the LiPON layer is thicker, all features present in the new surface layer corresponds to the coating.

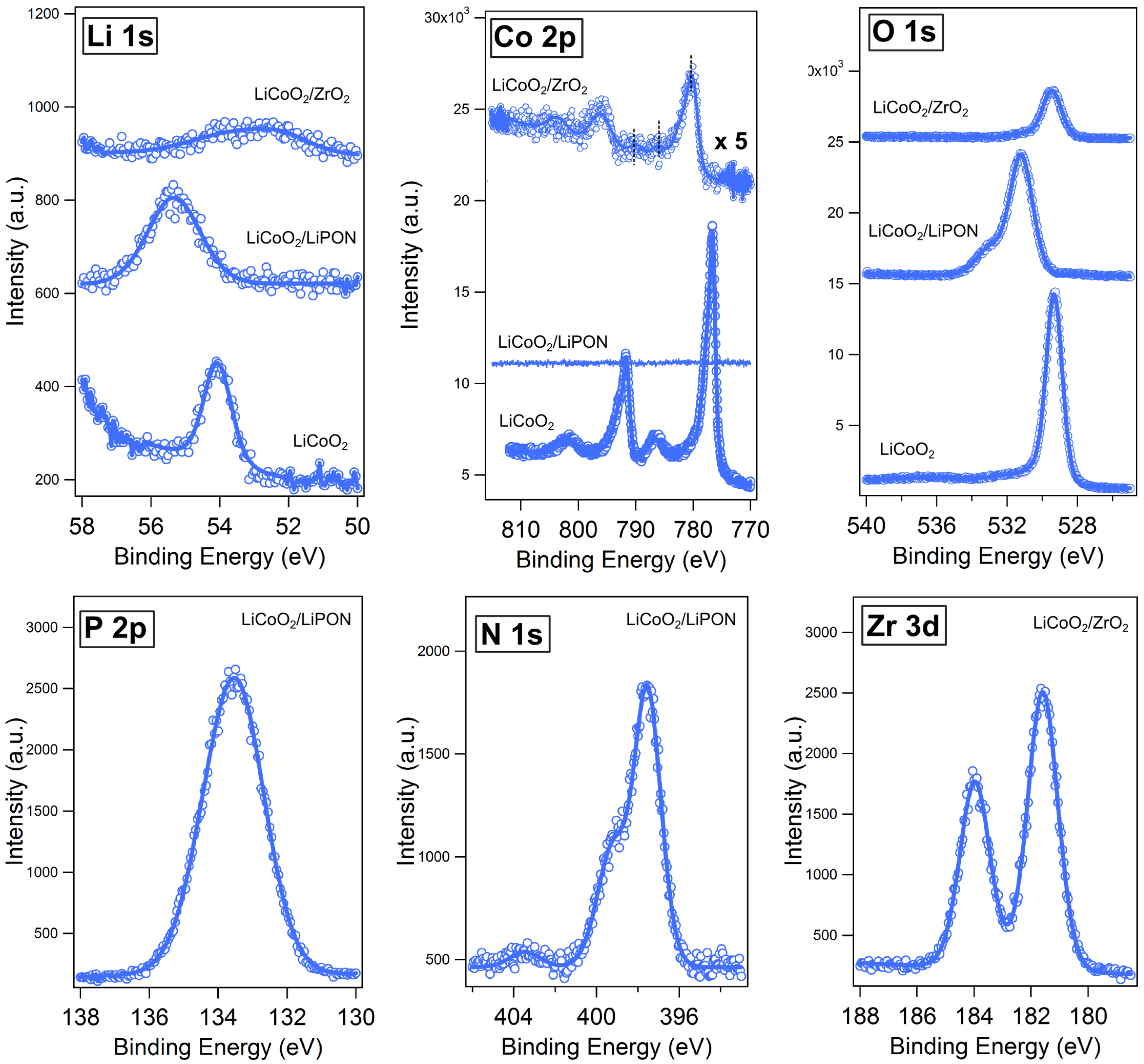

Figure 6.8: Li 1s, Co 2p, O 1s, P 2p, N 1s and Zr 3d core level spectra of initial surface layers formed after sputtering ZrO_2 or LiPON. Comparison made with uncoated $LiCoO_2$.

6.4.2 Surface layers after electrochemistry

The set of XPS experiments shown before were used to characterize the surface layers formed of coated films after galvanostatic cycling. The electrodes were recovered from the battery and washed with DEC. This procedure was executed in an argon filled glove box from where the sample was later transported to the XPS chamber in a transfer box to avoid having contaminations on the surface.

The surface chemistry of the recovered coated cathode materials after electrochemistry are based on Li, Co, O, Zr and N with additional C, F and P elements. The Li 1s, O 1s, Co 2p, C 1s, F 1s and P 2p spectra of coated and uncoated $LiCoO_2$ are shown in Figure 6.9. Zr 3d and N 1s core peaks of ZrO_2- and LiPON-coated $LiCoO_2$ thin film, before and after galvanostatic cycling are shown in Figure 6.10. The data of XPS analysis are summarized in Table 6.2.

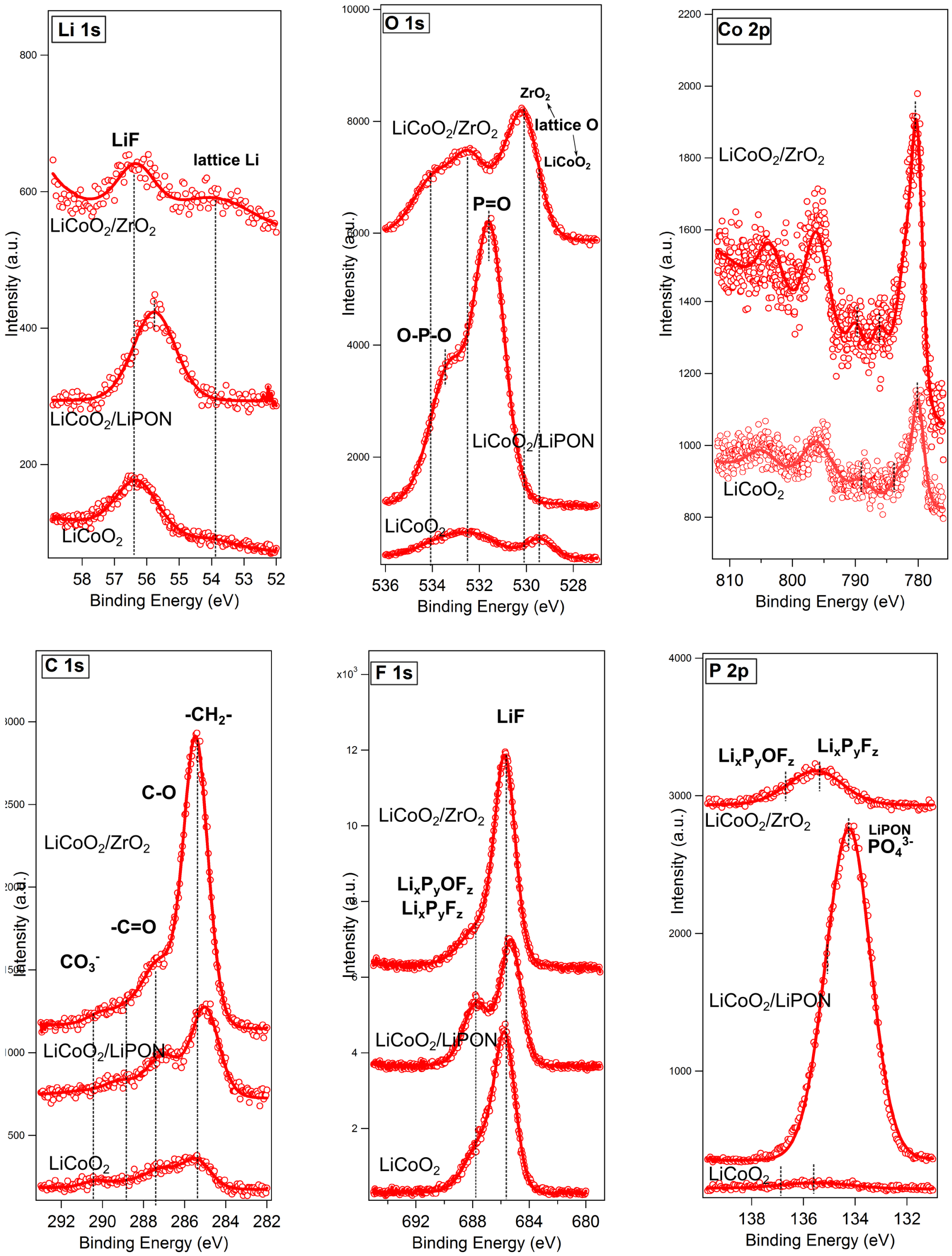

Figure 6.9: Li 1s, O 1s, Co 2p, C1s, F 1s and P 2p core peaks of uncoated, ZrO_2- and LiPON-coated $LiCoO_2$ thin films after galvanostatic cycling.

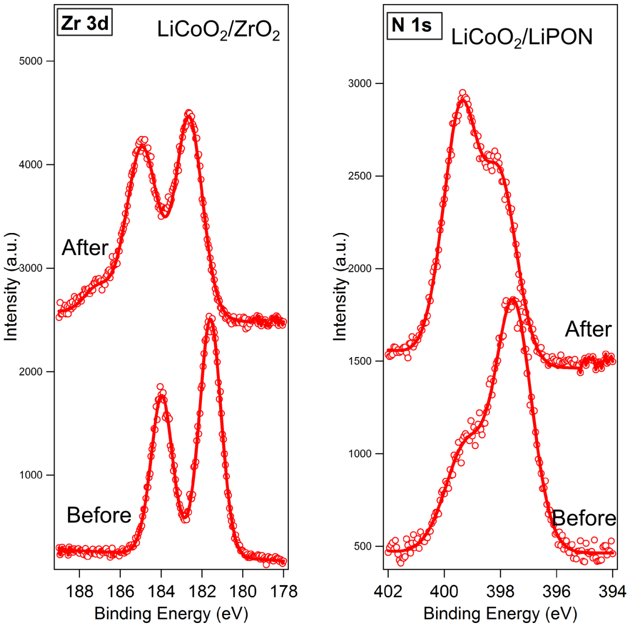

Figure 6.10: Zr 3d and N 1s core peaks of ZrO_2- and LiPON-coated $LiCoO_2$ thin film, before and after galvanostatic cycling.

6.4.2.1 ZrO_2 coating

Given the mixture of cathode and the coating layer on surface layer, the XPS spectra of ZrO_2-coated and bare $LiCoO_2$ present many similarities. As seen on Chapter 5, the Co 2p core peak for cycled $LiCoO_2$ shows the presence of a small amount of Co^{2+} ions proven by the presence of the satellite peak at 786 eV and also XRD measurements. It is possible to see this feature for the cycled ZrO_2 coated layer as well.

The O 1s core peak of the ZrO_2 coated sample displays a profile of at least three peaks. At lower binding energy, around 529 eV, the peak may be assigned to the oxygen from the crystalline network. At higher binding energy, peaks at 532.4 eV and 534.0 eV can be related to the oxygenated species present in the surface layer formed with GC.

The Li 1s spectrum consists of two components. The first at 53.7 eV is attributed to lattice Li from $LiCoO_2$ and the second at 56.3 eV corresponding to LiF.

The C 1s spectrum has four components. Hydrocarbons and aliphatic carbon appear at lower binding energies, 285.4 eV, while at higher binding energies, components at 287.3, 288.7 and 290 eV may be assigned to C-O, COO and CO_3^- like carbon environments [14].

The F 1s signal can be associated to what was observed on the Li 1s spectrum since it

Table 6.2: Chemical composition of the ZrO_2- or LiPON- coated $LiCoO_2$ cathode after battery cycling.

Peak	$\mathbf{E_B}$ **(eV)**	**Assignment**
Co 2p	779.7	$LiCoO_2$
	786.8	sat II+
	789.8	sat III+
F 1s	685.5	LiF
	686	$LiPF_6$
	687.7-688.4	-
O 1s	529.3-530	$LiCoO_2$
	531-532,7	Li_2CO_3
	533-534	Polycarbonate
N 1s	399.4	LiPON (Nd)
	397.9	LiPON (Nt)
	402	LiPON surface
Zr 3d	182.6	ZrO_2
	184	ZrO_2
	187.2	
P 2p	133.5-133.9	LiPON /PO_4^{3-}
	134.9	PO_xF_y
	136.7	$LiPF_6$
Li 1s	53.8	$LiCoO_2$
	55.3	LiPON
	56.3	LiF

presents a very intense peak at 685.7 eV which corresponds to LiF and another weak peak at higher binding energies related to salt compounds of the type $Li_xP_yF_z$. The presence of products of salt decomposition containing phosphorus can be seen as well on the P 2p spectrum appearing at 135 eV with additional fluorophosphate $Li_xP_yOF_z$, which have a higher binding energy, at 136 eV. The Zr 3d spectrum obtained, (Figure 6.10) shows a shift from the initial doublet towards 182 eV and 185 eV, with an additional component appearing at 187.1 eV.

6.4.2.2 LiPON coating

As the initial surface layer, the XPS analysis showed that the cycled layer is composed of Li, P, O, N, C and F.

The Li 1s spectrum of the cycled LiPON coated $LiCoO_2$ film evidenced the presence of LiF and lithium fluorophosphate species $Li_xP_yF_z$. However, a quantification of these species showed that the amount of the fluorine compounds present in the LiPON-coated are less compared to the uncoated $LiCoO_2$. The highest intensity component is nevertheless the Li from the coating (LiPON) appearing at 55.5 eV. O 1s core peak presents the typical ratio as for LiPON with an additional small presence of oxygenated species at higher binding energies. One of the most important features observed for these layers is the inversion of the ratios of N 1s spectrum components, as it is seen on Figure 6.10. In this case the different shape observed serves as an indication that surface reactions are occurring at the interface layers with the electrolyte during electrochemical activity. The P 2p peak shows a more important presence of phosphates on the layer after electrochemistry, therefore suggesting that the newly formed layer results in inorganic components involving the electrolyte salt, phosphates and nitrides.

The O 1s spectrum of cycled ZrO_2 sample presents a larger emissions coming from oxygenated species with C-O bonds compared to LiPON coated and uncoated samples. This is also seen in the C 1s peak, which evidences more polymeric units in the ZrO_2-coating compared to the LiPON coated $LiCoO_2$, but less than for the uncoated sample. There is an additional Li 1s component appearing at higher binding energies attributed to LiF. These two findings agree with what was found for the uncoated layers (Chapter 5), where large amounts of LiF salt is associated with the formation of polymeric chains. The surface layers reported in literature until now show degradation products from electrolytes, as for example $LiPF_6$ and will form an organic/inorganic layer mainly with carbon, lithium and oxygen. As seen by Aurbach et al [140], a main component of the surface layers on different cathode materials are Li_2CO_3 with $ROCO_2Li$ and polycarbonate species. The results found for the ZrO_2-coated sample showed how this surface presented the highest amount of carbon which was evidenced by the significant aliphatic peak when compared to LiPON-coated and uncoated samples. A possible reason is the presence of reduced Co^{2+} and an oxygen deficient layer formed after the thin ZrO_2 layer is sputtered, as seen on the Co 2p spectrum from before cycling (Figure 6.8). This surface layer may favor the nucleophilic reactions with the alkyl carbonate in the electrolyte as reported by Aurbach et al. [140].

Nevertheless, the overall impression is that this layer does not serve as an homogeneous shielding coverage which confirms the morphology results obtained with SEM imaging. Thus an inhomogeneous film may create gaps where the Li ions will migrate but at the same time it will give space for the reactions at the electrode-electrolyte to occur. Reports from Kim et al. on ZrO_2 -coated spinel electrodes presented improved electrochemical stability due to the lack of electrochemical reactions between coating and electrode, as well as the high porosity of the ZrO_2 with holds HF and H_2O from the electrolyte, minimizing the solubility of the spinel electrode. This is in accordance with the XPS results presented here, since the surface layer is mainly containing inorganic species, those related to salt decomposition products which may be trapped in the ZrO_2 porosity [147].

XPS analyses showed how both coatings have a different surface composition. The fact that the charge/discharge capacity for the 22 first cycles of both coating samples result at the same value may indicate that these two systems have similar efficacy even though their natures are inorganically (for ZrO_2) and organically based (for LiPON).

6.5 Conclusions

The protection mechanism and enhanced capacity retention for the first cycles was found to be related not only to the creation of a physical barrier which isolates the cathode material from the electrolyte, but also on the formation of a surface layer generated by chemical reactions between the coating-layer (created on $LiCoO_2$ from coating preparation by sputtering) and the electrolyte. These artificially created surface layers presented particularities based on the chemical composition of the coating and thickness.

The artificial layer founded on $ZroO_2$ gave an inhomogeneous coverage of the $LiCoO_2$ surface, producing two main effects on the cathode; i) formation of reduced Co^{2+} ions, and ii) generation of an oxygen deficient surface. This second point may facilitate nucleophilic reactions with the electrolyte, which is evidenced by the significant amount of oxygenated and polymeric species compared to LiPON-coated and uncoated. The amount of salt decomposition compounds observed are more than for LiPON, but less than for $LiCoO_2$. The resulting surface layer has mainly an inorganic nature.

A different scene is observed for the LiPON-coated $LiCoO_2$ thin films. Opposite to the ZrO_2, and since the coating layer before electrochemistry was exclusively LiPON, the composition of the layer obtained after cycling was significantly different, mainly LiPON related species, arising from the reaction of P and N with the salt components and with the electrolyte compounds, respectively.

Both coatings present a significantly different surface layer, mainly related to the original nature of the coating. On one hand the ZrO_2-coated cathode showed inorganic species, while the LiPON-coated cathode evidenced a more organic nature.

Chapter 7

Structural study on lithium phosphorus oxynitride LiPON thin films

Glassy ion conducting oxide films have properties that are appealing for advanced technological applications. The importance of developing these materials as thin films is seen from recent advances in solid state electrochemical applications. Given the electrochemical stability and ionic conducting properties that lithium phosphorus oxynitride (LiPON) presents, it serves as a good option to be implemented as amorphous electrolyte in all solid state lithium ion batteries, for example.

The techniques used to produce thin film glassy oxides include evaporation, pulsed laser deposition (PLD) and sputtering. Studies show that these preparation methods give materials with different properties and chemical compositions. For LiPON there is a wide range of compositions that can be obtained from rf sputtering. Reports on thin films show values of $\mathsf{Li}_{2.1-3.7}\mathsf{PO}_{2.9-3.8}\mathsf{N}_{0.2-0.7}$ done by Dudney et al. [32, 35], and $\mathsf{Li}_{2.6-3.5}\mathsf{PO}_{1.9-3.8}\mathsf{N}_{0.1-1.3}$ by Fleutot et al. [42], for example. Even though many studies have focused on the effect of deposition parameters on the final properties of the material, there is still no general agreement [31, 42, 44, 45, 129, 130, 133, 197, 198].

Additionally the method of preparation may also influence the structural characteristics of the films. Several studies comparing the properties of bulk glasses prepared with traditional melt quenching technique and thin film glassy materials deposited with sputtering have been made [138]. Even though both materials had the same nominal composition the final infrared (IR) results showed differences in the short range order (SRO). Therefore it is important to look at sputtered films and study the effect of structure and properties, like e.g ionic conductivity. In this way thin film engineering technology has many challenges to fully understand the process by which glassy oxides are deposited and the correlation between composition, structure, properties, and deposition parameters.

Glasses are prepared by introducing a glass modifier to the base network. Phosphate glasses are founded on a P_2O_5 3-D network where the introduction of the glass modifier breaks P-O-P bonds. The most common glass modifiers are alkali or alkali-earth oxides, e.g. Li_2O, Na_2O and CaO. Depending on the amount of modifying cations introduced into the structure the number of P-O-P bonds with bridging oxygen decrease leading to the formation of non bridging oxygen (Onb). The character of these new bonds change from covalent to ionic giving the material different properties.

The final phosphate tetrahedral units formed are described by the notation Q^i where i denotes the number of bridging oxygen per phosphate unit. A pure P_2O_5 phosphate network with only bridging oxygen (Ob) will result in Q^3 ultraphosphate units forming a highly cross linked structure. When a small amount of modifier oxide is added, Q^2, metaphosphate units are formed. These structures are characterized by having long chains or rings. Increasing the amount of modifier cation even further, i.e breaking up even more bridging oxygen bonds, will result in pyrophosphate and orthophosphate units with isolated Q^1 and Q^0 structures, respectively. Figure 7.1 shows the different tetrahedral sites found in phosphate glasses.

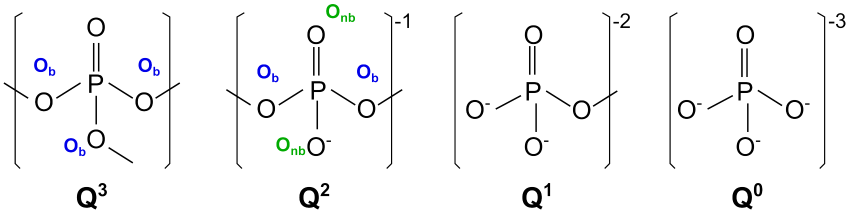

Figure 7.1: Q^i units describing the tetrahedral sites found in phosphate glasses.

Most amorphous oxides exhibit low ionic conductivity at room temperature. Nitrogen incorporation in thin film glassy materials has been studied thoroughly since it is thought to be a determinant factor for enhancing ionic conductivity [194, 199–201]. Additionally, doping phosphate glasses with nitrogen serves to improve chemical durability as well as to increase hardness, de-vitrification temperature, and resistance to attack by water and salt solutions [114, 202–205]. Several authors have found that the final structural and functional properties of sputtered thin films depend on the deposition parameters used. Improvement of ionic conductivity in borates and phosphates by substitution of nitrogen for oxygen has been done successfully in recent years [136, 204]. Nevertheless key concepts concerning the mechanism of nitrogenation and its effect on the ionic conductivity of LiPON films remain unclear. Studies done on annealing have also shown improvements on the conductivity properties of thin films [194, 206]. However, these studies are scarce and questions concerning the effect of thermal treatments on the structure are still unclear.

To elucidate the effect nitrogen or annealing have on LiPON thin films it is of importance to understand the final structural and chemical properties of the material.

In this chapter the composition and the short-medium range structure of the glass networks were examined by X-ray photoelectron spectroscopy (XPS) and infrared spectroscopy

(IR). Additionally the effect on the final electrochemical properties of the film, i.e. ionic conductivity, was studied with electrochemical impedance spectroscopy (EIS).

7.1 Experimental

7.1.1 Sample preparation

A set of lithium phosphates and lithium phosphorus oxynitride thin films were deposited with rf magnetron sputtering starting from a crystalline Li_3PO_4 target. Film depositions were done in the Daisy-Bat (Section 3.1.1), at the TU Darmstadt. Samples were prepared on (1 0 0) silicon wafers polished on both sides. Different nitrogen and argon mixtures were used with $8{\cdot}10^{-3}$ mbar pressure to have a step wise oxygen-nitrogen substitution series. Deposition parameters were set to obtain film thickness of approximately 1 μm (40 W rf power for 4h) suitable for IR transmittance measurements [136, 138]. Table 7.1 summarizes the deposition flow rates used for the experiments, from pure argon to pure nitrogen, which will be addressed as the *nitrogenation series* hereafter. Additional thin films were prepared at the ICMCB laboratory in a sputter chamber under a N_2 plasma for 4 h at 40 W and $1{\cdot}10^{-2}$ mbar pressure.

Table 7.1: N_2 and Ar flow rates (sccm) for the nitrogenation series of lithium phosphate and lithium phosphorus oxynitride sputtered films.

Sample	N_2 flow rate (sccm)	Ar flow rate (sccm)
N0-10	0	10
N0.5-9.5	0.5	9.5
N1-9	1	9
N3-7	3	7
N4-6	4	6
N5-5	5	5
N10-0	10	0

To complete the structural study, an additional set of lithium phosphorus oxynitride films were prepared with the same deposition parameters as stated before and with the highest nitrogen flow that can be set in the sputtering chamber. These films were subsequently annealed in vacuum with a base pressure of $1{\cdot}10^{-7}$ mbar for 1 hour. The different annealing temperatures used were T_A = 250, 320, 380 and 500°C. These experiments will be addressed in the document as the *annealed series.*

X-ray Photoelectron Spectroscopy (XPS) was performed on each sample after every deposition or annealing process. The Li 1s, P 2p, O 1s, N 1s core levels peaks and valence band were recorded using monochromated Al Kα radiation with hv= 1486.6 eV and a pass energy of 23.50 eV.

For the analysis of lithium phosphates and lithium phosphorus oxynitride film structure, infrared spectroscopy (IR) was used. The IR transmission spectra were recorded on a Bruker Vertex 70 v spectrometer, working under vacuum, equipped with DTGS detectors and two beam splitters (KBr or mylar multilayer). A total of 200 scans were averaged with a resolution of 4 cm $^{-1}$. A glove bag was attached to the IR spectrometer which was used for the handling and exchange of samples. The importance of this set-up will be treated further in this chapter.

In order the investigate the ionic conductivity of annealed samples, Electrochemical Impedance spectroscopy was performed, at TU-Darmstadt (TUD) on thin films prepared on a silicon wafer with Si/SiO_2/TiO_2/Pt layers from GMEK, with a top Au contact deposited using a shadow mask. Additional thin films were sputtered at ICMCB-Bordeaux, on glass substrates, using copper (Cu) thin films as current collectors. The 200 nm Cu electrodes were also deposited by sputtering in argon plasma. As shown on Section 3.2.6.3, measurements were done on cells with sandwich structures of 4 mm^2 area, in an argon filled measurement cell.

X-ray diffraction experiments were done on a Bruker diffractometer to determine changes in film density and possible crystallization after the annealing step.

7.2 Results and Discussion

7.2.1 Stability of deposited films to air exposure

Figure 7.2 presents IR transmittance spectrum of samples prepared in argon and shows the effect of exposing the layers to air. Spectral results show broad peaks for far and mid IR regions for a layer that was in contact with air after deposition and a layer kept under a controlled environment. The particular broadness observed for the far and mid IR regions is proof of the disordered structure present in amorphous materials.

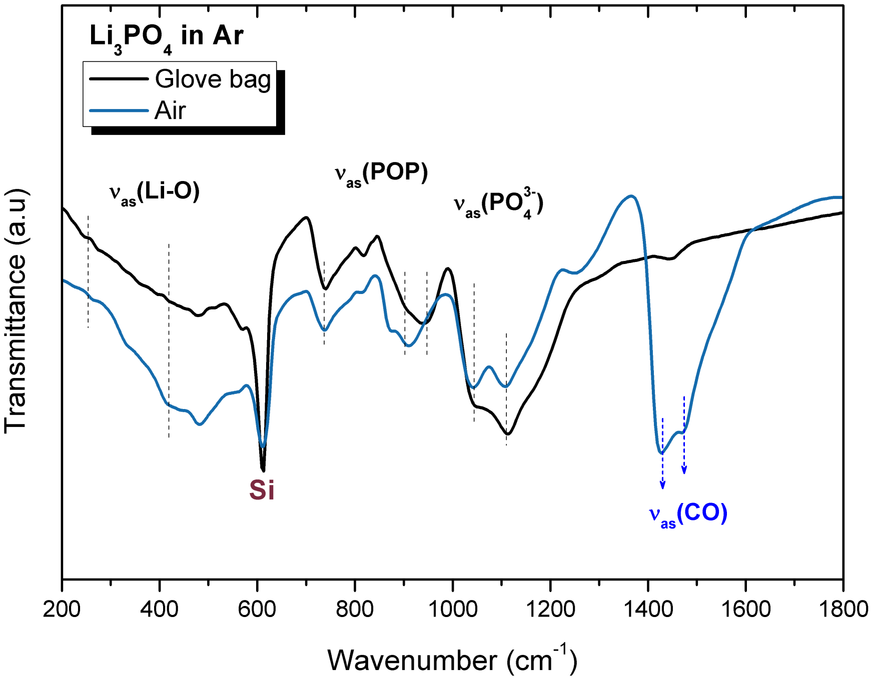

Figure 7.2: IR spectra of thin films of rf Sputtered Li_3PO_4 in argon kept under controlled environment and exposed to air.

The sharp peak observed at around 610 cm^{-1}corresponds to the silicon substrate. The assignments of the IR bands to the lithium phosphate units present in the thin films were made by comparison of the data with reported values in literature. The detailed assignments from all the expected vibrational modes of lithium phosphate glass films are summarized and shown on Table 7.2.

IR results shows characteristic vibrations for lithium phosphate structural units. The shoulder observed between 1200-1300 $cm^{-1}$is assigned to the asymmetric stretching vibrations of $PO_2{}^-$, $\nu_{as}(\mathsf{PO}_2^-)$, of metaphosphate units, while the peaks appearing between 900-1100 correspond to asymmetric stretching of pyro $\nu_{as}(\mathsf{PO}_3^{2-})$ and orthophosphate $\nu_{as}(\mathsf{PO}_4^{3-})$. Symmetric stretching modes of P-O-P bonds appear in the range of 700-850, while in the far IR region, 200-500 cm^{-1}, the vibrations of Li cations against the anion sites in the oxide matrix appear [138, 207, 208].

Figure 7.2 shows how the sample kept in argon and handled in the glove bag develops a broad peak between 200-500 cm^{-1} and weak doublets between 720-840$cm^{-1}$and 850-950cm^{-1}. Finally it presents two strong broad peaks with maximums at 1030 and 1100 cm^{-1}. The lithium phosphate glass film can be subsequently described as a mixture of Q^0 and Q^1 units with some small Q^2 chains, i.e. ortho, pyro and some metaphosphate chains.

The IR results showed a good match between the fringes in the low IR region for all films. This feature indicates that the a comparison between the samples is valid since the changes

Table 7.2: Assignments of component bands of the infrared spectra of vibrations present in lithium phospate thin film glasses.

Wavenumber (cm^{-1})	Assignment	Reference
200-550	ν(Li^{+}-site) (ν_L, ν_H)	[126]
500-600	$\delta(PO_2^-)$, δ(O-P-O), $\delta(PO_3^{2-})$,	[112, 207–209]
720-840	ν_s(P-O-P)	[112, 207–209]
	Orthophosphate	
1030-1050	$\nu_{as}(PO_4{}^{3-})$	[112, 207–209]
	Pyrophosphate	
900-950	ν_{as}(P-O-P)	[112, 207–209]
~1110	$\nu_{as}(PO_3^{2-})$	[112, 207–209]
	Metaphosphate	
840-980	ν_{as}(P-O-P)	[112, 207–209]
1200-1300	$\nu_{as}(PO_2^-)$	[112, 207–209]

ν_L, ν_H: low and high frequency component

ν_s, ν_{as}: symmetric and asymmetric stretching modes

δ:bending modes

observed in the IR spectra can be attributed to variations in the film structure and not to difference in thickness [136, 138].

The final spectra shown here exemplify the overlap of the different units distributed throughout the glassy network. This feature has been observed as well in studies done on sodium phosphorous oxynitride where the material presents different Q^i units [114].

On the other hand, the sample exposed to air presents variations compared to the one kept in argon. The far IR band appears to be more intense and less broad. Additionally there is an increase in the doublet between 850-950 cm^{-1} while both peaks at 1030 cm^{-1} and 1100 cm^{-1} are seen to be less intense. The most evident difference is observed in the region over 1250 cm^{-1} where there are two bands appearing at 1430 and 1490 cm^{-1}.

As seen before, the peaks at 800 cm^{-1} are attributed to P-O-P vibrations forming short chains. At around 950 cm^{-1}, peaks from Q^0 and Q^1 units are increasing and decreasing respectively compared to the prior sample. Additionally, vibrational modes not related to phosphate nor lithium environments are also observed. These new IR bands can be related to the asymmetric stretching mode of carbonate anions CO_3^{2-}.

To corroborate the presence of Li_2CO_3 the attenuated total reflection (ATR) spectra of powder Li_2CO_3 was measured. Figure 7.3 shows the ATR results compared to the lithium phosphate sample exposed to air. The bands appearing at 1490 cm^{-1} and 1430 cm^{-1} are found to correspond to C=O vibrational modes in lithium carbonate Li_2CO_3 [210]. Furthermore, peaks at 1088 and 871 cm^{-1} are also observed and can be related to stretching of C=O and bending of CO_3.

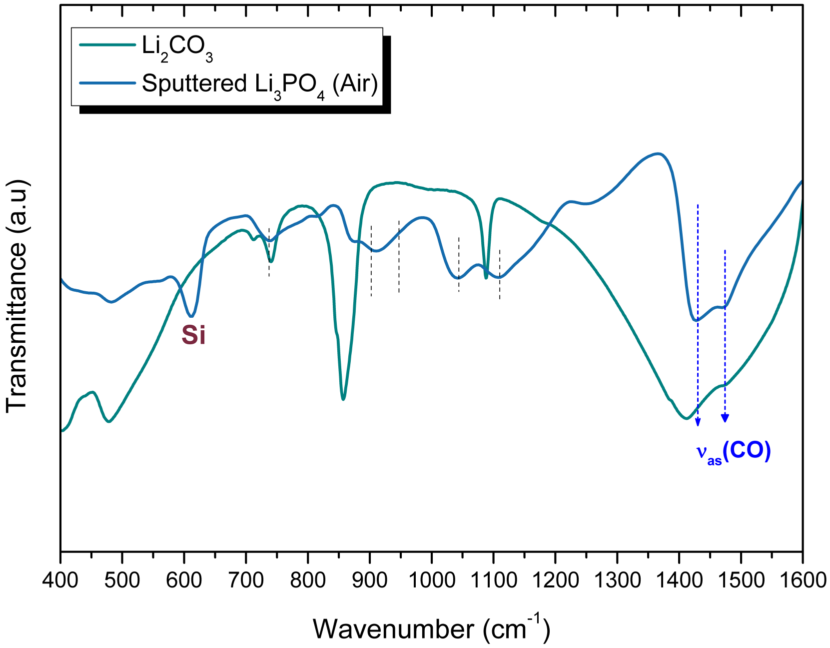

Figure 7.3: Comparison between ATR spectra of Li_2CO_3 powder with IR Transmission spectra of rf Sputtered Li_3PO_4 exposed to air.

The vibrations related to phosphates units are also affected by the presence of carbonate species. As a consequence the strong peak observed at 1030 cm^{-1}, related to orthophosphate units decrease in intensity. Additionally, a peak at 1250 cm^{-1}, appears, which can be attributed to the metaphosphate chain asymmetric vibrations. Peaks assigned to the

P-O-P vibrations, appearing between 850-950, are also seen to increase intensity. As for the far IR region, the relative intensity increases and presents sharper features.

As stated before, the sample exposed to air has a lower amount of Q^0 and Q^1 units compared to the one kept under argon. This feature evidences a higher cross linking of the structure and possible chain growth. Equation 7.1 propose the formation of Li_2CO_3 based on the release of oxide anions and lithium cations, provoking the linking of unstable Q^0 with Q^1 to form small chains based on Q^2 units, and reaction with absorbed CO_2.

$$Li_3PO_4 + CO_2 \rightarrow LiPO_3 + Li_2CO_3 \tag{7.1}$$

As it has been observed, lithium phosphate films are proven to be unstable in air. The apparent chemical stabilization of nitrogenated phosphates has been studied thoroughly for lithium and sodium compounds [202, 204, 211]. Therefore it is valid to determine the chemical stability of the sputtered oxynitride films when exposed to air.

Figure 7.4 shows the IR results of the fully nitrogenated (sample N10-0) and the oxide film prepared in argon (N0-10). Both samples were exposed to air prior to the IR measurements. The spectra clearly shows how after 10 minutes of air exposure the nitrogenated sample suffers no change with no carbonate-related peak. To avoid any type of carbonate contamination all the experiments presented hereafter were done with samples kept under a controlled environment.

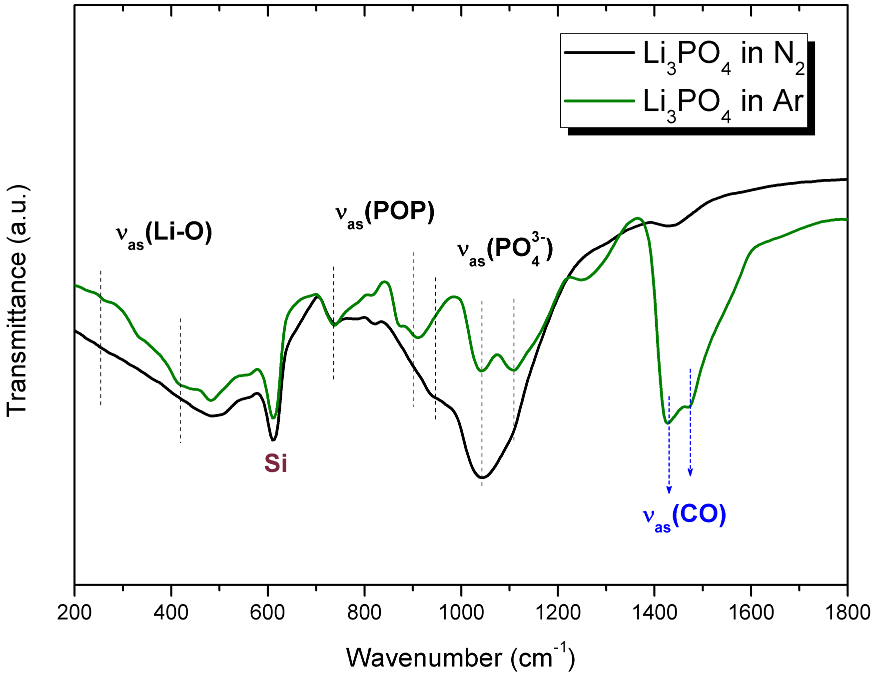

Figure 7.4: IR transmittance spectra of lithium phosphate and lithium phosphorus oxynitride thin films deposited with Ar and N_2 flow and exposed to air for 10 minutes.

7.2.2 Chemical analysis

XPS measurements were carried out for the determination of lithium, nitrogen and oxygen content, for films prepared at different N_2/Ar mixtures. The values of elemental atomic percentage of each layer was used to determined film composition. Results, summarized in Table 7.3, show how the amount of lithium and oxygen content changes with increasing nitrogen flow. Compared to the starting target material, Li_3PO_4, there is an apparent lithium loss during the sputtering process. In this case, the amount of lithium in the film drastically changes with small modification of the nitrogen flow in the reaction chamber.

Table 7.3: Film composition results determined with XPS for lithium phosphorus oxide/oxynitride films prepared with different N_2/Ar flow rates (sccm).

Sample	Film composition
N0-10	$Li_{1.1}PO_{3.3}$
N0.5-9.5	$Li_{0.4}PO_{2.7}N_{0.1}$
N1-9	$Li_{0.5}PO_{2.5}N_{0.4}$
N3-7	$Li_{1.0}PO_{2.6}N_{0.4}$
N4-6	$Li_{0.9}PO_{2.4}N_{0.5}$
N5-5	$Li_{0.9}PO_{2.5}N_{0.5}$
N10-0	$Li_{1.4}PO_{2.2}N_{0.9}$

The resulting composition of the samples agree with previous studies where final properties of thin films greatly depend on the sputtering process and deposition parameters. This difference in lithium content obtained with XPS should be handled with care when comparing samples within each series (nitrogenation and annealing).

Figure 7.5 examines the values of incorporated nitrogen and the final amount of oxygen in the sputtered films function of the nitrogen flow. Results show that lower flow rates give a fast increase in nitrogen incorporation and a fast oxygen decrease while further increase in gas flow shows a modest stabilization.

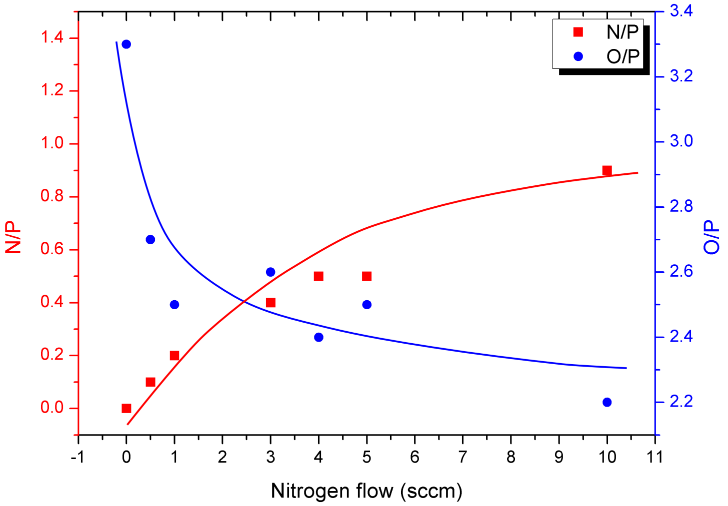

Figure 7.5: Nitrogen incorporation and final oxygen content of sputtered thin films with different N_2 flows. Lines are drawn to describe the tendency.

The XPS data of Li 1s, P 2p, O 1s and N 1s core levels from all lithium phosphate and phosphorus oxynitride films were fitted using a Voigt profile. The results of Li 1s peaks show a symmetric profile indicating that there are no additional components present in the glassy structures. P 2p peaks resulted in asymmetric and broad features, nevertheless further analysis would be too complex and non reliable. This is the reason why in the present work only fits on N 1s and O 1s core levels were performed. Figure 7.6 shows the profiles of O 1s, N 1s, and P 2p for samples N0-10, N0.5-9.5, N5-5 and N10-0. XPS peak position shifts observed in the samples are due to charging effects related to the electronically insulting nature of these oxide materials [212, 213].

N 1s and O 1s present multi component profiles that vary in the complete nitrogenation series as a result of the different glass compositions. The N1s core level peak was fitted with two components. The deconvolution was set to doubly and triply coordinated nitrogen present in structure, Nd and Nt respectively. The presence of these two types of nitrogen in lithium phosphorus oxynitride films has been proven and studied extensively [123, 135, 214]. For most of the samples the main peak contribution is found to be nitrogen which is bonded to two phosphorus atoms, P-N=P, which appears at lower binding energy in the spectra. On the other hand the shoulder observed at higher binding energies corresponds to nitrogen bonded to three phosphorus atoms >N-. The energy difference between doubly bonded (Nd) and triply bonded (Nt) nitrogen was fitted to be 1.5 eV.

The O 1s was also decomposed into two components. The main emission observed at

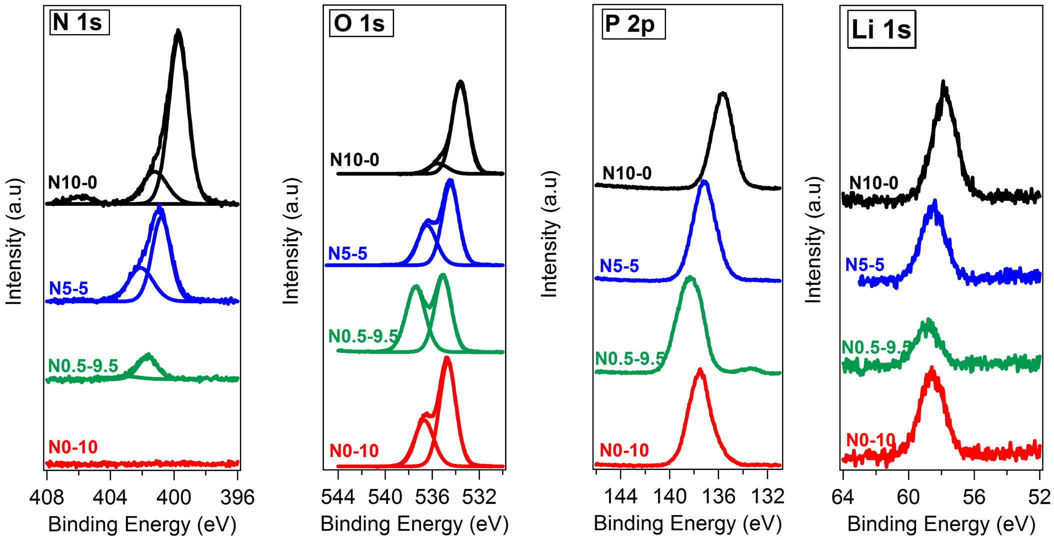

Figure 7.6: XPS profile decomposition of the O 1s, N 1s, P 2p and Li 1s peaks for samples N0-10, N0.5-9.5, N5-5 and N10-0.

low energies corresponds to the non bridging oxygen (Onb) which can be linked to both bonding in P-O-Li$^+$ and P=O. Nevertheless it is not possible to distinguish these two species due to the resonant bonding in the phosphate tetrahedron [33, 214]. The shoulder observed at higher binding energies corresponds to bridging oxygen in P-O-P (Ob). Figure 7.7 shows the evolution of Nt/Nd ratio compared to Ob/Onb ratio as a function of nitrogen incorporation.

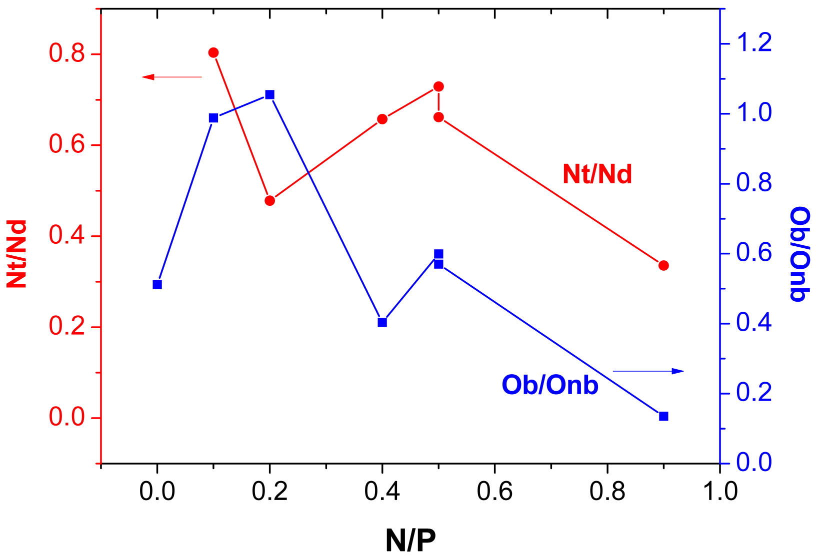

Figure 7.7: Respective Nt/Nd and Ob/Onb ratios determined by XPS in function of the nitrogen incorporation.

The Onb species tend to increase as the nitrogen content increases in the gas flow. In the case of Nd and Nt, Figure 7.7 shows the particular trend these two species have. It is observed how at very low nitrogen flow both Nd and Nt are formed in the same extent, but as the flow increases the tendency is to form Nd more than Nt. In general Nd increases faster and prevails throughout the whole series. Nevertheless it is important to take care and note that the changes observed here are also due to the different lithium content throughout the whole series. Reason why any conclusions drawn by the full series will result in some inaccuracy.

7.2.3 Structural analysis

As mentioned in the experimental part all infrared transmission spectra were collected to study the glass structure. Nevertheless, for a more reliable comparison between samples the final spectra were normalized and converted to absorption. The IR absorption spectra of the lithium phosphorus oxynitride thin films prepared at different N_2/Ar flow rates are shown on Figure 7.8.

The main vibrational peaks corresponding to different phosphate units are observed. Even though a clear trend with nitrogen incorporation is not observed, it is possible to detect similarities in spectral features between some samples. For example, N10-0 and N5-5, as well as N4-6, N3-7 and N0-10. While sample N0.5-9.5 has particular features different

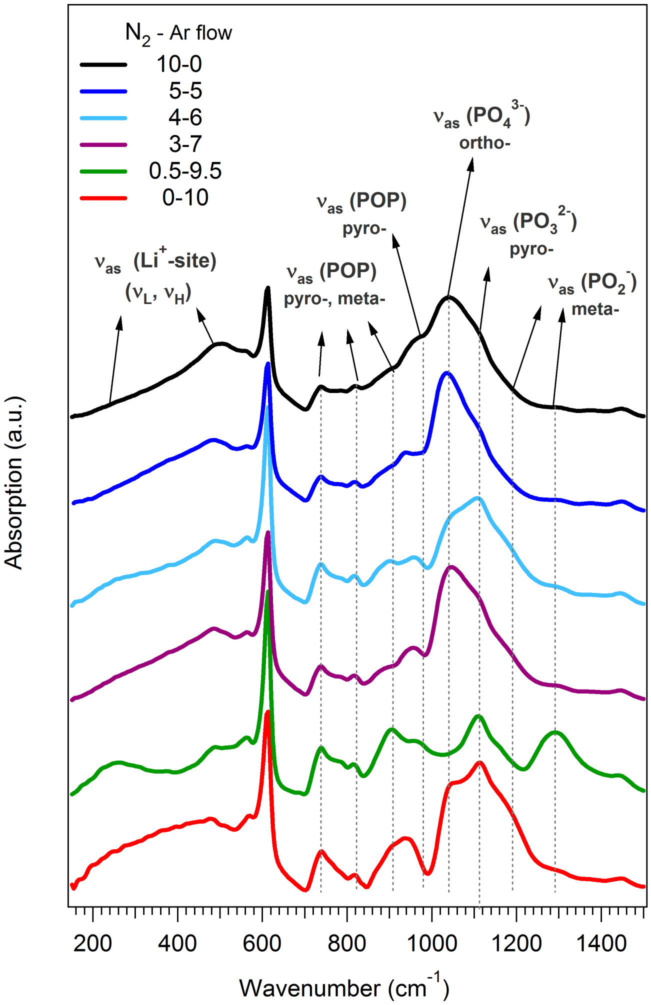

Figure 7.8: IR absorption spectra of lithium phosphorus oxynitride thin films for different N$_2$/Ar flow rates.

from the rest. The main characteristics of the IR spectra of the different sets of samples are summarized below:

- All samples have a weak doublet between 740-820 cm^{-1} .
- N10-0, N5-5 and N3-7 have a strong peak at 1040 cm^{-1} with medium shoulders at 960 cm^{-1} and 1110 cm^{-1} plus a broad peak at around 500 cm^{-1}.
- Samples N4-6 and N0-10 have a broader peak in the far IR region arising between 200-500 cm^{-1}. While in the mid IR region weak doublets between 900 cm^{-1} and 1000 cm^{-1} appear with a shoulder at 1200 cm^{-1}.
- Sample N0.5-9.5 has weaker bands in the far IR region, one at 220 cm^{-1} and another at 550 cm^{-1}. While in the mid IR region it has an intense doublet between 900-1000 cm^{-1}

and moderate peaks at 1150 cm^{-1} and 1300 cm^{-1}.

The isolated Q^0 orthophosphate PO_4^{3-} environment is found between 1030-1050 cm^{-1} and is observed in greater extent for higher nitrogenated samples (N10-0, N5-5 and N3-6). Samples N4-6 and N0-10 have higher amounts of Q^1 pyrophosphate units evidenced by the increase in the peak at 1110 cm^{-1}. Further, sample N0.5-9.5 has a structure composed mainly of Q^2 units, proven by the presence of vibrations at 902 cm^{-1} and 947 cm^{-1} which correspond to small metaphosphate chains and rings, and for longer chains the corresponding peak at 1300 cm^{-1}.

Given that oxygen and nitrogen have similar molecular weight, it is not expected to find big spectral changes. There is nevertheless a possible overlap of the signals due to the proximity of the absorptions of P-O and P-N [114]. This is evidenced by peak broadening observed in Figure 7.8 with nitrogen incorporation.

The XPS and IR results shown until now evidence how deposition parameters induce the formation of phosphate networks formed by different chain lengths, thus a variety of phosphate units. This effect is mainly due to lithium concentration variations in the material and less to nitrogen incorporation.

Nevertheless, due to the difference in lithium content it is hard to single out the real effect of nitrogen incorporation on the structure. For this reason, and to elucidate the dependence between the nitrogenation process and the different component environments, samples with the same overall amount of lithium (observed from IR results) were selected for further analysis.

Figure 7.9 presents the absorption spectra of N10-0, N5-5 and N0-10*. Sample N0-10* was prepared in full argon flow with similar deposition parameters than the rest of the nitrogenation series.

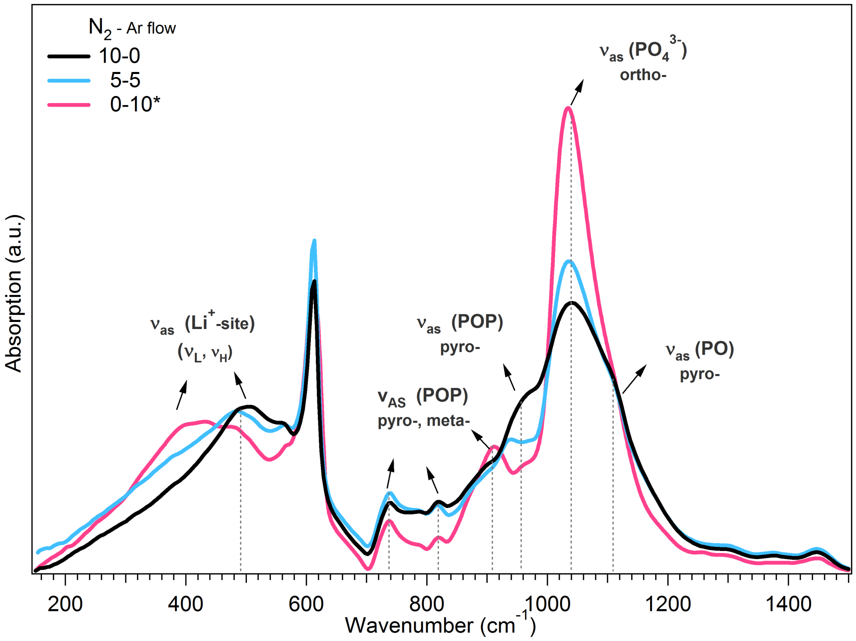

Figure 7.9: IR absoprtion spectra of lithium phosphorus oxynitride thin films for samples N10-0, N5-5 and N0-10*.

The set of selected samples have a pronounced peak at 1035 cm^{-1} due to isolated Q^0 units, as seen on Figure 7.9. With higher nitrogen flows the ionic P-O$^-$ bond in the PO$_4^{3-}$ units does not shift, nevertheless it has an important decrease in intensity. Additionally, it is possible to observe that with increasing nitrogen there is an increase in intensity of the peaks at 840, 960 and 1150 cm^{-1}. On the other hand, it is possible to observe a decrease of the area peak around 910 cm^{-1} correlated to the asymmetric stretching of phosphate bridges. The differences observed in the mid IR region show how the short range order is affected with the incorporation of nitrogen (decrease in Q^0 and increase of Q^1) generating a higher cross linking of the network.

Focusing on the far IR region related to the Li cation vibrations against their sites, it is possible to observe the frequency of the peak shift changing from 400 cm^{-1} to 500 cm^{-1}. The broad envelope present from 200 cm^{-1} until 600 cm^{-1} in the argon sample becomes narrower and shifts progressively, thus showing how incorporation of nitrogen greatly influences the lithium environment.

To have a better idea of how the glassy network and the lithium environment of fully (N10-0), partially (N5-5) and non nitrogenated (N0-10*) samples are changing, difference spectra are calculated. Figure 7.10 compares the spectral changes between the full oxynitride and the oxide (N10-0 - N0-10*) and the changes between the full oxynitride and the partially nitrogenated (N10-0 - N5-5) sample.

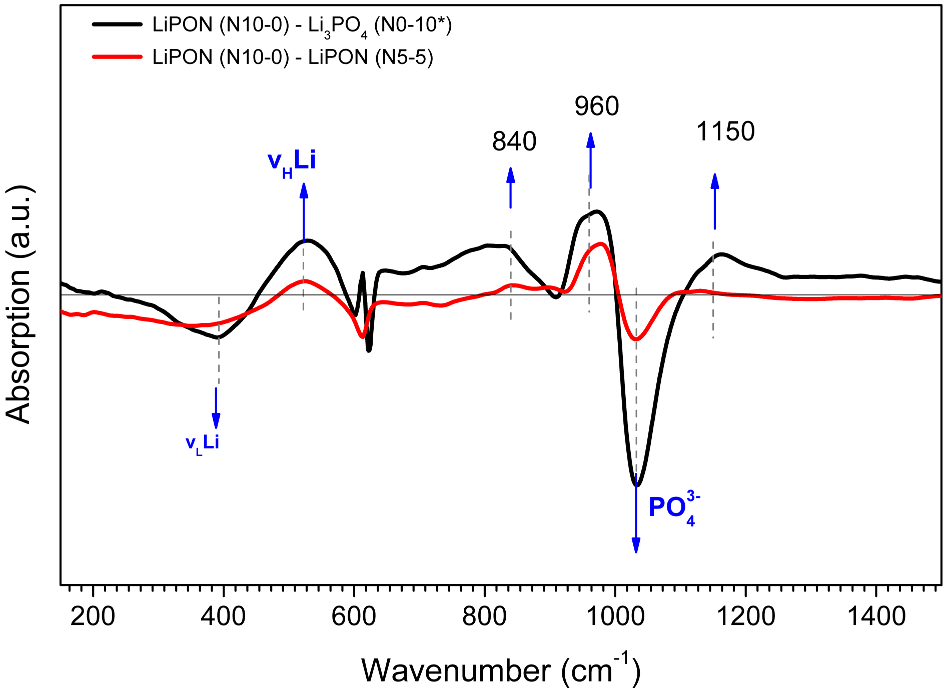

Figure 7.10: Infrared absorption difference spectra of fully (N10-0), partially (N5-5) and non nitrogenated (N0-10*) lithium phosphate thin films.

The mid IR region of Figure 7.10 confirms how the N10-0 full oxynitride film has the lowest amount of orthophosphate units (1035 cm^{-1}) and how the PO_4^{3-} units decrease with nitrogen incorporation. In the same way it is possible to corroborate that the full oxynitride presents more pyrophosphate units, peaks between 900-950 cm^{-1} and 1100-1200 cm^{-1}, and how these units increase with increasing nitrogen. One could then assume that the higher cross linking, arising from the formation of pyro-oxynitrides, is at the expense of lithium orthophosphate units that link to nitrogen atoms affecting the glassy network. At this point it is important to recall the fact that the selected samples ((N10-0),(N5-5) and (N0-10*)) were chosen based on the assumption that they all present similar lithium content based on the IR measurements. Therefore newly formed nitride units must be equivalent to the orthophosphate units present in the starting oxide.
The composition of the units should also be in accordance, to a certain extent, with the XPS results obtained before. XPS analysis showed that for sample N10-0, doubly bonded nitrogen Nd (=N-) is mainly present, around 75% of the total nitrogen amount. Therefore, any proposed cluster forming the network should include dimeric units with doubly bonded

nitrogen with the same Li content.

Many studies have proposed mechanisms showing the possible bonding of nitrogen can have in oxynitrides [123, 137, 204, 215]. Figure 7.11 shows the clusters proposed based on the XPS and IR results that elucidate the substitution of the bridging oxygen with nitrogen. As noted before, and due to the loss of lithium during deposition, the oxide network is formed of a mixture of a orthophosphate and pyrophosphate units, which are respectively depicted in Figure 7.11(a) and (b).

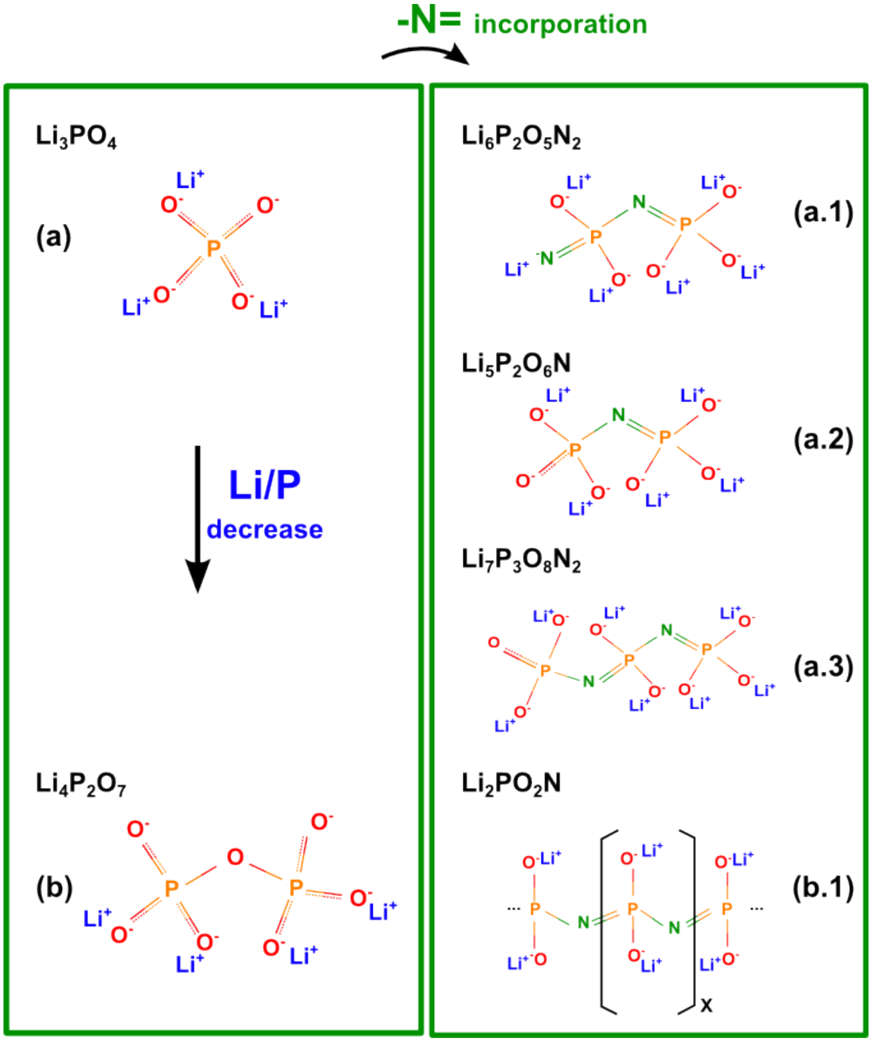

Figure 7.11: Proposed clusters with nitrogen incorporated to lithium phosphate dimeric unit(a) with one N (b) and two N atoms (c).

Cluster (a) and (b) show the lithium phosphate monomer and the pyrophosphate unit. The resulting Li/P ratio in each case is 3 and 2 respectively. Given that our IR results showed that the deposited layers are composed mainly of dimers with the presence of some monomers, the possible structures present in the layers should fall between these two oxides (cluster (a) and (b)). If one assumes that the Li content from each initial phosphate unit remains unmodified, the equivalent structures are clusters (a.1) and (b.1). Introducing nitrogen in the second case (b.1), Li/P=2, results in a pyro-oxynitride in which the corresponding unit will have a composition of Li_2PO_2N where each phosphorus atom will have two corresponding non-bridging oxygen atoms linked to Li^+ ions. As can be noted, the equivalent pyro-oxynitride will have very long chains of phosphates, a feature that is not present in the IR results. Therefore the possible structures should contain higher amounts of lithium, close to Li/P = 3. IR results showed additionally how the deposited layers are composed mainly of dimeric units with some monomers. To resemble structure (a), cluster (a.1) is proposed. The final structure will be $Li_6P_2O_5N_2$. In this case two nitrogen atoms are incorporated forming a dimeric unit which has two types of phosphorus atoms, one attached to three Onb and one N and the other joined to two Onb and two N atoms. Correlating this to IR vibrations, each phosphorus atom is expected to have a characteristic vibration profile. The proposed corresponding dimeric unit (a.1) serves as a theoretical example of the nitrogen incorporation of one nitrogen connecting the two monomers, resulting in a structure with final composition $Li_5P_2O_6N_1$. Cluster (a.3) further presents a three-phosphorus unit with two doubly bonded nitrogen atoms. In this case the resulting structure is $Li_7P_3O_8N_2$. It is possible to assume that the two peaks observed around 800 cm^{-1} and 950 cm^{-1} in the difference spectra (Figure 5(b)) could be related to a complex bridging formation of the nitrogen atoms in the clusters which depend on the type of surrounding environment present.

There are several models developed to explain network formation with nitrogenation in phosphate glasses. Bunker's model and Marchand's rules describe the mechanism by which nitrogen substitute oxygen atoms in metaphosphate glasses. They both coincide that the formation of two Nd and two Nt occur from the breaking of P-O and P=O bonds. For the formation of Nd, -N=, both P-O and P=O are broken, while for >N-, Nt, only P-O bonds are involved. Le Sauze et al have observed that for sodium phosphate the P-O^-Na^+ bonds will not be affected by the nitrogen substitution, but will depend intrinsically on the total cation content [216]. The trend of Ob/Onb for the present study, shown in Figure 7.7, exemplifies the reported data on other alkali metaphosphate glasses [202, 216]. It is nevertheless important to take care that this trend was assumed for layers with the same lithium content, around 1:1 Li:P ratio for metaphosphate case studies.

As stated before the far IR region of the difference spectra, Figure 7.10, shows changes in the lithium environment. The far IR envelop can be analyzed further with deconvolution of the different components present. Figure 7.12 presents fitting results on the far IR region of samples N0-10*, N5-5 and N10-0. Peaks corresponding to the substrate (Si) and the O-P-O deformation bonds were fixed to 610 cm^{-1} and 590 cm^{-1} respectively. The resulting components are two broad bands at around 460 cm^{-1} and 310 cm^{-1}. With nitrogen incorporation both of these bands shift towards higher frequencies. Additionally, the band at higher wavenumber becomes less broad.

In the type of phosphate glassy structures, similar to the ones studied here, lithium ions are found to be in a local minimum of potential energy related to the negatively charged units in the vicinity [126]. The short range order structures serve to accommodate the Li ions with a variety of coordination spheres which can be classified given their nature. Due to this disordered nature of the glass oxide it is possible to find charged, partially-charged and neutral units in the coordination sphere of the metal ion. In this way, the surrounding of the Li ions are specific anionic sites that can come from either non bridging or bridging oxygen of both charged and neutral units [126].

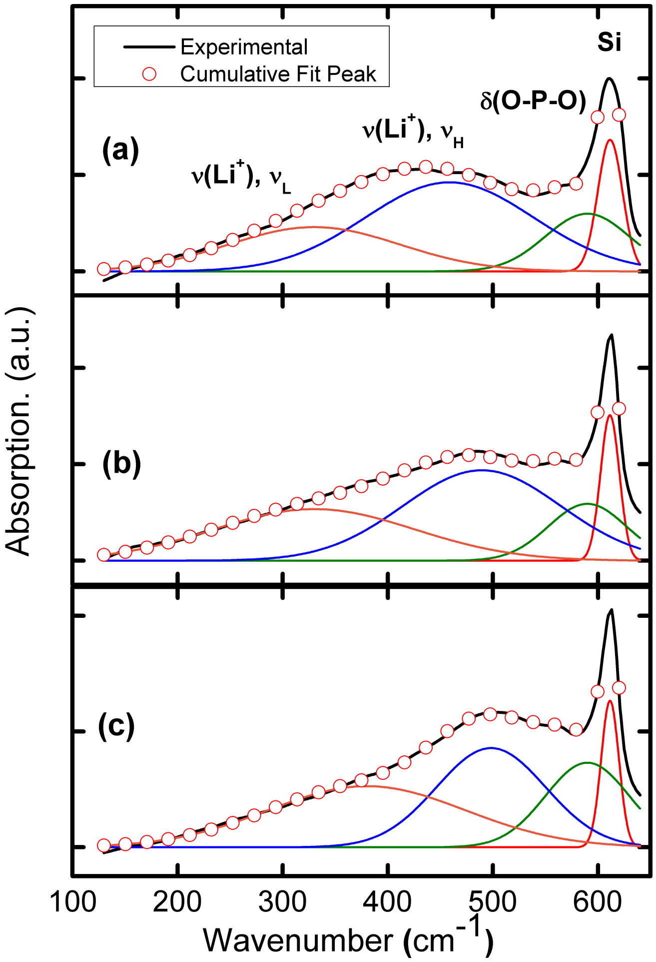

Figure 7.12: Fit results for components present in the far IR region for (a) non nitrogenated sample made in argon (N0-10*), (b) partially nitrogenated (N5-5) and (c) fully nitrogenated (N10-0) lithium phosphate thin films.

Kamitsos et al have found that for alkali glasses there are two contributions to the band in the far IR due to the existence of more than one type of anionic hosting for cations [126]. They found that the higher frequency component can be compared to the cation vibration present in the corresponding crystal. On the other hand the lower frequency was related to the unfavored sites with higher coordination number and lower negative charge density. As shown in Figure 7.12, with nitridation the high frequency component becomes more narrow, which will imply a significant increase of the metal ion sites distribution uniformity and therefore an increased ordering of the structure surrounding lithium cations.

As seen before, the introduction of nitrogen will increase the order in the material and place lithium ions in a coordination environment with a lower potential energy. Du and Holzwarth have performed calculations on oxynitride structures where they present the influence of bridging nitrogen on the lithium environment, and how compared to bridging oxygen, it will tend to be stronger [217, 218]. The higher uniform distribution of the N compared to O will increase the charge density surrounding the Li atoms, creating stronger Li-anion interactions. This gives an idea of the reason why nitrogen incorporation serves for chemical stability.The preparation of sputtered films with nitrogen will give stabilizing coordination spheres of Onb or N around lithium atoms which makes it unfavorable for them to react with CO_2 from air.

With these findings it is possible to assign the bands observed between 200 cm^{-1} and 550 cm^{-1} to Li atoms surrounded by different anionic environments. Even though this assumption is based on the far IR results obtained here, further information concerning Li-anion sites distances is needed to conclude on the real glassy network present.

It is also possible to conclude that during nitrogenation the main role of nitrogen is related to the formation of linkages and further modification of the glass structure while oxygen, mainly non-bridging, is related to lithium charge compensation.

7.2.4 Annealing effect on thin film composition and structure

The samples presented in this coming section were deposited and immediately annealed under vacuum (base pressure of $1{\cdot}10^{-7}$) for 1 hour. Subsequent XPS and IR measurements were performed under controlled atmospheres. For EIS measurements, deposition of the layers were done on $Si/SiO_2/TiO_2/Pt$ wafers with a sputtered gold contact done after LiPON deposition. This layer may have influenced the adhesion of the lithium phosphorus oxynitride film and made it difficult to measure XRD and EIS in some cases.

The same data treatment employed for the nitrogenation experiments was applied in the annealing series. Final structural and chemical properties of the thin films were analyzed as function of the different annealing temperatures T_A = 250, 320, 380 and 500 °C. As determined with XPS analysis in the prior section (*nitrogenation series*) annealed samples have a network formed by Nd, Nt, Onb and Ob similar to the fully nitrogenated N10-0 film.

It is important to consider that surface analysis on thermal treated samples at such high temperatures have always the uncertainty in determining if the results obtain correspond exclusively to surface related phenomena or if it extends to bulky features.

XPS deconvolution results, not presented here, revealed how the Ob/Onb ratio has an overall constant behavior through the different annealing temperatures. The changes observed are not significant, thus one can assume how the amount of these two species (Ob and Onb) have only minor changes throughout the range of temperatures studied. On the other hand annealing had an influence on the Nt/Nd ratio for one of the lower temperatures (250°C). This indicates that thermal treatment will give a significant change of the nitrogen environment in the glassy structure but only at lower temperatures and not higher than 250°C.

XRD results for the as deposited and annealed sample at 250°C, are shown on Figure 7.13. Diffraction patterns obtained are in correspondence with amorphous glassy structures with the characteristic broad peak around 22° [44, 45]. The sample annealed at 250°C showed an increase in reflection possibly due to minor gain in ordering of the network.

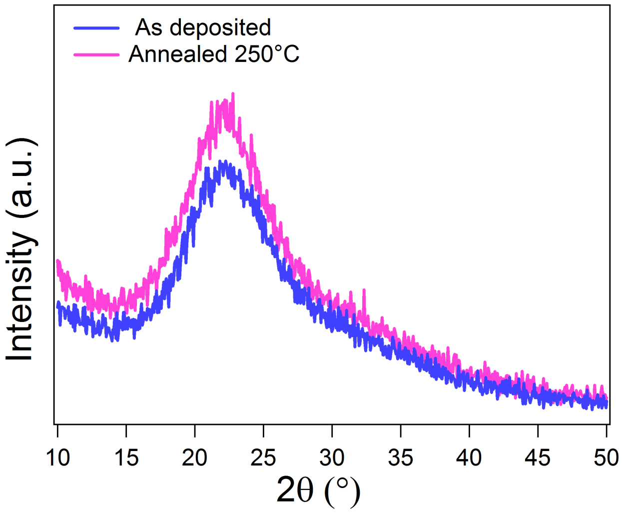

Figure 7.13: X-ray diffraction patterns of as deposited and annealed (250°C) lithium phosphorus oxynitride thin films.

Recent results on MOCVD deposition of Li_3PO_4 [219] show how the preparation of the material at 350°C gives a partially crystallized film with reflections at around 24° corresponding to (1 0 1) and (0 0 1) and at 37° for (0 0 2). Nevertheless the XRD pattern presented here shows no evidence of additional crystal phases indicating that the annealing process did not affect the amorphous character of the layer contributing to a loss of material during crystallization.

7.2.5 Structure and ionic conductivity

In this section, two experimental set ups were employed for the deposition and annealing of LiPON films, one in the TU-Darmstadt and the other at ICMCB-Bordeaux.

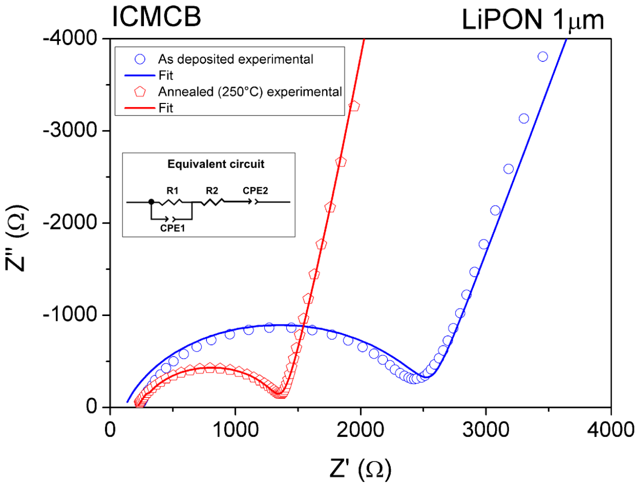

Figure 7.14: Impedance spectra of as deposited LiPON (1 μm thick) and annealed thin films at 250°C, prepared and measured at ICMCB-Bordeaux.

The Nyquist plot of the as deposited and annealed samples (250°C) prepared in ICMCB are shown in Figure 7.14. The analysis and fits of the curves were done using the equivalent circuit shown in Figure 7.14. The spectra is made of a semicircle and straight line signal, which gives a behavior similar to that of an ideal blocking electrode-electrolyte-electrode configuration. The results on ionic conductivity are summarized in Table 7.4 and show that the ionic conductivity doubles after the sample is annealed at 250°C

Table 7.4: Ionic conductivity values of lithium phosphorus oxynitride thin films annealed at different temperatures. *Layers presented delamination. See Figure 7.16.

Sample	Ionic Conductivity (S/cm)
ICMCB	
as deposited	$1.0 \cdot 10^{-6}$
250°C	$2.1 \cdot 10^{-6}$
TUD	
as deposited (80°C)	$8.5 \cdot 10^{-7}$
320°C	$1.9 \cdot 10^{-6}$ *
380°C	-
500°C	$5.5 \cdot 10^{-7}$ *

Figure 7.15 presents the impedance spectra obtained from sputtered layers at TU Darmstadt, i.e as deposited LiPON thin films compared to annealed layers. Measurements were only possible for samples treated at 320 and 500°C, which did not present shorts. Nevertheless, the thermal treatment produced changes in the morphology of the layer, observed with SEM measurements. Figure 7.16 presents two different magnifications of the layer after annealing at 500°C showing cracks and de-lamination on the surface. EIS measurements and ionic conductivity (σ) determination were possible in these two cases (320 and 500°C), but the lack of adhesion make these results unreliable.

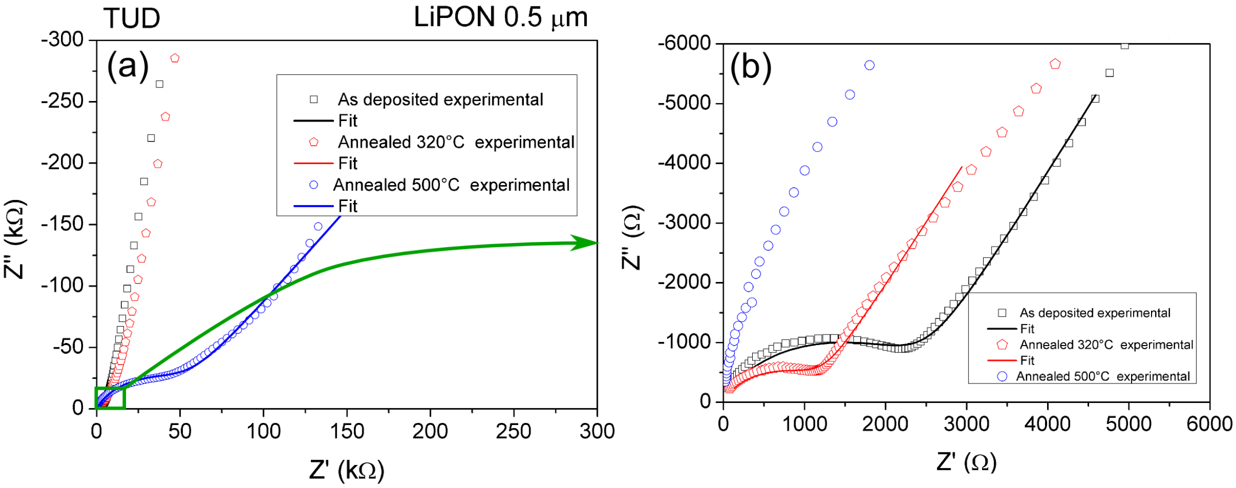

Figure 7.15: (a) Impedance spectra of as deposited LiPON and annealed thin films at 320 and 500°C, prepared and measured at TU Darmstadt. (b) Zoom of impedance spectra. Layers were 0.5 µm thick.

These shorts may occur either due to the LiPON layer not being thick enough (500 nm), or because of the pore or pinhole formation with thermal treatment. Comparing both as-deposited films it is possible to observe the influence of the annealing process on the final ionic conductivity.

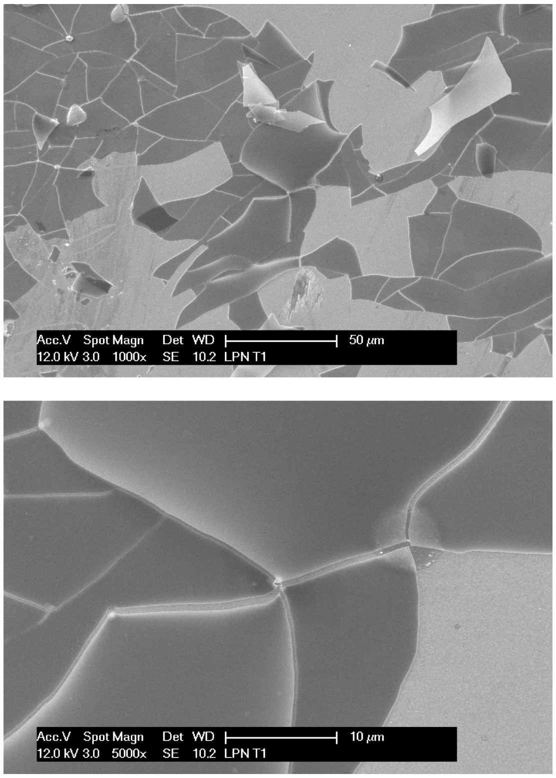

Figure 7.16: SEM images of a LiPON sample after annealing for 1 h at 500°C.

Annealed lithium phosphorus oxynitride thin films were further analyzed with IR spectroscopy. The results, shown on Figure 7.17, evidence minor structural changes after annealing compared to the as deposited sample. The IR absorption spectra shows that all films have the following features:

- A broad envelop between 200 and 500 cm^{-1}.
- A modest doublet between 720 and 840 cm^{-1}.
- A strong peak at 1040 cm^{-1} with shoulders at 960 and 1110 cm^{-1}.

As seen before these vibrations correspond to Li cation against anionic environments between 200-600 cm^{-1}, bending modes of P-O at 720-840 cm^{-1}, asymmetric stretching P-O bonds fo Q^1 and some Q^2 units at 960 cm^{-1}, asymmetric vibrations of PO_4^{3-} at 1040 cm^{-1} and asymmetric vibrations of PO^- in Q^1 units at 1110 cm^{-1}.

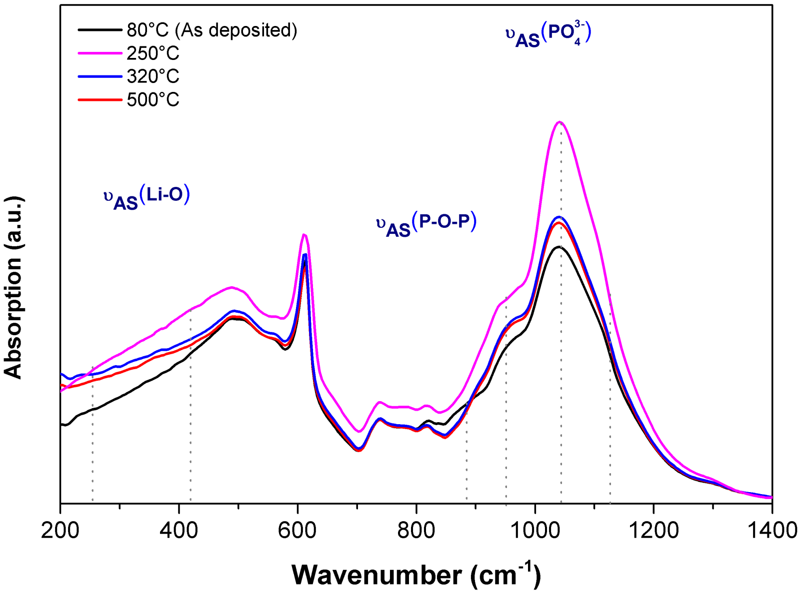

Figure 7.17: Infrared absorption spectra of lithium phosphorus oxynitride thin films annealed at different temperatures.

The minor changes seen at the mid and far IR regions with increasing temperature correspond to modifications of the short range order of the glassy network, evidenced by an increase in the peak related to isolated units. A difference spectra between the as deposited and the annealed sample at 250°C was calculated, where the small changes can be revealed and a better insight of the possible reasons for the enhanced ionic conductivity. Results are presented on Figure 7.18 and are compared to the difference between the as deposited and lithium phosphate (N0-10*) film prepared in argon (taken from the nitrogenation series). The pattern corresponding to the annealed series shows how the heat treatment increases the amount of isolated PO_4^{3-} units and decreases the vibrations between 800-960 cm^{-1} and 500-600 cm^{-1}, which are associated to the P-O-P stretching and O-P-O deformation modes, respectively.

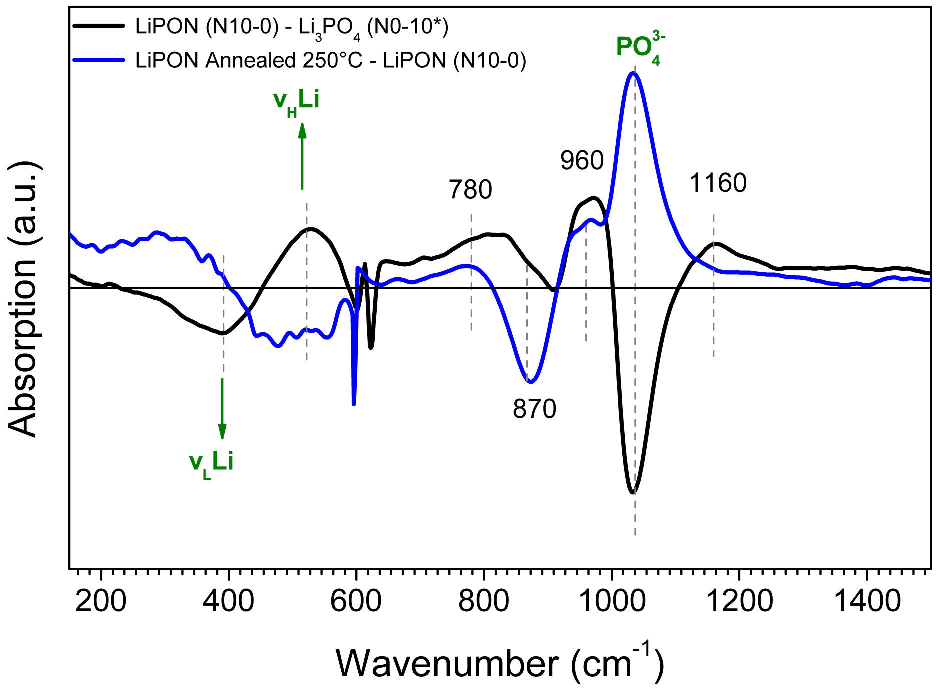

Figure 7.18: Infrared absorption difference spectra of as deposited and annealed (250°C) lithium phosphorus oxynitride thin film.

The mid IR region shows an decrease in the component between 800-900 cm^{-1}. The vibrational frequencies in this region have been associated to the presence of bridges in phosphate glasses. For example, Popovic et al and Velli et al found that long chained structures in metaphosphate have vibrations between 850-950 cm^{-1} for P-O bonds. As seen in the difference spectra, after the film has been annealed at 250°C there is evident decrease in the longer chain components that can be linked to the increase in ortho and pyrophosphate units. It is possible to assume that the energy given to the material provokes breaking of longer chains towards the formation of rings and isolated units.

On another point, Kamitsos et al have explained how annealing creates a slow cooled thin film amorphous state, different from the starting sputtered layer (fast cooled). This change will give the largest effect to the Li-ion motion band (far IR region) indicating that annealing triggers only a set of short range order (SRO) structural rearrangements that modify and/or create Li-sites with lower potential energy. Results shown here are in agreement with these finding and show a similar rearrangement in the Li-O environment and consequently lowering of potential energy upon thermal treatment [125, 138].

In this line of thought, assuming that the glass is linked through non-flexible negative charge in the phosphate network, a lowering in potential energy will induce an increase in the activation energy, which stems lithium transport. This would then mean that the ionic conductivity, which depends on the density of mobile Li ions and mobility, will also decrease. This last point contradicts the finding on ionic conductivity shown here. However, Dussauze et al have reported how the nitridation process on lithium boron oxynitride gives B-N-B bridges in contact with highly coordinated boron atoms (3-fold). They argue that the close contact of these units favors de-localization of negative charge of both oxygen and nitrogen atoms along the oxynitride structure [136]. This de-localization, or bond resonance, decreases the electrostatic interactions between Li and the surrounding sites. Therefore, if one assumes that for lithium oxynitrides the charges are flexible due to de-localization of the newly formed P-N bond, it is possible to explain the enhanced lithium mobility (and ionic conductivity). In summary, the two contradictory effects concerning the nature of the oxynitride phosphate network and the lithium environment to enhance chemical stability and ionic conductivity. On one side the far IR showed how the stronger interactions between lithium and the anion site produces a shift and narrowing of the band. Additionally, there will be an increase in glassy network around lithium ions. On the other side, the increased ionic conductivity is more related to the de-localization of negative charges along phosphate dimers and chains. The layers prepared with annealing may have this conductivity enhancement due to de-localization of negative charge in these longer chains making the ion hopping more efficient compared to the untreated sample.

Summing up, annealing the sample at 250°C has two main effects on the structure. One relates to the change in chain length and the other with the rearrangement of coordination environment surrounding Li atoms. Annealing gives the structure enough energy to rearrange and shift from a strained network formed with sputtering to a more relaxed ensemble. The presence of -N= atoms will provide a favorable environment where the de-localization of the charge can occur once the electrostatic part of the activation energy is decreased. Given that the network strain decreases with annealing, the final effect in enhanced ionic conductivity can be fully explained.

7.3 Conclusions

It was possible to enhance the chemical stability of lithium phosphorus oxides, which react with CO_2 from air and forming Li_2CO_3, with nitrogen incorporation.

Composition of phosphate glasses with rf sputtering was proven to be greatly influenced by the gas ratio employed. The largest variations are observed for lower amounts of N_2 in the gas mixture.

The lithium phosphorus oxynitride films deposited here presented glassy structures with mainly ortho and pyrophosphate units with small amounts of short metaphosphate chains.

The IR spectra results showed important differences in the short range order for films with a similar amount of lithium. A clear trend of the vibrational components of isolated PO_4^{3-} units and lithium environment with increasing nitrogen in the gas mixture was observed. Nitrogen insertion favors stability of lithium by giving an environment with lower potential energy.

Annealing at 250°C shows extended effects on the glassy network explained by the decrease of orthophosphate units and increase of the bridging units, and a change in coordination environment surrounding the Li atoms due to negative charge de-localization from doubly bonded nitrogen -N=. The ionic conductivity will be enhanced by the improved Li ion transport given the reduction in the electrostatic part in the activation energy.

LiPON is therefore a material with particularity of its components to form structures with great chemical stability but with high ion mobility and hence ionic conductivity: phosphate coordination, cross linkage, P-N covalency and ability to de-localize the charge and will affect Li^+ bonding in the respective coordination sites and will thus trigger lithium mobility.

Summary

The present work was based on the investigation of different thin film components of Li ion batteries.

A first part was dedicated to the deposition of cathodes in thin film form of a known material, $LiCoO_2$, and an alternative one, $Li(NiMnCo)O_2$ employing physical vapor deposition (PVD) and chemical vapor deposition (CVD), respectively.

A second part was focused on the cathode-electrolyte interface for three case studies: 1) as deposited $LiCoO_2$ cathode thin film, 2) ZrO_2 coated $LiCoO_2$ thin film and 3) LiPON coated $LiCoO_2$ thin film. The interface cathode-electrolyte of these three cases were studied before and after galvanostatic cycling to determine surface layer characteristics and changes arising on the interface after battery operation. The interface of a bare $LiCoO_2$ layer was further studied after soaking in liquid electrolyte to elucidate the effect of short storage procedures in batteries. Additionally, LiPON thin films were studied on the basis of structural changes occurring with nitrogenation and its correlation to a possible mechanism during ion conduction.

Thin film cathode materials

The preparation of $LiCoO_2$ thin films and determination of ideal deposition parameters in terms of surface composition and electrochemical activity was done on the first part. Results obtained showed how the different sputtering parameters clearly affect the chemical composition and electrochemical behavior of the material. The films deposited at 50 W, 550°C and 1:1 O_2:Ar presented a stoichiometric relation for the surface composition of $Li_{0,9}CoO_{2.1}$.

Results showed how after cycling there is a reduction of rate capability and increase in interface resistance. Cyclic voltamogramms showed the thin films with good cyclability for the first 6 cycles. The X-ray diffraction pattern showed the presence of several orientations related to the known HT phases found in literature for $LiCoO_2$ with low crystallinity. This feature was confirmed by the CV curves as well. XRD patterns evidenced a structure change with cycling and the appearance of an additional Co_3O_4 phase.

XPS measurements showed spectral features from the surface corresponding to stoichiometric $LiCoO_2$ which was taken as reference data for the continuing sections.

$Li(Ni_xMn_yCo_{1-x-y})O_2$ thin films were prepared via aerosol assisted chemical vapor deposition. Phase composition, structure and morphology of thin films deposited on silicon substrates were investigated as a function of process pressure and concentration of precursor solution. X-ray diffraction and Rietveld analysis using the March-Dollase model were applied for the determination of the texturing and microstructural characteristics. The morphology of the films was characterized using scanning electron microscopy. The investigation
a significant effect on the film morphology and texturing. Deposited thin films were electrochemically active showing the expected charging/discharging values and reasonable stability during cyclic voltammetry experiments.

Degradation study on a $LiCoO_2$ model electrode

Bulk and surface properties of $LiCoO_2$ thin films were studied before and after electrochemistry. Galvanostatic cycling showed a high decrease in capacity after the first cycle which was related to the poor crystallinity induced by structural changes favored with battery cycling. This significant decrease is not observed for well crystalline thin films. Electrochemical impedance spectroscopy additionally showed the appearance of a resistance associated to the interface layer formed.

Moreover, scanning electron microscopy showed how the deposited layers are polycrystalline with average 30 nm particles. Apart from a smoothening of the particles no major change was observed on the morphology after cycling.

Surface analysis done on $LiCoO_2$ thin films showed changes occurring at the interface layers after the electrode was in short contact with the electrolyte solution and after galvanostatic cycling.

Washing and soaking the electrode material in electrolyte and solvent showed that surface reactions start from the first contact. The formation of a surface layer from these processes occur with organic components from the solvent and inorganic from the salt. The most significant evidence by XPS was the appearance of Co^{2+} metal ion on the surface after soaking and after electrochemistry.

A main component of the electrolyte solution, $LiPF_6$, has critical effect since it can decompose and form HF which reacts with carbonates and forms LiF on the surface. Given the large amount of LiF, a high reactivity of $LiCoO_2$ with the decomposed species was observed, as the main components of the film were related to the decomposed $LiPF_6$ salt.

The remaining surface layer was mainly carbonated species and some inorganic components.

The carbon compounds found correspond to reactions from the EC solvent while the $LiPF_6$ salt formed LiF and other Li_xPF_y compounds, these last in a lower extent.

The surface chemistry of the layer formed on $LiCoO_2$ after cycling was mainly based on decomposed species from the electrolyte salt arising from carbonated and fluorinated species.

Soaking the sample for a short time resulted in the deposition of a surface layer on the active material composed of organic compounds related to the solvent. Contrary, electrochemical cycling favored the formation of inorganic species from the salt on the cathode surface. When the samples are soaked there are more organic species seen than after electrochemistry evidenced by the estimation of carbon containing species related to each sample, around 14% for soaked and 9% after cycling. Finally, the electrolyte salt was seen to decompose and further react generating intermediate species which with any possible water trace can enhance polymerization of solvent and form other additional products.

Artificial surface layers for the $LiCoO_2$ cathode

Artificial surface layers were deposited on $LiCoO_2$ by means of rf sputtering. The thin layers of ZrO_2 and LiPON used as coatings had minor effects on the original film morphology and crystalline structure.

The protection mechanism and enhanced capacity retention for the first cycles observed for coated $LiCoO_2$ thin films was related to two main factors; i) the creation of a physical barrier which isolates the cathode material from the electrolyte, and ii) formation of a surface layer from chemical reactions between the deposited artificial surface layer and the electrolyte.

An XPS analysis of the interface showed how the nature of each layer after galvanostatic cycling was different for each case. The resulting artificial surface layer formed from ZrO_2 coating showed mainly inorganic species, while the LiPON coated cathode showed an organic nature. The final surface layers after electrochemical cycling of the ZrO_2 coated film resembled that of the uncoated $LiCoO_2$.

Structural study on lithium phosphorus oxynitride LiPON thin films

The composition and properties of LiPON deposited with varying parameters was systematically studied. The chemical stability of lithium phosphorus oxides was enhanced with nitrogen incorporation while creating an oxynitride structure.

Composition of phosphate glasses with rf sputtering was proven to be greatly influenced by the gas ratio employed. The largest variations were observed for lower amounts of N_2 in the gas mixture. The IR spectra results showed important differences in the short range order for films with a similar amount of lithium.

The lithium phosphorus oxynitride films deposited here presented glassy structures with mainly ortho and pyro-phosphate units with small amounts of short metaphosphate chains.

Nitrogen insertion favors stability of lithium by giving an environment with lower potential energy, as was evidenced by the far-IR results.

Annealing at 250°C showed extended effects on the glassy network explained by the decreases of orthophosphate units and increase of the bridging units. Moreover, change in coordination environment surrounding the Li atoms due to negative charge de-localization from doubly bonded nitrogen -N= was also observed. The ionic conductivity was enhanced by the improved Li ion transport given the reduction in electrostatic part in the activation energy.

LiPON has the particularity of elements with specific coordination that favors the formation of structures with chemical stability and with high ion mobility. Such attributes are evidenced in the ionic conductivity properties due to phosphate coordination, cross linkage, P-N covalency and ability to de-localize the charge and trigger lithium mobility.

Résumé

Ce travail porte sur la recherche de différentes compositions de couches minces pour accumulateurs Li-ion.

Une première partie a été dédiée au dépôts de cathode sous forme de couche mince d'un matériau connu, $LiCoO_2$, et d'un matériau alternatif, $Li(NiMnCo)O_2$ en utilisant le dépôt physique en phase vapeur (PVD) et le dépôt chimique en phase vapeur (CVD), respectivement.

Une seconde partie s'est focalisée sur l'interface cathode-électrolyte pour trois cas d'étude : 1) couche mince de matériau de cathode $LiCoO_2$, 2) couche mince de $LiCoO_2$ recouvert de ZrO_2 et 3) couche mince de $LiCoO_2$ recouvert de LIPON. L'interface cathode-électrolyte de ces trois cas d'étude a été étudiée avant et après cyclage galvanostatique afin de déterminer les caractéristiques de la couche de surface et les changements provenant à l'interface lors du fonctionnement de l'accumulateur. L'interface des couches minces de $LiCoO_2$ a été étudiée plus en détail après trempage dans un électrolyte liquide afin de comprendre l'effet des procédures de stockages courts dans les accumulateurs. De plus, les couches minces de LiPON ont été étudiées sur la base de changements structuraux se produisant avec la nitruration et sa corrélation à un possible mécanisme ayant lieu durant la conduction ionique.

Couche mince de matériaux de cathode

La préparation des couches minces de $LiCoO_2$ et la détermination des paramètres de dépôt optimaux en termes de composition de surface et d'activité électrochimiques ont été réalisées dans la première partie. Les résultats obtenus montrent comment les différents paramètres de pulvérisation agissent sur la composition chimique et le comportement électrochimique du matériau. Les films déposés a 50 W, 550°C et 1 :1 O_2 :Ar présente une relation stoechiométrique pour une composition en surface de $Li_{0,9}CoO_{2.1}$. Les résultats ont montrés comment, après cyclage, il y a diminution de la capacité à cycler à régime rapide et augmentation de la résistance à l'interface. La voltamétrie cyclique a montré la bonne cyclabilité des couches minces lors des 6 premiers cycles. La diffraction des rayons X a montré la présence de différentes orientations, peu cristallisées, appartenant à la phase $LiCoO_2$ HT selon confirmation par la littérature. Ceci est également confirmé par les courbes de voltamétrie cyclique. Les diagrammes DRX mettent en évidence un changement de structure durant le cyclage et l'apparition d'une phase supplémentaire Co_3O_4. Les mesures XPS ont permis d'obtenir des données provenant de la surface et correspondant à du $LiCoO_2$ stoechiométrique et qui a servi de donnée de référence dans les sections suivantes.

Les couches minces de $Li(Ni_xMn_yCo_{1-x-y})O_2$ ont été préparées par dépôt chimique en phase vapeur assisté par aérosol. La composition, structure et morphologie des couches minces déposées sur substrat de silicium ont été étudiées en fonction de la pression totale et de la concentration de la solution de précurseur. La diffraction des rayons X et l'analyse Rietveld utilisant le modèle March-Dollase a été mise en œuvre pour la détermination de la texture et des caractéristiques microstructurales. La morphologie des films a été caractérisée par microscopie électronique à balayage. L'étude a montré que la concentration de la solution de précurseur et la pression totale ont un effet majeur sur la morphologie des films et leur texture. Les films déposés étaient actifs électrochimiquement, montrant un comportement en charge et décharge attendu et une stabilité raisonnable durant les études en voltamétrie cycliques.

Etude de dégradation sur une électrode de $LiCoO_2$ modèle

Les propriétés des couches minces de $LiCoO_2$ dans le massif et en surface ont été étudiées avant et après électrochimie. Le cyclage galvanostatique a montré une importante diminution de la capacité après le premier cycle ce qui a été relié à la faible cristallisation induite par les changements structuraux favorisés par le cyclage électrochimique. Cette diminution significative n'est pas observée pour des couches minces bien cristallisées. La spectroscopie d'impédance électrochimique a de plus montré l'apparition d'une résistance associée à la formation d'une couche d'interface.

De plus, la microscopie électronique à balayage a montré que les couches déposées sont polycristallines avec des tailles de particules de 30 nm de moyenne. A part un lissage des particules, aucun changement majeur sur la morphologie n'a été observé après cyclage.

Le nettoyage et le trempage du matériau d'électrode dans l'électrolyte et dans le solvant a montré que les réactions de surfaces commencent des le premier contact. La formation d'une couche de surface par ce procédé provient du solvant pour les composés organiques et du sel pour les composés inorganiques. En XPS, ceci est montré par l'apparition de l'ion métallique Co^{2+} en surface après trempage et après électrochimie.

Un composant principal de la solution d'électrolyte, $LiPF_6$, a un effet critique du au fait qu'il peut se décomposer et former HF, réagissant avec les carbonates et formant du LiF en surface. Etant donné la grande quantité de LiF, une importante réactivité du $LiCoO_2$ avec les espèces décomposées a été observée. La couche de surface restante était principalement composée d'espèces organiques et quelques composé inorganiques. Les composés carbonés trouvés correspondent aux réactions provenant du solvant EC tandis que les sels de $LiPF_6$ forment les composés LiF et autres Li_xPF_y, ces derniers en minorité. La chimie de surface de la couche formée sur $LiCoO_2$ après cyclage est principalement liée aux espèces décomposées du sel de l'électrolyte provenant des espèces carbonatées et fluorées. Tremper les électrodes pour un temps court a résulté au dépôt d'une couche de surface sur le matériau actif, composé d'espèces organiques liées au solvant. Au contraire, le cyclage électrochimique favorise la formation d'espèces inorganiques liées au sel en surface de la cathode. Quand les échantillons sont trempés, nous avons observés une plus grande quantité d'espèces organiques qu'après cyclage électrochimiques. Ceci est mis en évidence par l'estimation des espèces contenant du carbone pour chaque échantillon, autour de 14% pour les échantillons trempés et 9% après cyclage. Finalement, le sel de l'électrolyte a montré une décomposition et une réactivité générant des espèces intermédiaires favorisant la polymérisation du solvant en présence d'eau et la formation de produits additionnels.

Couche de surface artificielle pour la cathode de $LiCoO_2$

Des couches de surface artificielles ont été déposées sur $LiCoO_2$ par pulvérisation rf. Les couches minces de ZrO_2 et LiPON utilisé comme traitement de surface ont eu un effet mineur sur la morphologie du film de départ et sa structure cristalline. Le mécanisme de protection et l'amélioration de la capacité de rétention pour les premiers cycles, observés pour les couches minces de $LiCoO_2$ avec traitement de surface, a été relié à deux facteurs principaux ; i) la création d'une barrière physique qui isole le matériau de cathode de l'électrolyte, et ii) formation d'une couche de surface par réaction chimiques entre la couche de surface artificiel et l'électrolyte. Une analyse XPS de l'interface a montré comment la nature de chaque couche était différente dans chaque cas après cyclage galvanostatique. La couche de surface artificielle résultante formée a partir du traitement de surface ZrO_2 présente principalement des espèces inorganiques, tandis que la cathode recouverte de LiPON présente une nature organique. La couche de surface finale après cyclage électrochimique recouvert du film de ZrO_2 ressemble à celle du $LiCoO_2$ sans traitement.

Etude structural des couches minces de LiPON

La composition et les propriétés du LiPON déposé avec différentes conditions ont été étudiées systématiquement. La stabilité chimique des oxydes de phosphore lithiés a été améliorée avec l'incorporation d'azote tout en créant une structure oxynitrure.

La composition des films de verre de phosphate avec la pulvérisation rf a montré être grandement influencé par le ratio de gaz employé. La plus grande variation a été observé pour les quantités les plus faibles de N_2 dans le mélange de gaz. Les spectres IR montrent d'importantes différences pour l'ordre à courte distance pour les films avec une quantité similaire de lithium.

Les films d'oxynitrure de phosphore lithiés déposé ici présentent une structure vitreuse avec principalement des unités ortho et pyro-phosphate avec des faibles quantités de courtes chaines metaphosphate.

L'insertion d'azote favorise la stabilité du lithium en donnant un environnement d'énergie potentielle plus faible, comme mise en évidence par les résultats d'IR lointains.

Les recuits à 250°C ont montrés des effets étendus sur le réseau vitreux, expliqués par la diminution des unités orthophosphates et l'augmentation des unités ponteuses. De plus, des changements de coordination dans l'environnement autour des atomes de Li dus aux charges négatives délocalisées des liaisons doubles de l'azote -N= ont été également observés. La conduction ionique a été augmentée par l'amélioration du transport des ions Li étant donné la réduction de la composante électrostatique de l'énergie d'activation.

Le LIPON a la particularité d'avoir des éléments avec une coordination spécifique qui favorise la formation de structures avec stabilité chimique et une grande mobilité ionique. Ces attributs son démontrés par les propriétés de conduction ioniques du a la coordination du phosphate, réticulation, covalence P-N et l'habilité à délocaliser les charges et déclencher la mobilité du a la coordination du phosphate, réticulation, covalence P-N et l'habilité à délocaliser les charges et déclencher la mobilité du lithium.

Bibliography

[1] M. M. Thackeray, C. Wolverton, and E. D. Isaacs, “Electrical energy storage for transportation—approaching the limits of, and going beyond, lithium-ion batteries,” *Energy & Environmental Science*, vol. 5, no. 7, pp. 7854–7863, 2012.

[2] M. S. Islam and C. A. Fisher, “Lithium and sodium battery cathode materials: Computational insights into voltage, diffusion and nanostructural properties,” *Chemical Society Reviews*, vol. 43, no. 1, pp. 185–204, 2014.

[3] N. Nitta, F. Wu, J. T. Lee, and G. Yushin, “Li-ion battery materials: Present and future,” *Materials Today*, vol. 18, no. 5, pp. 252–264, 2015.

[4] D. Aurbach, B. Markovsky, M. Levi, E. Levi, A. Schechter, M. Moshkovich, and Y. Cohen, “New insights into the interactions between electrode materials and electrolyte solutions for advanced nonaqueous batteries,” *Journal of power sources*, vol. 81, pp. 95–111, 1999.

[5] K. Edström, T. Gustafsson, and J. O. Thomas, “The cathode–electrolyte interface in the Li-ion battery,” *Electrochimica Acta*, vol. 50, no. 2, pp. 397–403, 2004.

[6] A. Thißen, D. Ensling, M. Liberatore, Q.-H. Wu, F. F. Madrigal, M. Bhuvaneswari, R. Hunger, and W. Jaegermann, “Experimental routes to in situ characterization of the electronic structure and chemical composition of cathode materials for lithium ion batteries during lithium intercalation and deintercalation using photoelectron spectroscopy and related techniques,” *Ionics*, vol. 15, no. 4, pp. 393–403, 2009.

[7] G. Cherkashinin, K. Nikolowski, H. Ehrenberg, S. Jacke, L. Dimesso, and W. Jaegermann, “The stability of the SEI layer, surface composition and the oxidation state of transition metals at the electrolyte–cathode interface impacted by the electrochemical cycling: X-ray photoelectron spectroscopy investigation,” *Physical Chemistry Chemical Physics*, vol. 14, no. 35, pp. 12321–12331, 2012.

[8] R. Dedryvère, H. Martinez, S. Leroy, D. Lemordant, F. Bonhomme, P. Biensan, and D. Gonbeau, “Surface film formation on electrodes in a $LiCoO_2$/graphite cell: A step by step XPS study,” *Journal of Power Sources*, vol. 174, no. 2, pp. 462–468, 2007.

[9] J. Vetter, P. Novák, M. Wagner, C. Veit, K.-C. Möller, J. Besenhard, M. Winter, M. Wohlfahrt-Mehrens, C. Vogler, and A. Hammouche, “Ageing mechanisms in lithium-ion batteries,” *Journal of power sources*, vol. 147, no. 1, pp. 269–281, 2005.

[10] M. Wohlfahrt-Mehrens, C. Vogler, and J. Garche, “Aging mechanisms of lithium cathode materials,” *Journal of power sources*, vol. 127, no. 1, pp. 58–64, 2004.

[11] D. Aurbach, “Review of selected electrode–solution interactions which determine the performance of Li and Li ion batteries,” *Journal of Power Sources*, vol. 89, no. 2, pp. 206–218, 2000.

[12] Y. Takanashi, Y. Orikasa, M. Mogi, M. Oishi, H. Murayama, K. Sato, H. Yamashige, D. Takamatsu, T. Fujimoto, H. Tanida, *et al.*, "Thickness estimation of interface films formed on $Li_{1-x}CoO_2$ electrodes by hard X-ray photoelectron spectroscopy," *Journal of Power Sources*, vol. 196, no. 24, pp. 10679–10685, 2011.

[13] D. Takamatsu, T. Nakatsutsumi, S. Mori, Y. Orikasa, M. Mogi, H. Yamashige, K. Sato, T. Fujimoto, Y. Takanashi, H. Murayama, *et al.*, "Nanoscale observation of the electronic and local structures of $LiCoO_2$ thin film electrode by depth-resolved X-ray absorption spectroscopy," *The Journal of Physical Chemistry Letters*, vol. 2, no. 20, pp. 2511–2514, 2011.

[14] L. Dahéron, R. Dedryvere, H. Martinez, M. Ménétrier, C. Denage, C. Delmas, and D. Gonbeau, "Electron transfer mechanisms upon lithium deintercalation from $LiCoO_2$ to CoO_2 investigated by XPS," *Chemistry of Materials*, vol. 20, no. 2, pp. 583–590, 2007.

[15] D. Kolb, "Surface science aspects of interfacial electrochemistry," *Journal of Vacuum Science & Technology A*, vol. 4, no. 3, pp. 1294–1301, 1986.

[16] D. M. Kolb, "Electrochemical surface science: past, present and future," *Journal of Solid State Electrochemistry*, vol. 15, no. 7-8, pp. 1391–1399, 2011.

[17] T. Mayer, M. Lebedev, R. Hunger, and W. Jaegermann, "Elementary processes at semiconductor/electrolyte interfaces: perspectives and limits of electron spectroscopy," *Applied surface science*, vol. 252, no. 1, pp. 31–42, 2005.

[18] W. Jaegermann, "The semiconductor/electrolyte interface: a surface science approach," *Modern aspects of electrochemistry*, vol. 30, pp. 1–186, 1996.

[19] R. Hausbrand, D. Becker, and W. Jaegermann, "A surface science approach to cathode/electrolyte interfaces in Li-ion batteries: Contact properties, charge transfer and reactions," *Progress in Solid State Chemistry*, vol. 42, no. 4, pp. 175–183, 2014.

[20] D. Aurbach, B. Markovsky, A. Rodkin, E. Levi, Y. Cohen, H.-J. Kim, and M. Schmidt, "On the capacity fading of $LiCoO_2$ intercalation electrodes: The effect of cycling, storage, temperature, and surface film forming additives," *Electrochimica Acta*, vol. 47, no. 27, pp. 4291–4306, 2002.

[21] A. Chagnes and J. Swiatowska, *Electrolyte and solid-electrolyte interphase layer in lithium-ion batteries.* INTECH Open Access Publisher, 2012.

[22] M. Armand and J.-M. Tarascon, "Building better batteries," *Nature*, vol. 451, no. 7179, pp. 652–657, 2008.

[23] L. Fu, H. Liu, C. Li, Y. Wu, E. Rahm, R. Holze, and H. Wu, "Surface modifications of electrode materials for lithium ion batteries," *Solid State Sciences*, vol. 8, no. 2, pp. 113–128, 2006.

[24] J. Song, S. Jacke, D. Becker, R. Hausbrand, and W. Jaegermann, "Stabilization of thin film $LiCoO_2$ electrode by LiPON coating," *Electrochemical and Solid-State Letters*, vol. 14, no. 2, pp. A11–A13, 2011.

[25] S. Shi, J. Tu, Y. Tang, Y. Zhang, X. Liu, X. Wang, and C. Gu, "Enhanced electrochemical performance of LiF-modified $LiNi_{1/3}Co_{1/3}Mn_{1/3}O_2$ cathode materials for Li-ion batteries," *Journal of Power Sources*, vol. 225, pp. 338–346, 2013.

[26] Y. J. Kim, J. Cho, T.-J. Kim, and B. Park, "Suppression of cobalt dissolution from the $LiCoO_2$ cathodes with various metal-oxide coatings," *Journal of The Electrochemical Society*, vol. 150, no. 12, pp. A1723–A1725, 2003.

[27] M. Thackeray, C. Johnson, J.-S. Kim, K. Lauzze, J. Vaughey, N. Dietz, D. Abraham, S. Hackney, W. Zeltner, and M. Anderson, "ZrO_2-and Li_2ZrO_3-stabilized spinel and layered electrodes for lithium batteries," *Electrochemistry communications*, vol. 5, no. 9, pp. 752–758, 2003.

[28] D. Takamatsu, S. Mori, Y. Orikasa, T. Nakatsutsumi, Y. Koyama, H. Tanida, H. Arai, Y. Uchimoto, and Z. Ogumi, "Effects of ZrO_2 coating on $LiCoO_2$ thin-film electrode studied by in situ X-ray absorption spectroscopy," *Journal of The Electrochemical Society*, vol. 160, no. 5, pp. A3054–A3060, 2013.

[29] G. Liu, H. Kuo, R. Liu, C. Shen, D. Shy, X. Xing, and J. Chen, "Study of electrochemical properties of coating ZrO_2 on $LiCoO_2$," *Journal of Alloys and Compounds*, vol. 496, no. 1, pp. 512–516, 2010.

[30] Y. Huang, J. Chen, J. Ni, H. Zhou, and X. Zhang, "A modified ZrO_2-coating process to improve electrochemical performance of $Li(Ni_{1/3}Co_{1/3}Mn_{1/3})O_2$," *Journal of Power Sources*, vol. 188, no. 2, pp. 538–545, 2009.

[31] J. Bates, N. Dudney, G. Gruzalski, R. Zuhr, A. Choudhury, C. Luck, and J. Robertson, "Fabrication and characterization of amorphous lithium electrolyte thin films and rechargeable thin-film batteries," *Journal of Power Sources*, vol. 43, no. 1, pp. 103–110, 1993.

[32] N. J. Dudney, "Thin film micro-batteries," *The Electrochemical Society Interface*, vol. 17, no. 3, p. 44, 2008.

[33] A. Schwöbel, R. Hausbrand, and W. Jaegermann, "Interface reactions between LiPON and lithium studied by in-situ X-ray photoemission," *Solid State Ionics*, vol. 273, pp. 51–54, 2015.

[34] A. Schwöbel, R. Precht, M. Motzko, M. A. Carrillo Solano, W. Calvet, R. Hausbrand, and W. Jaegermann, "Determination of the valence band structure of an alkali phosphorus oxynitride glass: A synchrotron XPS study on LiPON," *Applied Surface Science*, vol. 321, pp. 55–60, 2014.

[35] N. J. Dudney, "Addition of a thin-film inorganic solid electrolyte (Lipon) as a protective film in lithium batteries with a liquid electrolyte," *Journal of Power Sources*, vol. 89, no. 2, pp. 176–179, 2000.

[36] K.-F. Chiu, C.-L. Chen, B.-S. Chen, and H.-J. Leu, "Modification of electrolyte/cathode interfaces by solid-state electrolyte thin films," *ECS Transactions*, vol. 35, no. 32, pp. 67–75, 2011.

[37] S. Tintignac, *Etude structurale et électrochimique de films de $LiCoO_2$ préparés par pulvérisation cathodique: application aux microaccumulateurs tout solide.* PhD thesis, Université Paris-Est, 2008.

[38] R. Younesi, M. Hahlin, F. Björefors, P. Johansson, and K. Edström, "Li–O_2 battery degradation by lithium peroxide (Li_2O_2): a model study," *Chemistry of Materials*, vol. 25, no. 1, pp. 77–84, 2012.

[39] R. Dedryvère, S. Laruelle, S. Grugeon, L. Gireaud, J.-M. Tarascon, and D. Gonbeau, "XPS identification of the organic and inorganic components of the electrode/electrolyte interface formed on a metallic cathode," *Journal of The Electrochemical Society*, vol. 152, no. 4, pp. A689–A696, 2005.

[40] K. Yamamoto, T. Minato, S. Mori, D. Takamatsu, Y. Orikasa, H. Tanida, K. Nakanishi, H. Murayama, T. Masese, T. Mori, *et al.*, "Improved cyclic performance of lithium-ion batteries: An investigation of cathode/electrolyte interface via in situ total-reflection fluorescence X-ray absorption spectroscopy," *The Journal of Physical Chemistry C*, vol. 118, no. 18, pp. 9538–9543, 2014.

[41] D. Ensling, A. Thissen, and W. Jaegermann, "On the formation of lithium oxides and carbonates on Li metal electrodes in comparison to $LiCoO_2$ surface phases investigated by photoelectron spectroscopy," *Applied Surface Science*, vol. 255, no. 5, pp. 2517–2523, 2008.

[42] B. Fleutot, B. Pecquenard, H. Martinez, M. Letellier, and A. Levasseur, "Investigation of the local structure of LiPON thin films to better understand the role of nitrogen on their performance," *Solid State Ionics*, vol. 186, no. 1, pp. 29–36, 2011.

[43] B. Fleutot, *Amélioration des performances des microbatteries au lithium: corrélation entre la structure locale et la conductivité ionique d'électrolytes solides amorphes*. PhD thesis, Université de Bordeaux, 2010.

[44] Y. Hamon, *Nitruration de verres conducteurs ioniques en couches minces*. PhD thesis, Université Sciences et Technologies-Bordeaux I, 2004.

[45] Y. Hamon, A. Douard, F. Sabary, C. Marcel, P. Vinatier, B. Pecquenard, and A. Levasseur, "Influence of sputtering conditions on ionic conductivity of LiPON thin films," *Solid State Ionics*, vol. 177, no. 3, pp. 257–261, 2006.

[46] C. Hamann, A. Hamnett, and W. Vielstich, *Electrochemistry*. Weinheim: Wiley-VCH Pub, 2007.

[47] J. Newman and K. E. Thomas-Alyea, *Electrochemical systems*. John Wiley & Sons, 2012.

[48] A. J. Bard, L. R. Faulkner, *et al.*, "Electrochemical methods. fundamentals and applications," *Electrochemical Methods, 2nd ed.; Wiley: New York*, 2001.

[49] C. Julien, G. Nazri, and W. Plieth, "Solid state batteries, materials design and optimization," *Crystal Research and Technology*, vol. 30, no. 3, pp. 398–398, 1995.

[50] J.-M. Tarascon and M. Armand, "Issues and challenges facing rechargeable lithium batteries," *Nature*, vol. 414, no. 6861, pp. 359–367, 2001.

[51] M. Winter, J. O. Besenhard, M. E. Spahr, and P. Novak, "Insertion electrode materials for rechargeable lithium batteries," *Advanced materials*, vol. 10, no. 10, pp. 725–763, 1998.

[52] M. Winter and R. J. Brodd, "What are batteries, fuel cells, and supercapacitors?," *Chemical reviews*, vol. 104, no. 10, pp. 4245–4270, 2004.

[53] B. Scrosati and J. Garche, "Lithium batteries: Status, prospects and future," *Journal of Power Sources*, vol. 195, no. 9, pp. 2419–2430, 2010.

[54] D. Linden, "Handbook of batteries and fuel cells," *New York, McGraw-Hill Book Co., 1984, 1075 p. No individual items are abstracted in this volume.*, vol. 1, 1984.

[55] J. Collins, G. Gourdin, M. Foster, and D. Qu, "Carbon surface functionalities and SEI formation during Li intercalation," *Carbon*, vol. 92, pp. 193–244, 2015.

[56] P. H. Notten, F. Roozeboom, R. A. Niessen, and L. Baggetto, "3-D integrated all-solid-state rechargeable batteries," *Advanced Materials*, vol. 19, no. 24, pp. 4564–4567, 2007.

[57] D. Guyomard and J. Tarascon, "Li metal-free rechargeable $LiMn_2O_4$/carbon cells: Their understanding and optimization," *Journal of The Electrochemical Society*, vol. 139, no. 4, pp. 937–948, 1992.

[58] M. S. Whittingham, "Lithium batteries and cathode materials," *Chemical reviews*, vol. 104, no. 10, pp. 4271–4302, 2004.

[59] R. Koksbang, J. Barker, H. Shi, and M. Saidi, "Cathode materials for lithium rocking chair batteries," *Solid state ionics*, vol. 84, no. 1, pp. 1–21, 1996.

[60] L. Sebastian and J. Gopalakrishnan, "Lithium ion mobility in metal oxides: A materials chemistry perspective," *Journal of Materials Chemistry*, vol. 13, no. 3, pp. 433–441, 2003.

[61] T. Ohzuku and R. J. Brodd, "An overview of positive-electrode materials for advanced lithium-ion batteries," *Journal of Power Sources*, vol. 174, no. 2, pp. 449–456, 2007.

[62] J. B. Bates, N. J. Dudney, B. J. Neudecker, F. X. Hart, H. P. Jun, and S. A. Hackney, "Preferred orientation of polycrystalline $LiCoO_2$ films," *Journal of The Electrochemical Society*, vol. 147, no. 1, pp. 59–70, 2000.

[63] Y. R. Kosuri, T. R. Penki, M. Nookala, P. Morgen, and M. R. Gowravaram, “Investigations on sputter deposited $LiCoO_2$ thin films from powder target,” *Advanced Materials Letters*, vol. 4, no. 8, pp. 615–620, 2013.

[64] J. F. Oudenhoven, L. Baggetto, and P. H. Notten, “All-solid-state lithium-ion microbatteries: A review of various three-dimensional concepts,” *Advanced Energy Materials*, vol. 1, no. 1, pp. 10–33, 2011.

[65] H. Katsui, Y. Yamashita, R. Tu, and T. Goto, “Preparation of Li–Co–O film by metal organic chemical vapor deposition,” *Journal of the Ceramic Society of Japan*, vol. 121, no. 1413, pp. 406–410, 2013.

[66] S.-I. Cho and S.-G. Yoon, “Characterization of $LiCoO_2$ thin film cathodes deposited by liquid-delivery metallorganic chemical vapor deposition for rechargeable lithium batteries,” *Journal of The Electrochemical Society*, vol. 149, no. 12, pp. A1584–A1588, 2002.

[67] B. Neudecker, R. Zuhr, B. Kwak, J. Bates, and J. Robertson, “Lithium manganese nickel oxides $Li_x(Mn_yNi_{1-y})_{2\text{-}x}O_2$ I. Synthesis and characterization of thin films and bulk phases,” *Journal of the Electrochemical Society*, vol. 145, no. 12, pp. 4148–4159, 1998.

[68] J. Schwenzel, V. Thangadurai, and W. Weppner, “Investigation of thin film all-solid-state lithium ion battery materials,” *Ionics*, vol. 9, no. 5-6, pp. 348–356, 2003.

[69] C. Jacob, T. Lynch, A. Chen, J. Jian, and H. Wang, “Highly textured $Li(Ni_{0.5}Mn_{0.3}Co_{0.2})O_2$ thin films on stainless steel as cathode for lithium-ion battery,” *Journal of Power Sources*, vol. 241, pp. 410 – 414, 2013.

[70] P. Bouwman, B. Boukamp, H. Bouwmeester, H. Wondergem, and P. Notten, “Structural analysis of submicrometer $LiCoO_2$ films,” *Journal of The Electrochemical Society*, vol. 148, no. 4, pp. A311–A317, 2001.

[71] M.-K. Kim, K.-S. Park, J.-T. Son, J.-G. Kim, H.-T. Chung, and H.-G. Kim, “The electrochemical properties of thin-film $LiCoO_2$ cathode prepared by sol–gel process,” *Solid state ionics*, vol. 152, pp. 267–272, 2002.

[72] L. Baggetto, R. A. Niessen, F. Roozeboom, and P. H. Notten, “High energy density all-solid-state batteries: A challenging concept towards 3D integration,” *Advanced Functional Materials*, vol. 18, no. 7, pp. 1057–1066, 2008.

[73] T. Ohzuku and A. Ueda, “Solid-state redox reactions of $LiCoO_2$ (R-3m) for 4 volt secondary lithium cells,” *Journal of The Electrochemical Society*, vol. 141, no. 11, pp. 2972–2977, 1994.

[74] J. Cho, Y. J. Kim, T.-J. Kim, and B. Park, “Enhanced structural stability of o-$LiMnO_2$ by sol-gel coating of Al_2O_3,” *Chemistry of Materials*, vol. 13, no. 1, pp. 18–20, 2001.

[75] H. Xia, Y. Meng, L. Lu, and G. Ceder, “Electrochemical behavior and Li diffusion study of $LiCoO_2$ thin film electrode prepared by PLD,” *J. Power Sources*, vol. 159, pp. 1422–1427, 2006.

[76] G.-H. Kim, A. Pesaran, and R. Spotnitz, “A three-dimensional thermal abuse model for lithium-ion cells,” *Journal of Power Sources*, vol. 170, no. 2, pp. 476–489, 2007.

[77] M. K. Gulbinska, *Lithium-ion Battery Materials and Engineering: Current Topics and Problems from the Manufacturing Perspective*. Springer, 2014.

[78] C. Delmas, M. Ménétrier, L. Croguennec, I. Saadoune, A. Rougier, C. Pouillerie, G. Prado, M. Grüne, and L. Fournes, “An overview of the $Li(Ni,M)O_2$ systems: Syntheses, structures and properties,” *Electrochimica Acta*, vol. 45, no. 1, pp. 243–253, 1999.

[79] I. Nakai, K. Takahashi, Y. Shiraishi, T. Nakagome, F. Izumi, Y. Ishii, F. Nishikawa, and T. Konishi, "X-ray absorption fine structure and neutron diffraction analyses of de-intercalation behavior in the $LiCoO_2$ and $LiNiO_2$ systems," *Journal of power sources*, vol. 68, no. 2, pp. 536–539, 1997.

[80] J. Paulsen, C. Thomas, and J. R. Dahn, "Layered Li-Mn-Oxide with the O_2 structure: A cathode material for Li-ion cells which does not convert to spinel," *Journal of The Electrochemical Society*, vol. 146, no. 10, pp. 3560–3565, 1999.

[81] J.-J. Ding, Q. Sun, and Z.-W. Fu, "Layered $Li(Ni_{1/4}Mn_{1/2}Co_{1/3})O_2$ as cathode material for all-solid-state thin-film rechargeable lithium-ion batteries," *Electrochemical and Solid-State Letters*, vol. 13, no. 8, pp. A105–A108, 2010.

[82] J. B. Goodenough and Y. Kim, "Challenges for rechargeable Li batteries†," *Chemistry of Materials*, vol. 22, no. 3, pp. 587–603, 2010.

[83] J. Wilcox, S. Patoux, and M. Doeff, "Structure and electrochemistry of $LiNi_{1/3}Co_{1/3\text{-}y}M_yMn_{1/3}O_2$ (M= Ti, Al, Fe) positive electrode materials," *Journal of The Electrochemical Society*, vol. 156, no. 3, pp. A192–A198, 2009.

[84] J.-M. Kim and H.-T. Chung, "The first cycle characteristics of $LiCo_{1/3}Ni_{1/3}Mn_{1/3}O_2$ charged up to 4.7 V," *Electrochimica Acta*, vol. 49, no. 6, pp. 937–944, 2004.

[85] X. Hou and K.-L. Choy, "Processing and applications of aerosol-assisted chemical vapor deposition," *Chemical Vapor Deposition*, vol. 12, no. 10, pp. 583–596, 2006.

[86] P. O'Brien, N. L. Pickett, and D. J. Otway, "Developments in CVD delivery systems: A chemist's perspective on the chemical and physical interactions between precursors," *Chemical Vapor Deposition*, vol. 8, no. 6, pp. 237–249, 2002.

[87] M. I. Ionescu, Y. Zhang, R. Li, X. Sun, H. Abou-Rachid, and L.-S. Lussier, "Hydrogen-free spray pyrolysis chemical vapor deposition method for the carbon nanotube growth: Parametric studies," *Applied Surface Science*, vol. 257, no. 15, pp. 6843 – 6849, 2011.

[88] P. S. Patil, "Versatility of chemical spray pyrolysis technique," *Materials Chemistry and physics*, vol. 59, no. 3, pp. 185–198, 1999.

[89] A. J. Darbandi and H. Hahn, "Nanoparticulate cathode thin films with high electrochemical activity for low temperature SOFC applications," *Solid State Ionics*, vol. 180, no. 26, pp. 1379–1387, 2009.

[90] R. Djenadic, M. Botros, C. Benel, O. Clemens, S. Indris, A. Choudhary, T. Bergfeldt, and H. Hahn, "Nebulized spray pyrolysis of Al-doped $Li_7La_3Zr_2O_{12}$ solid electrolyte for battery applications," *Solid State Ionics*, vol. 263, pp. 49–56, 2014.

[91] C. Benel, A. J. Darbandi, R. Djenadic, A. Evans, R. Tölke, M. Prestat, and H. Hahn, "Cathodes for thin-film solid oxide fuel cells," *Journal of Power Sources*, vol. 229, pp. 258–264, 2013.

[92] C. Chen, E. Kelder, M. Jak, and J. Schoonman, "Electrostatic spray deposition of thin layers of cathode materials for lithium battery," *Solid State Ionics*, vol. 86, pp. 1301–1306, 1996.

[93] F. Iskandar, "Nanoparticle processing for optical applications – A review," *Advanced Powder Technology*, vol. 20, no. 4, pp. 283–292, 2009.

[94] C. Chen, E. Kelder, and J. Schoonman, "Electrode and solid electrolyte thin films for secondary lithium-ion batteries," *Journal of power sources*, vol. 68, no. 2, pp. 377–380, 1997.

[95] C. Chen, E. Kelder, P. van der Put, and J. Schoonman, "Morphology control of thin $LiCoO_2$ films fabricated using the electrostatic spray deposition (ESD) technique," *Journal of material chemistry*, vol. 6, no. 5, pp. 765–771, 1996.

[96] J. Kalhoff, G. G. Eshetu, D. Bresser, and S. Passerini, “Safer electrolytes for lithium-ion batteries: State of the art and perspectives,” *ChemSusChem*, 2015.

[97] K. Xu, “Nonaqueous liquid electrolytes for lithium-based rechargeable batteries,” *Chemical reviews*, vol. 104, no. 10, pp. 4303–4418, 2004.

[98] J. O. Besenhard, *Handbook of battery materials*. John Wiley & Sons, 2008.

[99] M. Nazri, “Liquid electrolytes: Some theoretical and practical aspects,” in *Lithium batteries*, pp. 509–529, Springer, 2003.

[100] M. Park, X. Zhang, M. Chung, G. B. Less, and A. M. Sastry, “A review of conduction phenomena in Li-ion batteries,” *Journal of Power Sources*, vol. 195, no. 24, pp. 7904–7929, 2010.

[101] L. Suo, Y.-S. Hu, H. Li, M. Armand, and L. Chen, “A new class of solvent-in-salt electrolyte for high-energy rechargeable metallic lithium batteries,” *Nature communications*, vol. 4, p. 1481, 2013.

[102] K. Takada, “Progress and prospective of solid-state lithium batteries,” *Acta Materialia*, vol. 61, no. 3, pp. 759–770, 2013.

[103] V. Thangadurai and W. Weppner, “Recent progress in solid oxide and lithium ion conducting electrolytes research,” *Ionics*, vol. 12, no. 1, pp. 81–92, 2006.

[104] V. Thangadurai, H. Kaack, and W. J. Weppner, “Novel fast lithium ion conduction in garnet-type $Li_5La_3M_2O_{12}$ (M= Nb, Ta),” *Journal of the American Ceramic Society*, vol. 86, no. 3, pp. 437–440, 2003.

[105] E. Quartarone and P. Mustarelli, “Electrolytes for solid-state lithium rechargeable batteries: recent advances and perspectives,” *Chemical Society Reviews*, vol. 40, no. 5, pp. 2525–2540, 2011.

[106] M. Murayama, R. Kanno, M. Irie, S. Ito, T. Hata, N. Sonoyama, and Y. Kawamoto, “Synthesis of new lithium ionic conductor thio-LISICON—lithium silicon sulfides system,” *Journal of Solid State Chemistry*, vol. 168, no. 1, pp. 140–148, 2002.

[107] M. R. Palacin, “Recent advances in rechargeable battery materials: A chemist’s perspective,” *Chemical Society Reviews*, vol. 38, no. 9, pp. 2565–2575, 2009.

[108] W. Holand and G. H. Beall, *Glass ceramic technology*. John Wiley & Sons, 2012.

[109] R. K. Brow, “Review: The structure of simple phosphate glasses,” *Journal of Non-Crystalline Solids*, vol. 263, pp. 1–28, 2000.

[110] R. Brow, L. Kovacic, and R. Loehman, “Novel glass sealing technologies,” *Ceram. Trans.*, vol. 70, pp. 177–187, 1995.

[111] D. Day, Z. Wu, C. Ray, and P. Hrma, “Chemically durable iron phosphate glass wasteforms,” *Journal of non-crystalline solids*, vol. 241, no. 1, pp. 1–12, 1998.

[112] C. Dayanand, G. Bhikshamaiah, V. J. Tyagaraju, M. Salagram, and A. K. Murthy, “Structural investigations of phosphate glasses: A detailed infrared study of the x(PbO)-(1-x) P_2O_5 vitreous system,” *Journal of materials science*, vol. 31, no. 8, pp. 1945–1967, 1996.

[113] J. Vogel, P. Wange, and P. Hartmann, “Effect of composition changes on the structure and properties of phosphate glasses in the pyrophosphate region,” *Glass science and technology*, vol. 70, no. 1, pp. 23–27, 1997.

[114] M. R. Reidmeyer, M. Rajaram, and D. E. Day, “Preparation of phosphorus oxynitride glasses,” *Journal of non-crystalline solids*, vol. 85, no. 1, pp. 186–203, 1986.

[115] J. B. Bates, N. J. Dudney, C. F. Luck, B. C. Sales, R. A. Zuhr, and J. D. Robertson, “Deposition and characterization of Li_2O–SiO_2–P_2O_5 thin films,” *Journal of the American Ceramic Society*, vol. 76, no. 4, pp. 929–943, 1993.

[116] J. Fu, “Fast Li^+ ion conduction in $Li_2O-(Al_2O_3,Ga_2O_3)-TiO_2-P_2O_5$ glass-ceramics,” *Journal of materials science*, vol. 33, no. 6, pp. 1549–1553, 1998.

[117] Y.-N. Xu, W. Ching, and Y.-M. Chiang, “Comparative studies of the electronic structure of $LiFePO_4$, $FePO_4$, Li_3PO_4, $LiMnPO_4$, $LiCoPO_4$, and $LiNiPO_4$,” *Journal of applied physics*, vol. 95, pp. 6583–6585, 2004.

[118] F. Berkemeier, M. R. S. Abouzari, and G. Schmitz, “Thickness-dependent dc conductivity of lithium borate glasses,” *Physical review B*, vol. 76, no. 2, p. 024205, 2007.

[119] T. Minami, “Fast ion conducting glasses,” *Journal of Non-Crystalline Solids*, vol. 73, no. 1, pp. 273–284, 1985.

[120] M. D. Ingram and C. T. Imrie, “New insights from variable-temperature and variable-pressure studies into coupling and decoupling processes for ion transport in polymer electrolytes and glasses,” *Solid State Ionics*, vol. 196, no. 1, pp. 9–17, 2011.

[121] R. E. Loehman, “Oxynitride glasses,” *MRS Bulletin*, vol. 12, no. 05, pp. 26–31, 1987.

[122] R. E. Loehman, “Oxynitride glasses,” *Journal of Non-Crystalline Solids*, vol. 42, no. 1, pp. 433–445, 1980.

[123] R. Marchand, D. Agliz, L. Boukbir, and A. Quemerais, “Characterization of nitrogen containing phosphate glasses by X-ray photoelectron spectroscopy,” *Journal of non-crystalline solids*, vol. 103, no. 1, pp. 35–44, 1988.

[124] F. Muñoz, L. Pascual, A. Durán, J. Rocherullé, and R. Marchand, “Alkali and alkali–lead oxynitride phosphate glasses: a comparative structural study by NMR and XPS,” *Comptes Rendus Chimie*, vol. 5, no. 11, pp. 731–738, 2002.

[125] E. Kamitsos, C. Varsamis, and A. Vegiri, “Spectroscopic studies of mobile cations in glass,” *Proc. Int. Cong. Glass*, vol. 1, pp. 234–246, 2001.

[126] E. Kamitsos and G. D. Chryssikos, “Alkali sites in glass,” *Solid State Ionics*, vol. 105, no. 1, pp. 75–85, 1998.

[127] J. Bates, N. Dudney, G. Gruzalski, R. Zuhr, A. Choudhury, C. Luck, and J. Robertson, “Electrical properties of amorphous lithium electrolyte thin films,” *Solid state ionics*, vol. 53, pp. 647–654, 1992.

[128] X. Yu, J. Bates, G. Jellison, and F. Hart, “A stable thin-film lithium electrolyte: Lithium phosphorus oxynitride,” *Journal of the electrochemical society*, vol. 144, no. 2, pp. 524–532, 1997.

[129] C. Choi, W. Cho, B. Cho, H. Kim, Y. Yoon, and Y. Tak, “Radio-frequency magnetron sputtering power effect on the ionic conductivities of LiPON films,” *Electrochemical and solid-state letters*, vol. 5, no. 1, pp. A14–A17, 2002.

[130] N.-S. Roh, S.-D. Lee, and H.-S. Kwon, “Effects of deposition condition on the ionic conductivity and structure of amorphous lithium phosphorus oxynitrate thin film,” *Scripta materialia*, vol. 42, no. 1, pp. 43–49, 1999.

[131] C. Nimisha, K. Y. Rao, G. Venkatesh, G. M. Rao, and N. Munichandraiah, “Sputter deposited LiPON thin films from powder target as electrolyte for thin film battery applications,” *Thin Solid Films*, vol. 519, no. 10, pp. 3401–3406, 2011.

[132] Z. Hu, D. Li, and K. Xie, "Influence of radio frequency power on structure and ionic conductivity of LiPON thin films," *Bulletin of Materials Science*, vol. 31, no. 4, pp. 681–686, 2008.

[133] H. Y. Park, S. C. Nam, Y. C. Lim, K. G. Choi, K. C. Lee, G. B. Park, S.-R. Lee, H. P. Kim, and S. B. Cho, "Effects of sputtering pressure on the characteristics of lithium ion conductive lithium phosphorous oxynitride thin film," *Journal of electroceramics*, vol. 17, no. 2-4, pp. 1023–1030, 2006.

[134] N. Suzuki, S. Shirai, N. Takahashi, T. Inaba, and T. Shiga, "A lithium phosphorous oxynitride (LiPON) film sputtered from unsintered Li_3PO_4 powder target," *Solid State Ionics*, vol. 191, no. 1, pp. 49–54, 2011.

[135] B. C. Bunker, D. R. Tallant, C. A. Balfe, R. J. Kirkpatrick, G. L. Turner, and M. R. Reidmeyer, "Structure of phosphorus oxynitride glasses," *Journal of the American Ceramic Society*, vol. 70, no. 9, pp. 675–681, 1987.

[136] M. Dussauze, E. I. Kamitsos, P. Johansson, A. Matic, C.-P. E. Varsamis, D. Cavagnat, P. Vinatier, and Y. Hamon, "Lithium ion conducting boron-oxynitride amorphous thin films: Synthesis and molecular structure by infrared spectroscopy and density functional theory modeling," *The Journal of Physical Chemistry C*, vol. 117, no. 14, pp. 7202–7213, 2013.

[137] M. R. Reidmeyer, D. E. Day, and R. K. Brow, "Phosphorus oxynitride glasses of variable sodium content," *Journal of non-crystalline solids*, vol. 177, pp. 208–215, 1994.

[138] E. I. Kamitsos, M. Dussauze, C.-P. E. Varsamis, P. Vinatier, and Y. Hamon, "Thin film amorphous electrolytes: Structure and composition by experimental and simulated infrared spectra," *The Journal of Physical Chemistry C*, vol. 111, no. 22, pp. 8111–8119, 2007.

[139] E. Peled, "The electrochemical behavior of alkali and alkaline earth metals in nonaqueous battery systems— the solid electrolyte interphase model," *Journal of The Electrochemical Society*, vol. 126, no. 12, pp. 2047–2051, 1979.

[140] D. Aurbach, K. Gamolsky, B. Markovsky, G. Salitra, Y. Gofer, U. Heider, R. Oesten, and M. Schmidt, "The study of surface phenomena related to electrochemical lithium intercalation into Li_xMO_y host materials (M = Ni, Mn)," *Journal of The Electrochemical Society*, vol. 147, no. 4, pp. 1322–1331, 2000.

[141] D. Aurbach, "Electrode–solution interactions in Li-ion batteries: A short summary and new insights," *Journal of power sources*, vol. 119, pp. 497–503, 2003.

[142] B. Markovsky, A. Rodkin, Y. Cohen, O. Palchik, E. Levi, D. Aurbach, H.-J. Kim, and M. Schmidt, "The study of capacity fading processes of Li-ion batteries: major factors that play a role," *Journal of power sources*, vol. 119, pp. 504–510, 2003.

[143] J. Cho, Y. J. Kim, T.-J. Kim, and B. Park, "Zero-strain intercalation cathode for rechargeable Li-ion cell," *Angewandte Chemie*, vol. 113, no. 18, pp. 3471–3473, 2001.

[144] C. Li, H. Zhang, L. Fu, H. Liu, Y. Wu, E. Rahm, R. Holze, and H. Wu, "Cathode materials modified by surface coating for lithium ion batteries," *Electrochimica Acta*, vol. 51, no. 19, pp. 3872–3883, 2006.

[145] Y.-K. Sun, J.-M. Han, S.-T. Myung, S.-W. Lee, and K. Amine, "Significant improvement of high voltage cycling behavior AlF_3-coated $LiCoO_2$ cathode," *Electrochemistry communications*, vol. 8, no. 5, pp. 821–826, 2006.

[146] J. Cho, Y. J. Kim, and B. Park, "Novel $LiCoO_2$ cathode material with Al_2O_3 coating for a Li-ion cell," *Chemistry of Materials*, vol. 12, no. 12, pp. 3788–3791, 2000.

[147] J.-S. Kim, C. Johnson, J. Vaughey, S. Hackney, K. Walz, W. Zeltner, M. Anderson, and M. Thackeray, "The electrochemical stability of spinel electrodes coated with ZrO_2, Al_2O_3, and SiO_2 from colloidal suspensions," *Journal of The Electrochemical Society*, vol. 151, no. 10, pp. A1755–A1761, 2004.

[148] E. Jeong, C. Hong, Y. Tak, S. C. Nam, and S. Cho, "Investigation of interfacial resistance between $LiCoO_2$ cathode and LiPON electrolyte in the thin film battery," *Journal of power sources*, vol. 159, no. 1, pp. 223–226, 2006.

[149] Z. Chen and J. Dahn, "Effect of a ZrO_2 coating on the structure and electrochemistry of Li_xCoO_2 when cycled to 4.5 V," *Electrochemical and solid-state letters*, vol. 5, no. 10, pp. A213–A216, 2002.

[150] D. M. Mattox, *Handbook of physical vapor deposition (PVD) processing.* William Andrew, 2010.

[151] J.-H. Park and T. Sudarshan, *Chemical vapor deposition*, vol. 2. ASM international, 2001.

[152] A. Klein, T. Mayer, A. Thissen, and W. Jaegermann, "Photoelectron spectroscopy in materials science and physical chemistry," *Bunsen-Magazin*, vol. 10, no. 4, pp. 124–139, 2008.

[153] J. F. Moulder, J. Chastain, and R. C. King, *Handbook of X-ray photoelectron spectroscopy: A reference book of standard spectra for identification and interpretation of XPS data.* Perkin-Elmer Eden Prairie, MN, 1992.

[154] P. Tarte, "Isomorphism and polymorphism of the compounds Li_3PO_4, Li_3AsO_4 and Li_3VO_4," *Journal of Inorganic and Nuclear Chemistry*, vol. 29, no. 4, pp. 915–923, 1967.

[155] Y. G. Kim, "Plasma-assisted directed vapor deposition for synthesizing lithium phosphorus oxynitride thin films," 2008.

[156] A. Thompson and D. Vaughan, "X-ray data booklet (center for X-ray optics and advanced light source)," *Lawrence Berkeley National Laboratory,*, 2001.

[157] J. A. Bearden and A. Burr, "Reevaluation of X-ray atomic energy levels," *Reviews of Modern Physics*, vol. 39, no. 1, p. 125, 1967.

[158] T. V. User's Manual, "Bruker AXS," *Karlsruhe, Germany*, 2008.

[159] W. Dollase, "Correction of intensities for preferred orientation in powder diffractometry: Application of the March model," *Journal of Applied Crystallography*, vol. 19, no. 4, pp. 267–272, 1986.

[160] A. Segmüller, "Characterization of epitaxial films by grazing-incidence X-ray diffraction," *Thin Solid Films*, vol. 154, no. 1, pp. 33–42, 1987.

[161] P. V. Braun, J. Cho, J. H. Pikul, W. P. King, and H. Zhang, "High power rechargeable batteries," *Current Opinion in Solid State and Materials Science*, vol. 16, no. 4, pp. 186–198, 2012.

[162] C. Julien and A. Mauger, "Review of 5-V electrodes for Li-ion batteries: Status and trends," *Ionics*, vol. 19, no. 7, pp. 951–988, 2013.

[163] L. Baggetto, R. R. Unocic, N. J. Dudney, and G. M. Veith, "Fabrication and characterization of Li–Mn–Ni–O sputtered thin film high voltage cathodes for Li-ion batteries," *Journal of Power Sources*, vol. 211, pp. 108–118, 2012.

[164] G. Cherkashinin, D. Ensling, and W. Jaegermann, "$LiMO_2$ (M= Ni, Co) thin film cathode materials: A correlation between the valence state of transition metals and the electrochemical properties," *Journal of Materials Chemistry A*, vol. 2, no. 10, pp. 3571–3580, 2014.

[165] T. Ohzuku and Y. Makimura, "Layered lithium insertion material of $LiCo_{1/3}Ni_{1/3}Mn_{1/3}O_2$ for lithium ion batteries," *Chemistry Letters*, vol. 30, no. 7, pp. 642–643, 2001.

[166] D. Ensling, *Photoelektronenspektroskopische Untersuchung der elektronischen Struktur dünner Lithiumkobaltoxidschichten.* PhD thesis, 2007. Darmstadt, Techn. Univ., Diss., 2006.

[167] L. Bohne, T. Pirk, and W. Jaegermann, "Investigations on the influence of the substrate on the crystal structure of sputtered $LiCoO_2$," *Journal of Solid State Electrochemistry*, vol. 17, no. 8, pp. 2095–2099, 2013.

[168] L. Bohne, "Integrierte 3D-Lithium-Ionen-Dünnschichtbatterien: Dünnschichtkathoden auf strukturierten Substraten und elektrochemische Eigenschaften," April 2012.

[169] J. Bates, N. Dudney, B. Neudecker, F. Hart, H. Jun, and S. Hackney, "Preferred orientation of polycrystalline $LiCoO_2$ films," *Journal of The Electrochemical Society*, vol. 147, no. 1, pp. 59–70, 2000.

[170] J. N. Reimers and J. Dahn, "Electrochemical and in situ X-ray diffraction studies of lithium intercalation in Li_xCoO_2," *Journal of the Electrochemical Society*, vol. 139, no. 8, pp. 2091–2097, 1992.

[171] A. Van der Ven and G. Ceder, "Lithium diffusion in layered Li_xCoO_2," *Electrochemical and Solid-State Letters*, vol. 3, no. 7, pp. 301–304, 2000.

[172] N. Yabuuchi, Y. Makimura, and T. Ohzuku, "Solid-state chemistry and electrochemistry of $LiCo_{1/3}Ni_{1/3}Mn_{1/3}O_2$ for advanced lithium-ion batteries III. Rechargeable capacity and cyclability," *Journal of The Electrochemical Society*, vol. 154, no. 4, pp. A314–A321, 2007.

[173] N. Yabuuchi and T. Ohzuku, "Novel lithium insertion material of $Li(Ni_{1/4}Mn_{1/2}Co_{1/3})O_2$ for advanced Lithium-ion batteries," *Journal of Power Sources*, vol. 119, pp. 171–174, 2003.

[174] S. Park, C. Yoon, S. Kang, H. Kim, S. Moon, and Y. Sun, "Synthesis and structural characterization of layered $Li(Ni_{1/3}Co_{1/3}Mn_{1/3})O_2$ cathode materials by ultrasonic spray pyrolysis method," *Electrochimica Acta*, vol. 49, no. 4, pp. 557–563, 2004.

[175] C. Loho, A. J. Darbandi, R. Djenadic, O. Clemens, and H. Hahn, "CO_2-laser flash evaporation as novel CVD precursor delivery system for functional thin film growth," *Chemical Vapor Deposition*, vol. 20, no. 4-5-6, pp. 152–160, 2014.

[176] K. Choy, "Chemical vapour deposition of coatings," *Progress in Materials Science*, vol. 48, no. 2, pp. 57 – 170, 2003.

[177] R. Dominko, M. Bele, M. Gaberšček, A. Meden, M. Remškar, and J. Jamnik, "Structure and electrochemical performance of Li_2MnSiO_4 and Li_2FeSiO_4 as potential Li-battery cathode materials," *Electrochemistry Communications*, vol. 8, no. 2, pp. 217–222, 2006.

[178] J.-L. Pouchou, "X-ray microanalysis of thin surface films and coatings," *Microchimica Acta*, vol. 138, no. 3-4, pp. 133–152, 2002.

[179] B. Hwang, Y. Tsai, D. Carlier, and G. Ceder, "A combined computational/experimental study on $LiNi_{1/3}Mn_{1/3}Co_{1/3}O_2$," *Chemistry of Materials*, vol. 15, no. 19, pp. 3676–3682, 2003.

[180] J. Deng, L. Xi, L. Wang, Z. Wang, C. Chung, X. Han, and H. Zhou, "Electrochemical performance of $LiCo_{1/3}Ni_{1/3}Mn_{1/3}O_2$ thin film electrodes prepared by pulsed laser deposition," *Journal of Power Sources*, vol. 217, pp. 491–497, 2012.

[181] K. Shaju, G. Subba Rao, and B. Chowdari, "Performance of layered $Li(Ni_{1/3}Co_{1/3}Mn_{1/3})O_2$ as cathode for Li-ion batteries," *Electrochimica Acta*, vol. 48, no. 2, pp. 145–151, 2002.

[182] Z. Guo, W. Liu, and B.-L. Su, "Fabrication of Co_3O_4 hierarchically superhydrophobic boat-like hollow cages at the silicon surface," *Nanotechnology*, vol. 19, no. 44, p. 445608, 2008.

[183] Y. Iriyama, M. Inaba, T. Abe, and Z. Ogumi, "Preparation of c-axis oriented thin films of $LiCoO_2$ by pulsed laser deposition and their electrochemical properties," *Journal of power sources*, vol. 94, no. 2, pp. 175–182, 2001.

[184] Y. J. Kim, E.-K. Lee, H. Kim, J. Cho, Y. W. Cho, B. Park, S. M. Oh, and J. K. Yoon, "Changes in the lattice constants of thin-film $LiCoO_2$ cathodes at the 4.2 V charged state," *Journal of The Electrochemical Society*, vol. 151, no. 7, pp. A1063–A1067, 2004.

[185] B. Wang, J. Bates, F. Hart, B. Sales, R. Zuhr, and J. Robertson, "Characterization of thin-film rechargeable lithium batteries with lithium cobalt oxide cathodes," *Journal of The Electrochemical Society*, vol. 143, no. 10, pp. 3203–3213, 1996.

[186] S. Verdier, L. El Ouatani, R. Dedryvere, F. Bonhomme, P. Biensan, and D. Gonbeau, "XPS study on Al_2O_3-and $AlPO_4$-coated $LiCoO_2$ cathode material for high-capacity Li ion batteries," *Journal of The Electrochemical Society*, vol. 154, no. 12, pp. A1088–A1099, 2007.

[187] A. Andersson, "Surface phenomena in Li-ion batteries," 2001.

[188] A. Andersson, D. Abraham, R. Haasch, S. MacLaren, J. Liu, and K. Amine, "Surface characterization of electrodes from high power lithium-ion batteries," *Journal of The Electrochemical Society*, vol. 149, no. 10, pp. A1358–A1369, 2002.

[189] N. Liu, H. Li, Z. Wang, X. Huang, and L. Chen, "Origin of solid electrolyte interphase on nanosized $LiCoO_2$," *Electrochemical and solid-state letters*, vol. 9, no. 7, pp. A328–A331, 2006.

[190] Z. Wang, X. Huang, and L. Chen, "Characterization of spontaneous reactions of $LiCoO_2$ with electrolyte solvent for lithium-ion batteries," *Journal of The Electrochemical Society*, vol. 151, no. 10, pp. A1641–A1652, 2004.

[191] K. Hoang and M. D. Johannes, "Defect chemistry in layered transition-metal oxides from screened hybrid density functional calculations," *Journal of Materials Chemistry A*, vol. 2, no. 15, pp. 5224–5235, 2014.

[192] Z. Wang, X. Huang, and L. Chen, "Performance improvement of surface-modified $LiCoO_2$ cathode materials: An infrared absorption and X-ray photoelectron spectroscopic investigation," *Journal of the Electrochemical Society*, vol. 150, no. 2, pp. A199–A208, 2003.

[193] H. Li, Z. Wang, L. Chen, and X. Huang, "Research on advanced materials for Li-ion batteries," *Advanced Materials*, vol. 21, no. 45, p. 4593, 2009.

[194] B. Fleutot, B. Pecquenard, H. Martinez, and A. Levasseur, "Thorough study of the local structure of LiPON thin films to better understand the influence of a solder-reflow type thermal treatment on their performances," *Solid State Ionics*, vol. 206, pp. 72–77, 2012.

[195] E. J. Jeon, Y. W. Shin, S. C. Nam, W. I. Cho, and Y. S. Yoon, "Characterization of all-solid-state thin-film batteries with V_2O_5 thin-film cathodes using ex situ and in situ processes," *Journal of The Electrochemical Society*, vol. 148, no. 4, pp. A318–A322, 2001.

[196] Y. Iriyama, T. Kako, C. Yada, T. Abe, and Z. Ogumi, "Charge transfer reaction at the lithium phosphorus oxynitride glass electrolyte/lithium cobalt oxide thin film interface," *Solid State Ionics*, vol. 176, no. 31, pp. 2371–2376, 2005.

[197] B. Kim, Y. S. Cho, J.-G. Lee, K.-H. Joo, K.-O. Jung, J. Oh, B. Park, H.-J. Sohn, T. Kang, J. Cho, *et al.*, "Ion-implantation modification of lithium–phosphorus oxynitride thin-films," *Journal of power sources*, vol. 109, no. 1, pp. 214–219, 2002.

[198] N. Mascaraque, J. L. G. Fierro, A. Durán, and F. Muñoz, "An interpretation for the increase of ionic conductivity by nitrogen incorporation in LiPON oxynitride glasses," *Solid State Ionics*, vol. 233, pp. 73–79, 2013.

[199] Y. Hamon, P. Vinatier, E. I. Kamitsos, M. Dussauze, C.-P. E. Varsamis, D. Zielniok, C. Roesser, and B. Roling, “Nitrogen flow rate as a new key parameter for the nitridation of electrolyte thin films,” *Solid State Ionics*, vol. 179, no. 21, pp. 1223–1226, 2008.

[200] E. I. Kamitsos, M. Dussauze, C.-P. E. Varsamis, P. Vinatier, and Y. Hamon, “Infrared spectroscopy of Li-diborate glassy thin films,” *Journal of non-crystalline solids*, vol. 353, no. 18, pp. 1818–1823, 2007.

[201] B. Fleutot, B. Pecquenard, H. Martinez, and A. Levasseur, “Lithium borophosphate thin film electrolyte as an alternative to LiPON for solder-reflow processed lithium-ion microbatteries,” *Solid State Ionics*, vol. 249, pp. 49–55, 2013.

[202] R. Marchand, “Nitrogen-containing phosphate glasses,” *Journal of Non-Crystalline Solids*, vol. 56, no. 1, pp. 173–178, 1983.

[203] R. W. Larson and D. E. Day, “Preparation and characterization of lithium phosphorus oxynitride glass,” *Journal of non-crystalline solids*, vol. 88, no. 1, pp. 97–113, 1986.

[204] B. Wang, B. Kwak, B. Sales, and J. Bates, “Ionic conductivities and structure of lithium phosphorus oxynitride glasses,” *Journal of non-crystalline solids*, vol. 183, no. 3, pp. 297–306, 1995.

[205] R. Marchand, Y. Laurent, J. Guyader, P. L’Haridon, and P. Verdier, “Nitrides and oxynitrides: Preparation, crystal chemistry and properties,” *Journal of the European Ceramic Society*, vol. 8, no. 4, pp. 197–213, 1991.

[206] B. Neudecker, R. Zuhr, and J. Bates, “Lithium silicon tin oxynitride (Li_ySiTON): High-performance anode in thin-film lithium-ion batteries for microelectronics,” *Journal of power sources*, vol. 81, pp. 27–32, 1999.

[207] L. Velli, C.-P. E. Varsamis, E. Kamitsos, D. Möncke, and D. Ehrt, “Structural investigation of metaphosphate glasses,” *Physics and Chemistry of Glasses-European Journal of Glass Science and Technology Part B*, vol. 46, no. 2, pp. 178–181, 2005.

[208] L. Popović, D. De Waal, and J. Boeyens, “Correlation between Raman wavenumbers and P-O bond lengths in crystalline inorganic phosphates,” *Journal of Raman spectroscopy*, vol. 36, no. 1, pp. 2–11, 2005.

[209] D. Corbridge and E. Lowe, “The infra-red spectra of some inorganic phosphorus compounds,” *Journal of the Chemical Society (Resumed)*, pp. 493–502, 1954.

[210] A. Boulant, J. F. Bardeau, A. Jouanneaux, J. Emery, J.-Y. Buzare, and O. Bohnke, “Reaction mechanisms of $Li_{0.30}La_{0.57}TiO_3$ powder with ambient air: H^+/Li^+ exchange with water and Li_2CO_3 formation,” *Dalton Transactions*, vol. 39, no. 16, pp. 3968–3975, 2010.

[211] F. Muñoz, A. Durán, L. Pascual, L. Montagne, B. Revel, and A. C. M. Rodrigues, “Increased electrical conductivity of LiPON glasses produced by ammonolysis,” *Solid State Ionics*, vol. 179, no. 15, pp. 574–579, 2008.

[212] R. K. Brow, M. R. Reidmeyer, and D. E. Day, “Oxygen bonding in nitrided sodium-and lithium-metaphosphate glasses,” *Journal of non-crystalline solids*, vol. 99, no. 1, pp. 178–189, 1988.

[213] Y. G. Kim and H. Wadley, “The influence of the nitrogen-ion flux on structure and ionic conductivity of vapor deposited lithium phosphorus oxynitride films,” *Journal of Power Sources*, vol. 196, no. 3, pp. 1371–1377, 2011.

[214] J. J. Hudgens, R. K. Brow, D. R. Tallant, and S. W. Martin, “Raman spectroscopy study of the structure of lithium and sodium ultraphosphate glasses,” *Journal of non-crystalline solids*, vol. 223, no. 1, pp. 21–31, 1998.

[215] L. Boukbir, R. Marchand, Y. Laurent, Z. J. Chao, C. Parent, and G. Le Flem, “A structural investigation of phosphorus oxynitride glasses,” *Journal of Solid State Chemistry*, vol. 87, no. 2, pp. 423–429, 1990.

[216] A. Le Sauze, L. Montagne, G. Palavit, and R. Marchand, “Nitridation of alkali metaphosphate glasses: A comparative structural analysis of the Na–P–O–N and Li–Na–P–O–N systems,” *Journal of non-crystalline solids*, vol. 293, pp. 81–86, 2001.

[217] Y. A. Du and N. Holzwarth, “Effects of O vacancies and N or Si substitutions on Li^+ migration in Li_3PO_4 electrolytes from first principles,” *Physical Review B*, vol. 78, no. 17, p. 174301, 2008.

[218] Y. A. Du and N. Holzwarth, “First-principles study of LiPON and related solid electrolytes,” *Physical Review B*, vol. 81, no. 18, p. 184106, 2010.

[219] J. Xie, J. F. Oudenhoven, P.-P. R. Harks, D. Li, and P. H. Notten, “Chemical vapor deposition of lithium phosphate thin-films for 3D all-solid-state Li-ion batteries,” *Journal of the Electrochemical Society*, vol. 162, no. 3, pp. A249–A254, 2015.

THÈSE EN COTUTELLE PRÉSENTÉE

POUR OBTENIR LE GRADE DE

DOCTEUR DE

L'UNIVERSITÉ DE BORDEAUX

ET DE TECHNISCHE UNIVERSITÄT DARMSTADT

ÉCOLE DOCTORALE DES SCIENCES CHIMIQUES
SPECIALITE: PHYSICO-CHIMIE DE LA MATIERE CONDENSEE

ÉCOLE DOCTORALE DU PARTENAIRE

Par Mercedes Alicia CARRILLO SOLANO

DEVELOPMENT OF ARTIFICIAL SURFACE LAYERS FOR THIN FILM CATHODE MATERIALS

Sous la direction de Mme. Laurence CROGUENNEC & M. Wolfram JAEGERMANN

Soutenue le 30 octobre, 2015

Membres du jury :

M. Maximilian FICHTNER	Professeur, Helmholtz Institute Ulm, Allemagne	Rapporteur
M. Frédéric LE CRAS	Ingénieur Chercheur HDR, CEA LETI, France	Rapporteur
M. Jörg SCHNEIDER	Professeur, Technische Universität Darmstadt, Allemagne	Examinateur
M. Hervé MARTINEZ	Professeur, Université de Pau et Pays de L'Adour, France	Examinateur
M. Ralf RIEDL	Professeur, Technische Universität Darmstadt, Allemagne	Examinateur
M. Wolfram JAEGERMANN	Professeur, Technische Universität Darmstadt, Allemagne	Directeur
Mme. Laurence CROGUENNEC	Directrice de Recherche CNRS, ICMCB, France	Directeur
M. Philippe VINATIER	Maître de Conférence CNRS, ICMCB, France	Invité

Titre : Développement de surface artificielles pour cathode sous forme de couche mince pour accumulateurs Li-ion

Abstract:

Ce travail porte sur la recherche de différentes compositions de couches minces pour accumulateurs Li-ion.

Une première partie a été dédiée au dépôts de cathode sous forme de couche mince d'un matériau connu, $LiCoO_2$, et d'un matériau alternatif, $Li(NiMnCo)O_2$ en utilisant le dépôt physique en phase vapeur (PVD) et le dépôt chimique en phase vapeur (CVD), respectivement. Les résultats ($LiCoO_2$) ont montrés comment, après cyclage, il y a diminution de la capacité à cycler à régime rapide et augmentation de la résistance à l'interface. La diffraction des rayons X a montré la présence de différentes orientations, peu cristallisées, appartenant à la phase $LiCoO_2$ HT selon confirmation par la littérature. Les couches minces de $Li(Ni_xMn_yCo_{1-x-y})O_2$ ont été préparées par dépôt chimique en phase vapeur assisté par aérosol. La diffraction des rayons X et l'analyse Rietveld utilisant le modèle March-Dollase a été mise en œuvre pour la détermination de la texture et des caractéristiques microstructurales. La morphologie des films a été caractérisée par microscopie électronique à balayage. L'étude a montré que la concentration de la solution de précurseur et la pression totale ont un effet majeur sur la morphologie des films et leur texture.

Une seconde partie s'est focalisée sur l'interface cathode-électrolyte pour trois cas d'étude : 1) couche mince de matériau de cathode $LiCoO_2$, 2) couche mince de $LiCoO_2$ recouvert de ZrO_2 et 3) couche mince de $LiCoO_2$ recouvert de LIPON. L'interface cathode-électrolyte de ces trois cas d'étude a été étudiée avant et après cyclage galvanostatique afin de déterminer les caractéristiques de la couche de surface et les changements provenant à l'interface lors du fonctionnement de l'accumulateur. L'interface des couches minces de $LiCoO_2$ a été étudiée plus en détail après trempage dans un électrolyte liquide afin de comprendre l'effet des procédures de stockages courts dans les accumulateurs.

De plus, les couches minces de LiPON ont été étudiées sur la base de changements structuraux se produisant avec la nitruration et sa corrélation à un possible mécanisme ayant lieu durant la conduction ionique.

Mots clés : Accumulateurs Li ion, Couches minces, $LiCoO_2$, Surface artificielle, ZrO_2, LiPON

Title : Development of artificial surface layers for thin film cathode materials

Abstract :

The present work was based on the investigation of different thin film components of Li ion batteries. A first part was dedicated to the deposition of cathodes in thin film form of a known material, $LiCoO_2$, and an alternative one, $Li(NiMnCo)O_2$ employing physical vapor deposition (PVD) and chemical vapor deposition (CVD), respectively. Results on the deposition of $LiCoO_2$ showed how after cycling there is a reduction of rate capability and increase in interface resistance. The X-ray diffraction pattern showed the presence of several orientations related to the known HT phases found in literature for $LiCoO_2$ with low crystallinity. On the other hand $Li(Ni_xMn_yCo_z)O_2$ thin films prepared via aerosol assisted CVD were analyzed with X-ray diffraction and Rietveld refinement using the March-Dollase model for the determination of the texturing and microstructural characteristics. Additionally the morphology of the films was characterized using scanning electron microscopy. The investigation showed that concentration of precursor solution and process pressures have a significant effect on the film morphology and texturing.

A second part was focused on the cathode-electrolyte interface for three case studies: 1) as deposited $LiCoO_2$ cathode thin film, 2) ZrO_2 coated $LiCoO_2$ thin film and 3) LiPON coated $LiCoO_2$ thin film. The interface cathode-electrolyte of these three cases were studied before and after galvanostatic cycling to determine surface layer characteristics and changes arising on the interface after battery operation. The interface of a bare $LiCoO_2$ layer was further studied after soaking in liquid electrolyte to elucidate the effect of short storage procedures in batteries.

Surface analysis done on $LiCoO_2$ thin films showed changes occurring at the interface layers after the electrode was in short contact with the electrolyte solution and after galvanostatic cycling. Washing and soaking the electrode material in electrolyte and solvent showed that surface reactions start from the first contact. A main component of the electrolyte solution, $LiPF_6$, has critical effect since it can decompose and form HF which reacts with carbonates and forms LiF on the surface. Given the large amount of LiF, a high reactivity of $LiCoO_2$ with the decomposed species was observed, as the main components of the film were related to the decomposed $LiPF_6$ salt.

The surface chemistry of the layer formed on $LiCoO_2$ after cycling was mainly based on decomposed species from the electrolyte salt arising from carbonated and fluorinated species. Artificial surface layers were deposited on $LiCoO_2$ by means of rf sputtering. The thin layers of ZrO_2 and LiPON used as coatings had minor effects on the original film morphology and crystalline structure. An XPS analysis of the interface showed how the nature of each layer after galvanostatic cycling was different for each case. The resulting artificial surface layer formed from ZrO_2 coating showed mainly inorganic species, while the LiPON coated cathode showed an organic nature. The final surface layers after electrochemical cycling of the ZrO2 coated film resembled that of the uncoated $LiCoO_2$.

Additionally, LiPON thin films were studied on the basis of structural changes occurring with nitrogenation and its correlation to a possible mechanism during ion conduction. Composition of phosphate glasses with rf sputtering was proven to be greatly influenced by the gas ratio employed. The largest variations were observed for lower amounts of N_2 in the gas mixture. The IR spectra results showed important differences in the short range order for films with a similar amount of lithium. The lithium phosphorus oxynitride films deposited here presented glassy structures with mainly ortho and pyro-phosphate units with small amounts of short metaphosphate chains. Nitrogen insertion favors stability of lithium by giving an environment with lower potential energy, as was evidenced by the far-IR results.

Keywords : Li-ion batteries, Thin film cathode, $LiCoO_2$, Artificial surface layer, ZrO_2, LiPON

Unité de recherche

[Institut de Chimie de la Matière Condensée de Bordeaux (ICMCB) - UPR 9048]

Mercedes Alicia Carrillo Solano

Date and place of birth: August 12, 1984; Barrancas, La Guajira (Colombia 🇨🇴)

Qualification: **Physical Chemist (MSc) & Materials Engineer (MEng)**

Experience

10/2011—09/2014 **Researcher** — Darmstadt, Germany

Technische Universität Darmstadt – Surface Science Group.

-Thin film preparation of oxides/oxynitrides for battery systems (PVD, CVD).
- Fundamental and technical understanding of thin film deposition techniques for Li-ion battery cells in UHV systems.
- Developed performance test schemes, surface and electrochemical characterization, for Li-ion battery systems including IR, XPS, SEM, XRD, GCPL, EIS and CV.
- Developed scientific research collaboration between industrial and academic partners.

02/2011—06/2011 **Scientific Internship** — Grenoble, France

Institut National Polytechnique de Grenoble (INP-LMPG)

- Prepared and characterized thin film oxides for photovoltaic applications.
- Studied and tested precursors for commercial products.
- Conducted experiments with Metal Organic CVD equipment.

01/2009—05/2009 **Assistant teacher** — Bogotá, Colombia

Universidad de los Andes, Chemistry Department

- Organized and coordinated chemical laboratory activities.
- Taught general laboratory chemistry to engineers.

Education

10/2011—10/2015 **Doctorate** — Darmstadt, Germany

Defended 30.10.2015

Dr.Ing /Technische Universität Darmstadt & Dr.Ing /Université de Bordeaux

International Doctoral School in Functional Materials (IDS-FunMat)

Surface and electrochemical study of materials for Li-ion batteries.

09/2009—07/2011 **Master** — Paris, France/ Genova, Italy

Master Sc Phys. Chem /Université Paris Sud 11 & Master Mat. Eng. /Università di Genova

International Master in Surface, Electrochemistry, Radiation and Photochemistry.

01/2006—05/2009 **Bachelor** — Bogotá, Colombia
Chemist - Universidad de los Andes
Thermodynamics of adsorption processes on commercial activated carbon.

2nd place Poster Award: European Material Research Society Spring meeting (E-MRS), May 2014, Lille, France. "Development of artificial Solid Electrolyte Interface layers for battery materials.

Additional training

08/2015—10/2015 **German language course** — Darmstadt, Germany
Donner and Partner

03/2014 **Scientific communication** — Spa, Belgium
IDS-FunMat Training School - 2014

03/2013 **Scientific communication, intellectual property and innovation** — Annecy, France
IDS-FunMat Training School - 2013

10/2012 **RGI Workshop "How can Grids protect and enhance the Environment? - Implementing the European Grid Declaration"** — Paris, France
Renewables-Grid-Initiative - 2012

03/2012 **Project and risk management and scientific communication** — Anglet, France
IDS-FunMat Training School - 2012

08/2010 **International School in project and risk management and communication** — Genova, Italy
SERP-Chem summer school - 2010

01/2010—06/2010 **Advanced training in Photochemistry** — Poznan, Poland
Universidad Adam Mickiewicz de Poznań Photochemistry.

Languages

Spanish:	Native
German:	Basic knowledge
English:	Advanced
French:	Basic knowledge
Italian:	Intermediate

Publications

M.A. Carrillo Solano, M. Dussauze, P. Vinatier, E.I. Kamitsos & W. Jaegermann, (2015) “Phosphate structure and lithium environments in lithium phosphorus oxynitride amorphous thin films”, Ionics DOI no. 10.1007/s11581-015-1573-1

M. Motzko, **M.A. Carrillo Solano**, W. Jaegermann & R. Hausbrand, (2015) Photoemission Study of the Interaction Between $LiCoO_2$ Thin Films and Adsorbed Water", The Journal of Physical Chemistry C. DOI: 10.1021/acs.jpcc.5b05793

M.A. Carrillo Solano; O. Clemens; A. J. Darbandi, H. Hahn, R. Hausbrand & W. Jaegermann, (2015) “Preparation of $LiNiMnCoO_2$ thin films for Li-ion batteries by aerosol-assisted chemical vapor deposition” , Thin Solid Films. *Under Review*

A. Schwöbel, R. Precht, M. Motzko, **M.A. Carrillo Solano**, W. Calvet, R. Hausbrand, & W. Jaegermann, (2014) “Determination of the valence band structure of an alkali phosphorus oxynitride glass: A synchrotron XPS study on LiPON”. Applied Surface Science, 321, 55-60.